

**An experimental study of the system FeO-Fe<sub>2</sub>O<sub>3</sub>-SiO<sub>2</sub> at high pressures and temperatures: Garnet, perovskite and post-perovskite phases**

Der Bayreuther Graduiertenschule für Mathematik und Naturwissenschaften

zur Erlangung der Würde eines  
Doktors der Naturwissenschaften

-Dr. rer. nat.-

vorgelegte

**Dissertation**

von

**Leyla Ismailova**

**aus Moskau (Russland)**

**Bayreuth, 2016**

This doctoral thesis was prepared at the at the Bavarian Research Institute of Experimental Geochemistry and Geophysics and the Laboratory of Crystallography at the University of Bayreuth from 08/2013 until 04/2016 and was supervised by Prof. Dr. Natalia Dubrovinskaia and Prof. Dr. Leonid Dubrovinsky.

This is a full reprint of the dissertation submitted to obtain academic degree of Doctor of Natural Sciences (Dr. rer. nat.) and approved by the Bayreuth Graduate School of Mathematical and Natural Sciences (BayNAT) of the University of Bayreuth.

Date of submission: 30.03.2016

Date of defense: 03.08.2016

Acting director: Prof. Dr. Stephan Kümmel

Doctoral committee:

Prof. Dr. Leonid Dubrovinsky (1<sup>st</sup> reviewer)

Prof. Dr. Daniel Frost (2<sup>nd</sup> reviewer)

Prof. Dr. Natalia Dubrovinskaia (chairman)

Dr. Hauke Marquardt

## Zusammenfassung

Granate stellen eine wichtige Mineralgruppe im oberen Erdmantel und der Übergangszone dar. Materialien mit Granatstruktur sind zusätzlich essentiell für viele industrielle Anwendungen. Unter den Druck- und Temperaturbedingungen des unteren Erdmantels wandeln sich Granate erst in Si-Perovskit (Bridgmanit) um, der sich mit zunehmender Tiefe in Post-Perovskit mit  $\text{CaIrO}_3$ -Struktur umformt. Der Einbau von Eisen in die Kristallstrukturen der oben genannten Phasen kann einen enormen Einfluss auf die chemischen und physikalischen Eigenschaften des Erdmantels haben, sowie auf dessen Dynamik und Evolution. Um diesen Einfluss zu untersuchen sind experimentelle Messungen unter den relevanten Druck- und Temperaturbedingungen notwendig. Die Ergebnisse dieser Arbeit beinhalten neue Einblicke in die Chemie und Elastizität dieser relevanten Mineralphasen des Erdmantels.

Skiagit-reiche Granat-Einkristalle wurden bei einem Druck von 9.5 GPa und einer Temperatur von 1100 °C in der Vielstempelpresse synthetisiert. Die Kristallstruktur wurde dabei mithilfe von Synchrotron-Einkristall-Röntgenbeugung untersucht. Anhand von Synchrotron-Mößbauer-Spektroskopie-Messungen wurde festgestellt, dass  $\text{Fe}^{2+}$  wie erwartet auf den Dodekaeder- und  $\text{Fe}^{3+}$  auf den Oktaeder-Positionen eingebaut wird. Die Strukturformel  $\text{Fe}_3(\text{Fe}^{2+}_{0.234(2)}\text{Fe}^{3+}_{1.532(2)}\text{Si}^{4+}_{0.234(2)})(\text{SiO}_4)_3$  wurde mithilfe von Einkristall-Röntgenbeugung und Elektronenmikrosonden-Analysen ermittelt und zeigt, dass Skiagit-reicher Granat einen Überschuss an  $\text{Si}^{4+}$  und  $\text{Fe}^{2+}$  auf den Oktaeder-Positionen aufweist. Das deutet darauf hin, dass der in dieser Arbeit synthetisierte Granat einen Skiagit-Fe-Majorit Mischkristall darstellt, wobei das Skiagit ~23 mol% des Fe-Majorit Endglieds ( $\text{Fe}_2^{3+}(\text{Fe}^{2+}\text{Si}^{4+})\text{Si}_3\text{O}_{12}$ ) enthält.

Weitere Synthesen von Skiagit-Majorit Mischkristallen wurden bei unterschiedlichen Drücken und Temperaturen durchgeführt und zeigen, dass Skiagit bis zu 76 % des Fe-Majorit Endglieds aufnehmen kann. Der Einbau von  $\text{Fe}^{2+}$  und  $\text{Si}^{4+}$  anstelle von  $\text{Fe}^{3+}$  in die Oktaeder-Positionen führt zu einer Verringerung des Volumens der Einheitszelle unter Raumdruck und -temperatur. Mithilfe von Experimenten in der Diamantstempelzelle wurden Zustandsgleichungen der Granate mit unterschiedlichen Zusammensetzungen bestimmt. In-situ Einkristall-Röntgenbeugung bis 90 GPa zeigen einen Anstieg des Kompressionsmoduls von 164(3) GPa bis 169(3) GPa bei einer

gradueller Zunahme der Majorit-Komponente. Die experimentellen Ergebnisse dieser Arbeit kombiniert mit bereits publizierten Daten aus der Literatur demonstrieren einen deutlichen Einfluss des gesamten Eisengehalts, sowie des  $\text{Fe}^{3+}/\text{Fe}^{2+}$ -Verhältnisses auf die Elastizität von (Mg,Fe)-Majorit. Zwischen 50 GPa und 60 GPa verringert sich das molare Volumen des Skiagit-Fe-Majorits abrupt um rund 3%. Analysen mithilfe von Einkristall-Röntgenbeugung und Hochdruck-Synchrotron-Mößbauer-Spektroskopie weisen darauf hin, dass diese Volumenabnahme auf eine Veränderung des elektronischen Zustandes des Eisens im Oktaeder zurückzuführen ist.

Experimente unter Hochdruck und -temperatur in der Vielstempelpresse bis 25 GPa zeigen, dass Skiagit-Majorit bis 12.5 GPa stabil ist und mit höherem Druck zu Fe-Oxiden und  $\text{SiO}_2$  zerfällt. Experimente mit Skiagit-Majorit-Granaten in einer laserbeheizten Diamantstempelzelle bis 40 GPa und zwischen 1500 und 2300 K, führen zu einem Zerfall zu  $\text{Fe}_4\text{O}_5$  und Stishovit ( $\text{SiO}_2$ ). Bei einem Druck oberhalb von 45 GPa und denselben Temperaturen zerfallen die Granate zu einer Hochdruckform von  $\text{Fe}_3\text{O}_4$  und Fe-Bridgmanit.

Fe-reicher Bridgmanit wird von  $\text{Fe}^{3+}$  stabilisiert, wodurch es möglich wird, puren Eisensilikat-Perovskit der Zusammensetzung  $\text{Fe}^{2+}_{0.64(2)}\text{Fe}^{3+}_{0.24(2)}\text{Si}_{1.00(3)}\text{O}_3$  zwischen ~45 GPa und 110 GPa zu synthetisieren. Die Kristallchemie des  $\text{Fe}^{3+}$ -reichen Bridgmanits ist dabei sehr ungewöhnlich, da Eisen in dem großen, verzerrten Prisma (Position A) eingebaut ist und kein Eisen im Oktaeder (Position B) messbar ist. Des Weiteren enthält Bridgmanit ~12% Gitterdefekte auf Position A. Die Kompressibilität von Fe-Bridgmanit ( $K_{300}=190(4)$  GPa,  $K'=4$ ,  $V_0=178.98(6)$  Å<sup>3</sup>/Einheitszelle) ist signifikant höher als die Kompressibilitäten bereits bekannter Fe- und/oder Al-Bridgmanite.

Pure Eisensilikat-Post-Perovskite wurden in einer laserbeheizten Diamantstempelzelle zwischen Drücken von 127(1) GPa und 146(1) GPa von den Ausgangsphasen Skiagit-Majorit und Fe-Bridgmanit synthetisiert. Synchrotron-Röntgenbeugung zeigt, dass der Einbau von Eisen im Vergleich zu Mg-reichen Post-Perovskit zu einer Zunahme des Volumens der Einheitszelle führt. Die Volumenzunahme um 3.5% relativ zu Fe-freien Post-Perovskit ist durch eine Vergrößerung des Einheitszellenparameters b der Post-Perovskit-Struktur um 2.30% erklärbar. Die Dichte des untersuchten Post-Perovskits ( $6.670$  g/cm<sup>3</sup>) ist um 3% niedriger als die geschätzte Dichte für puren  $\text{FeSiO}_3$  ( $6.928$  g/cm<sup>3</sup>) unter denselben

Bedingungen. Die Ergebnisse bezüglich des puren Eisen-Post-Perovskits unterstützen die Annahme, dass die Anreicherung von Eisen einer der Gründe für die Bildung von sogenannten „ultra-low velocity“-Zonen im unteren Teil des unteren Erdmantels ist.

## Summary

Garnets are important minerals in the Earth's upper-mantle and transition zone, and materials with the garnet structure are essential for many industrial applications. At lower mantle conditions, garnets transform into silicate perovskite (bridgmanite) and eventually into post-perovskite (CaIrO<sub>3</sub>-structured) silicate. Incorporation of iron into the structures of these phases can strongly affect chemical and physical properties of the Earth's mantle, as well as its dynamics and evolution. In order to determine these effects, experimental measurements at relevant pressure-temperature conditions are needed. The results that comprise this thesis provide new insights into the chemistry and elasticity of mantle minerals.

Single crystals of skiaigite-rich garnet were synthesized at a pressure of 9.5 GPa and temperature of 1100 °C using a multi-anvil apparatus. The crystal structure was investigated using single-crystal synchrotron X-ray diffraction. Synchrotron Mössbauer source spectroscopy revealed that Fe<sup>2+</sup> and Fe<sup>3+</sup> predominantly occupy dodecahedral and octahedral sites, respectively, as expected for the garnet structure. The structural formula Fe<sub>3</sub>(Fe<sup>2+</sup><sub>0.234(2)</sub>Fe<sup>3+</sup><sub>1.532(2)</sub>Si<sup>4+</sup><sub>0.234(2)</sub>)(SiO<sub>4</sub>)<sub>3</sub>, obtained from single-crystal X-ray diffraction data and electron microprobe analyses shows that the skiaigite-rich garnet synthesized in our experiment contains excess of Si and Fe<sup>2+</sup> entering the octahedral site. The occurrence of Si and Fe<sup>2+</sup> in the octahedral site means that this synthetic garnet is a skiaigite – Fe-majorite solid solution: the end-member skiaigite contains ~23 mol% of the Fe-majorite end-member (Fe<sub>2</sub><sup>3+</sup>(Fe<sup>2+</sup>Si<sup>4+</sup>)Si<sub>3</sub>O<sub>12</sub>) component.

Systematic synthesis of skiaigite-majorite garnets at different pressures and temperatures shows that skiaigite can accommodate up to 76% of the Fe-majorite end-member. The substitution of Fe<sup>2+</sup> and Si<sup>4+</sup> for Fe<sup>3+</sup> in the octahedral site decreases the unit-cell volume of garnets at ambient conditions. Equations of states of garnets with different compositions were measured using the diamond anvil cell technique. The analysis of single-crystal X-ray diffraction data collected upon compression up to 90 GPa reveals that with increasing majorite component, the bulk modulus slightly increases from 164(3) to 169(3) GPa. Our experimental results and the analysis of the literature data unambiguously demonstrate a considerable influence of the total iron content and the Fe<sup>3+</sup>/Fe<sup>2+</sup> ratio in (Mg,Fe)-majorites on their elasticity. At pressures

between 50 and 60 GPa, a significant deviation from a monotonic dependence of the molar volumes of skiagite-Fe-majorite garnets on pressure was observed, and in the small pressure interval (just 10 GPa) the volume drop was approximately 3%. By combining single crystal diffraction and high-pressure synchrotron Mössbauer spectroscopy results, we found that such changes in the compressional behaviour were associated with changes in the electronic state of Fe in the octahedral site.

High-pressure high-temperature experiments in multi-anvil apparatus up to 25 GPa show that skiagite-majorite is stable up to 12.5 GPa and then decomposes to a mixture of Fe oxides and SiO<sub>2</sub>. Laser heating of skiagite-majorite garnets in the diamond-anvil cell at pressures up to about 40 GPa and temperatures between 1500 and 2300 K resulted in decomposition to Fe<sub>4</sub>O<sub>5</sub> and stishovite (SiO<sub>2</sub>), but above 45 GPa, heating of the garnet resulted in the formation of a high-pressure form of Fe<sub>3</sub>O<sub>4</sub> and Fe-bridgmanite.

Ferric iron stabilizes Fe-rich bridgmanite to such an extent that it is possible to synthesize pure iron silicate perovskite at pressures between ~45 GPa and 110 GPa with the resulting composition (Fe<sup>2+</sup><sub>0.64(2)</sub>Fe<sup>3+</sup><sub>0.24(2)</sub>)Si<sub>1.00(3)</sub>O<sub>3</sub> (within uncertainty of measurements independent of conditions of synthesis). The crystal chemistry of ferric iron-bearing bridgmanite is very unusual. First, all iron is located in a large distorted prism (A site) with no evidence of iron in the octahedral (B) site. Second, bridgmanite contains a significant amount of vacancies (~12%) at the A site. Moreover, the compressibility of iron bridgmanite (K<sub>300</sub>=190(4) GPa, K'=4, V<sub>0</sub>=178.98(6) Å<sup>3</sup>/unit cell) is anomalously high compared to any known Fe- or/and Al-rich bridgmanites.

At pressures of 127(1) GPa and 146(1) GPa, pure iron silicate post-perovskite was synthesized using laser-heated diamond anvil cell from skiagite-majorite garnet and Fe bridgmanite. Synchrotron X-ray diffraction revealed that the incorporation of iron leads to increase of the unit-cell volume relative to magnesium post-perovskite. The change in unit cell parameter *b* in the post-perovskite structure is the most significant contribution to volume expansion; it increases in length by 2.39% and increases total volume by 3.5% in comparison to Fe-free post-perovskite. The density of studied post-perovskite (6.670 g/cm<sup>3</sup>) is 3% lower than the density estimated at the same conditions for pure FeSiO<sub>3</sub> (6.928 g/cm<sup>3</sup>). Results from synthesis of pure iron post-perovskite support the idea that iron enrichment may be one of the reasons for formation of ultra-low velocity zones at the base of the lower mantle.

## **Acknowledgments**

I would like to thank my supervisors Leonid Dubrovinsky and Natalia Dubrovinskaia for their patience and believe in this work. I couldn't have found better advisors.

I want to thank Prof.Dr. Andrey Bobrov from Moscow State University for the huge help with this project.

I want to thank Hans Keppler for his great spectroscopy and diffraction classes, and for his support during all the time that I spend in Bayreuth.

I want to say a great thank to Catherine McCammon and Tiziana Boffa Balaran for their scientific help.

I can't imagine my time in Bayreuth without help of my "junior supervisors" and good friends Elena and Maxim. It was a great pleasure to work with them and learn crystallography from them.

Many thanks to my officemates Somnath and George for creating very friendly working atmosphere.

Within past 3 years I managed to create a lot of friends and I'm going to miss all of them: Alex, Elena, Hipster, Slava, Martha, Zsani, Nicki, Fabi, Catherina, Ines, Sylvain. I want to thank them all for this amazing time in BGI.

A huge thank to Nicki for translating my summary and Andi for proofing English in my thesis.

I want to express a huge love to my family: papa Sabir, mama Larisa and Kirill for giving me love, support and being with me all the time.

## TABLE OF CONTENTS

<b>Zusammenfassung</b> .....	<b>3</b>
<b>Summary</b> .....	<b>6</b>
<b>Acknowledgments</b> .....	<b>8</b>
<b>1 Introduction</b> .....	<b>11</b>
<b>1.1 Structure and composition of the Earth's mantle</b> .....	<b>11</b>
<b>1.2 Iron in selected silicate mantle minerals (garnets, perovskite and post-perovskite)</b> .....	<b>13</b>
<b>2 Methods</b> .....	<b>17</b>
<b>2.1 Methods of high pressure high temperature synthesis</b> .....	<b>17</b>
2.1.1 Multi anvil apparatus.....	17
2.1.2 Diamond anvil cell.....	19
<b>2.2 Analytical techniques</b> .....	<b>21</b>
2.2.1 Synchrotron techniques.....	21
Equation of state.....	23
2.2.2 Electron microprobe.....	25
<b>3 Synopsis</b> .....	<b>26</b>
<b>3.1 High-pressure synthesis of skiagite-majorite garnet</b> .....	<b>27</b>
<b>3.2 Effect of composition on compressibility of skiagite - Fe-majorite garnets</b> .....	<b>30</b>
<b>3.3 Stability of Fe,Al-bearing bridgmanite in the lower mantle and synthesis of pure Fe-bridgmanite</b> .....	<b>33</b>
<b>3.4 Synthesis of pure iron post-perovskite</b> .....	<b>37</b>
<b>4 List of manuscripts and individual contribution of all authors</b> .....	<b>41</b>
<b>5 Results</b> .....	<b>44</b>
<b>5.1 High-pressure synthesis of skiagite-majorite garnet and investigation of its crystal structure</b> .....	<b>44</b>
5.1.1 Introduction.....	45

5.1.2 Experimental methods.....	46
5.1.3 Results and discussion.....	48
5.1.4 Implications.....	62
<b>5.2 Effect of composition on compressibility of skiagite-Fe-majorite garnet.....</b>	<b>63</b>
5.2.1 Introduction.....	64
5.2.2 Methods.....	65
5.2.3 Results.....	67
5.2.4 Discussion.....	78
5.2.5 Conclusions.....	84
5.2.6 Supplementary Materials.....	84
<b>5.3 Stability of Fe,Al-bearing bridgmanite in the lower mantle and synthesis of pure Fe-bridgmanite.....</b>	<b>112</b>
5.3.1 Main Text.....	113
5.3.2 Supplementary materials.....	123
<b>5.4 Synthesis of pure iron silicate post-perovskite.....</b>	<b>149</b>
5.4.1 Introduction.....	149
5.4.2 Experimental methods.....	150
5.4.3 Results.....	151
5.4.4 Implications.....	157
<b>6 References.....</b>	<b>159</b>

# 1 INTRODUCTION

## 1.1 Structure and composition of the Earth's mantle

Knowledge of the Earth's composition and structure are essential in understanding the evolution of planets and global geological processes. It yields insights into how our planet formed and evolved, as well as provides us with the information important for understanding of the development of other planets.

The chemical composition of the Earth is derived from geophysical observations, geochemical studies of natural rocks and minerals, inclusions in diamonds, and experimental and theoretical studies of phases related to the Earth's interior. Seismic profiles revealed the presence of two major discontinuities within the mantle: (a) at the transition zone, at a depth of 410 to 660 km, which defines the boundary between the upper and the lower mantle; (b) and the D'' layer that locates at the core-mantle boundary. Composition of the Earth's mantle is assumed to be "pyrolitical" and the upper mantle is comprised of four major minerals: olivine  $(\text{Mg,Fe})_2\text{SiO}_4$ , orthopyroxene  $(\text{Mg,Fe})\text{SiO}_3$ , clinopyroxene  $\text{Ca}(\text{Mg,Fe})_2\text{Si}_2\text{O}_6$ , and garnets  $(\text{Mg,Fe,Ca})_3\text{Al}_2\text{Si}_3\text{O}_{12}$  (Ringwood 1975).

The first discontinuity in the mantle is associated with the transition between different polymorphs of olivine  $(\text{Mg,Fe})_2\text{SiO}_4$ . At a pressure of about 14 GPa which corresponds to a depth of about 410 km, the  $\alpha$ -phase, olivine, transforms to the  $\beta$ -phase, wadsleyite, with a spinel structure. This transition, which is now widely accepted, is the reason for the discontinuity in the seismic wave's propagation at this depth. Deeper in the mantle, at about 17 GPa (500-550 km depth), wadsleyite transforms to more densely packed spinel structured  $\gamma$ -phase, ringwoodite. This transition may also cause a weak seismic discontinuity.

The decomposition of ringwoodite into  $(\text{Mg,Fe})\text{SiO}_3$  with the perovskite structure and  $(\text{Mg,Fe})\text{O}$  oxide (magnesiowüstite) is responsible for the 660-km discontinuity.

Pyroxenes start to dissolve into the garnet at pressures of around  $\sim 5$  GPa as majoritic components, transforming the garnet into a silica-rich garnet (Akaogi and Akimoto 1977; Irifune et al. 1986; Irifune 1987; Irifune and Ringwood 1993). This transformation is completed at approximately mid-transition zone pressures of about 15 GPa (Irifune 1987). The coupled substitution of  $(\text{Mg,Fe,Ca})^{2+}$  and  $\text{Si}^{4+}$  in the octahedral sites of cubic garnet leads to the ideal majorite end-member  $(\text{Mg,Fe,Ca})_4\text{Si}_4\text{O}_{12}$  stoichiometry – identical to that of pyroxene. The stability field of garnet increases. In the transition zone majoritic garnet is one of the predominant phases; it transforms to a perovskite-structured phase in the lower mantle.

The most abundant phase of the lower mantle ( $\sim 80\%$  by volume) is bridgmanite (perovskite-structured  $(\text{Mg,Fe,Al})(\text{Al,Si})\text{O}_3$  (Tschauner et al. 2014). Perovskite has an orthorhombic  $\text{GdFeO}_3$ -type structure, where the large cation site, bicapped prism, is occupied by large  $\text{Mg}^{2+}$  and  $\text{Fe}^{2+}$  cations, while the smaller octahedra accommodate Al and Si cations. At the pressure-temperature conditions similar to those at the D'' discontinuity as experimentally observed, the perovskite-structured phase transforms to a  $\text{CaIrO}_3$  post-perovskite structured phase (Murakami 2004). In contrast to the octahedral framework in perovskite, post-perovskite's structure consists of layers of linked silica octahedra. This layered structure has been proposed to be responsible for an increase of anisotropy near the base of the mantle (Shim et al. 2008).

The second most abundant phase ( $\sim 20\%$  by volume) in the lower mantle is magnesiowüstite or ferropericlase  $(\text{Mg,Fe})\text{O}$ . The pressure-induced transition of Fe from the high-spin to the low-spin state has been shown to produce softening in elastic properties of these materials (Speziale et al. 2007). In addition to the phases mentioned above, a cubic  $\text{CaSiO}_3$  perovskite and  $\text{SiO}_2$  phases (stishovite,  $\text{CaCl}_2$  or  $\alpha\text{-PbO}_2$  structured) are stable in the lower mantle. Due to the low abundances of these phases, their effects on physical and chemical properties of the mantle materials are minor.

A schematic diagram representing the relative abundances of the different phases in the Earth's mantle is shown in Figure 2.1.1-1

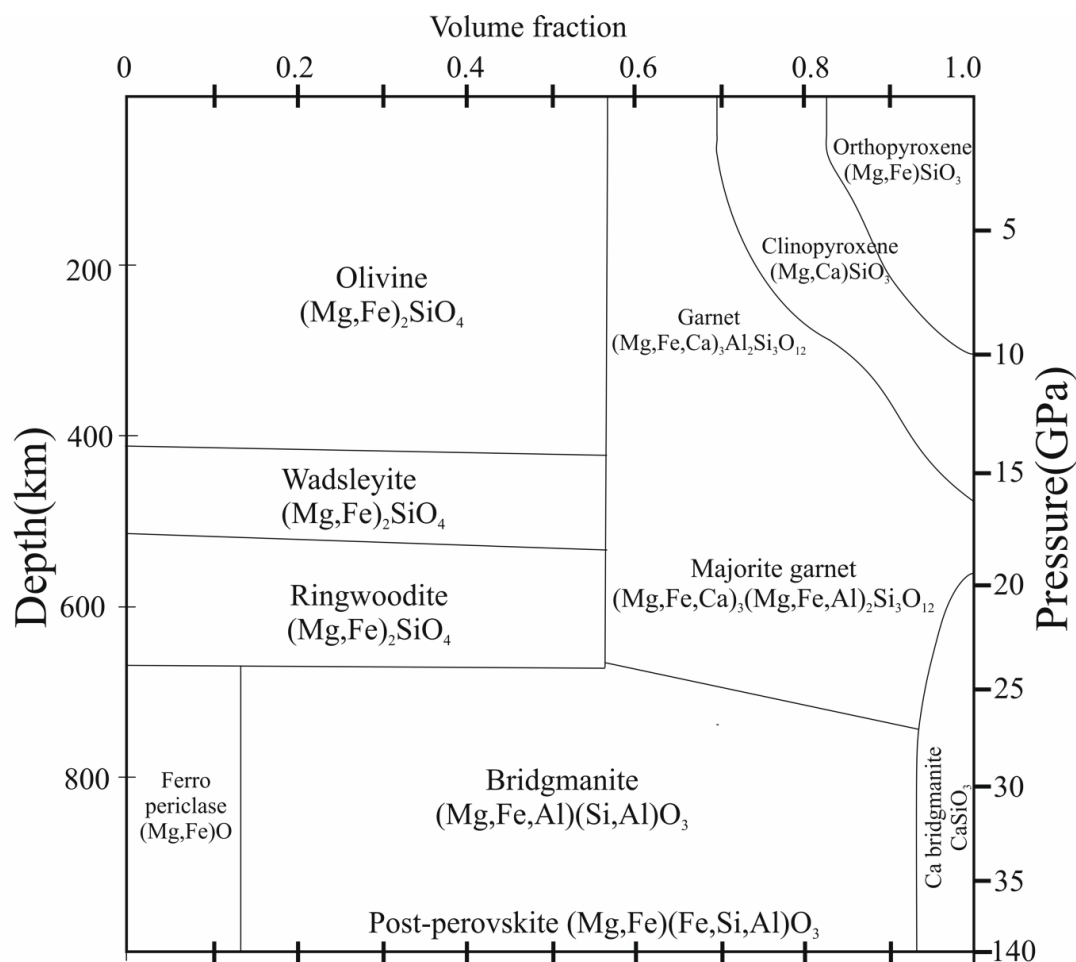


**Figure 2.1.1-1 Volume fractions and relative abundances of upper-mantle and lower-mantle minerals. Modified after Frost, 2008.**

## 1.2 Iron in selected silicate mantle minerals (garnets, perovskite and post-perovskite)

Silicate garnets are common in many geological environments and garnet-bearing assemblages are often used to estimate pressure-temperature conditions of the Earth's mantle. Making accurate estimates of geologic conditions from such assemblages requires a detailed knowledge of the physical and chemical properties of garnets

(Woodland and Ross 1994). Natural garnets are always complex solid solutions and involve substitution of divalent and trivalent cations on dodecahedral and octahedral sites, respectively. The most common Fe-bearing garnets are almandine, andradite and skiagite. The latter garnet contains iron in both ferrous ( $\text{Fe}^{2+}$ ) and ferric ( $\text{Fe}^{3+}$ ) states and can be used to estimate the oxygen fugacity (Gudmundsson and Wood 1995). The garnet  $\text{Fe}^{3+}/\Sigma\text{Fe}$  ratios in garnet-bearing peridotite xenoliths are between 2% and 13% (Canil and O'Neill 1996). Geothermometry and barometry reveals a trend of increasing garnet  $\text{Fe}^{3+}/\Sigma\text{Fe}$  ratio with temperature and pressure of equilibration (Frost and McCammon, 2008).

With dissolution of  $(\text{Mg,Fe})\text{SiO}_3$  in  $(\text{Mg,Fe,Ca})_3\text{Al}_2\text{Si}_3\text{O}_{12}$ , garnets become silica-rich with a majorite component. Upper-mantle garnets have cubic symmetry and silica exclusively occupies the tetrahedral site, while in majorite garnets, silica also enters an octahedral site along with magnesium and iron. The  $\text{MgSiO}_3$  end member of majorite has a tetragonal symmetry, a slight distortion from cubic symmetry that is due to re-ordering of Mg and Si on the octahedral sites (Angel et al. 1989). Introducing Al into the garnet is known to stabilize the cubic symmetry (Kato 1986; Hatch and Ghose 1989). Akaogi and Akimoto (1977) experimentally showed that solubility of  $\text{Fe}_4\text{Si}_4\text{O}_{12}$  in  $\text{Fe}_3\text{Al}_2\text{Si}_3\text{O}_{12}$  may extend up to a maximum of 40 mol. %, but the pure iron end-member  $\text{Fe}_4\text{Si}_4\text{O}_{12}$  is not stable. They haven't reported any structural data for these solid solutions except the extrapolated unit-cell volume. Whether iron majorite ( $\text{Fe}_4\text{Si}_4\text{O}_{12}$ ) has cubic or tetragonal symmetry, and at which compositions possible transformation occurs is unknown. As was shown by O'Neill et al. (1993), even at its minimum oxygen fugacity limit in equilibrium with metallic iron,  $(\text{Mg,Fe})_4\text{Si}_4\text{O}_{12}$  majorite contains appreciable amount of  $\text{Fe}^{3+}$  in the octahedral site, which increases with increasing oxygen fugacity.

Solubility of iron in the lower mantle bridgmanite has been shown to extend up to maximum of 75% of  $\text{FeSiO}_3$  in the deep mantle based on experimental studies (Tateno et al. 2005; Dorfman et al. 2013). Pure iron bridgmanite ( $\text{FeSiO}_3$ ) is shown to dissociate to mixtures of oxides from 20 to 150 GPa (Ming and Bassett, 1975; Dorfman et al. 2013) (Fujino et al. 2009). Bridgmanite relevant to the lower mantle contains both

ferrous and ferric iron (Andrault 2001; Murakami et al. 2012; Glazyrin et al. 2014; Kuperenko et al. 2014). The concentration of  $\text{Fe}^{3+}$  will be high even under extremely reducing conditions (Frost et al. 2004).

The Fe-enrichment of perovskite in the lower mantle can occur because of separation of dense material during differentiation (Lee et al. 2010), stagnation of Fe-rich crust (Dobson and Brodholt 2005), or reactions between the core and mantle (Knittle et al. 1991; Dubrovinsky et al. 2003). These reasons can also cause Fe-enrichment in iron-rich post-perovskite. The pressure range at which post-perovskite transition occurs is strongly dependent on the Fe and Al content and the oxidation state of Fe (Shim et al. 2008). In addition to perovskite, post-perovskite contains both  $\text{Fe}^{2+}$  and  $\text{Fe}^{3+}$ . Ferrous iron stabilizes post-perovskite relative to perovskite and the two mixture are stable over a wide pressure range (Mao et al. 2004, 2006; Tateno et al. 2005; Caracas and Cohen 2008). Single-phase post-perovskite hasn't been synthesized in Mg- Al-free pure Fe composition.

Iron is the most abundant transition element in the mantle and exists in two oxidation states ( $\text{Fe}^{2+}$  and  $\text{Fe}^{3+}$ ). At ambient conditions, both ferrous and ferric irons are in the high-spin spin electronic state, where the partially filled  $3d$  shell is dominated by unpaired electrons. With increasing pressure it becomes energetically more favorable for electrons to be paired. Spin-pairing transition can significantly affect the properties of the materials that compose the interior of our planet. Constraining the spin state of iron is therefore critical for understanding the chemistry and dynamics of the Earth's interior. High-pressure experiments such as Mössbauer spectroscopy and X-ray emission spectroscopy provide evidence for this transition. X-ray diffraction can also be a powerful technique, since we can obtain Fe-O distances and the unit-cell volume and follow them as a function of pressure.

Pressure-induced electronic spin-transition of iron occurs in lower mantle in minerals such as magnesiowüstite and bridgmanite. In ferropericlase, the spin-transition affects elasticity, density and transport properties such as electrical and thermal conductivity (Keppler et al. 2007; Lin et al. 2007; Chen et al. 2012). The spin transition in

bridgmanite may also have a significant effect on chemical heterogeneities in the lower mantle.

Studying the spin transition of iron in minerals not relevant to lower mantle is also important, because it can help find regularities in the behavior of iron. For example, Fe-bearing silicate garnets with a high cubic symmetry and high symmetry of the cations environment are perfect candidates for studying regularities of  $\text{Fe}^{3+}$  in the octahedral coordination. Recent experimental studies show pressure-induced transition in andradite ( $\text{Ca}_3\text{Fe}_2\text{Si}_3\text{O}_{12}$ ) (Friedrich et al. 2014) and in henritermierite  $\text{Ca}_3\text{Mn}_2[\text{SiO}_4]_2[\text{O}_4\text{H}_4]$  (Friedrich et al. 2015). The spin-transition of  $\text{Fe}^{3+}$  in these compounds is associated with the reduction of the  $\text{Fe}^{3+}\text{O}_6$  polyhedral volume and occurs at a pressure range between 55 and 70 GPa. This transition has a large effect on the volume and therefore on the compressibility of these materials.

## 2 METHODS

### 2.1 Methods of high pressure high temperature synthesis

#### 2.1.1 Multi anvil apparatus

To synthesize garnet, high-pressure high-temperature conditions relevant to the upper-mantle (7-9 GPa and 1100-1300°C) were generated using multi anvil apparatus in Bayreschies Geoinstitut (BGI).

The multi anvil apparatus consists of a hydraulic press generating a uniaxial force, which is applied onto a set of 6 steel anvils (first stage anvils). Assembled together, the first stage anvils form a cubic void in which a set of eight corner-truncated tungsten carbide cubes (second stage anvils) is placed. Triangle truncation faces create an octahedral high-pressure chamber, in which the pressure cell is placed. Pyrophyllite gaskets are placed between the anvils to seal the high-pressure chamber. The cubes were packed all together using epoxy-impregnated fiberglass laminate sheets, which also insure electrical insulation from the six guide block anvils. More details concerning multi anvil technique can be found in (Frost et al. 2004; Keppler and Frost 2005; Ito 2007).

The schematic of the pressure cell is shown in Figure 2.1.1.

As starting materials, we used stoichiometric mixtures of various oxides: FeO, Fe<sub>2</sub>O<sub>3</sub>, and SiO<sub>2</sub>. A capsule was made from a platinum (Pt) foil of 2 mm in diameter and 3.5 mm in length. The capsule with the starting material is enclosed into a MgO sleeve,

separating it from the heater; two MgO spacers are placed from both sides of the sample chamber, when the assembly is inside an octahedron of MgO doped with 5% Cr<sub>2</sub>O<sub>3</sub> to reduce heat loss by radiation. High temperature is generated using either graphite or LaCrO<sub>3</sub> resistive heaters. The temperature was controlled by W3%Re/W25%Re thermocouples, which were placed within a 4-hole alumina tube. During the experiment the assembly was first compressed to a desired pressure, heated up, and kept at a desired temperature for 30 minutes, then rapidly quenched to room temperature and decompressed to ambient pressure. With such strategy each run takes about 24 hours.

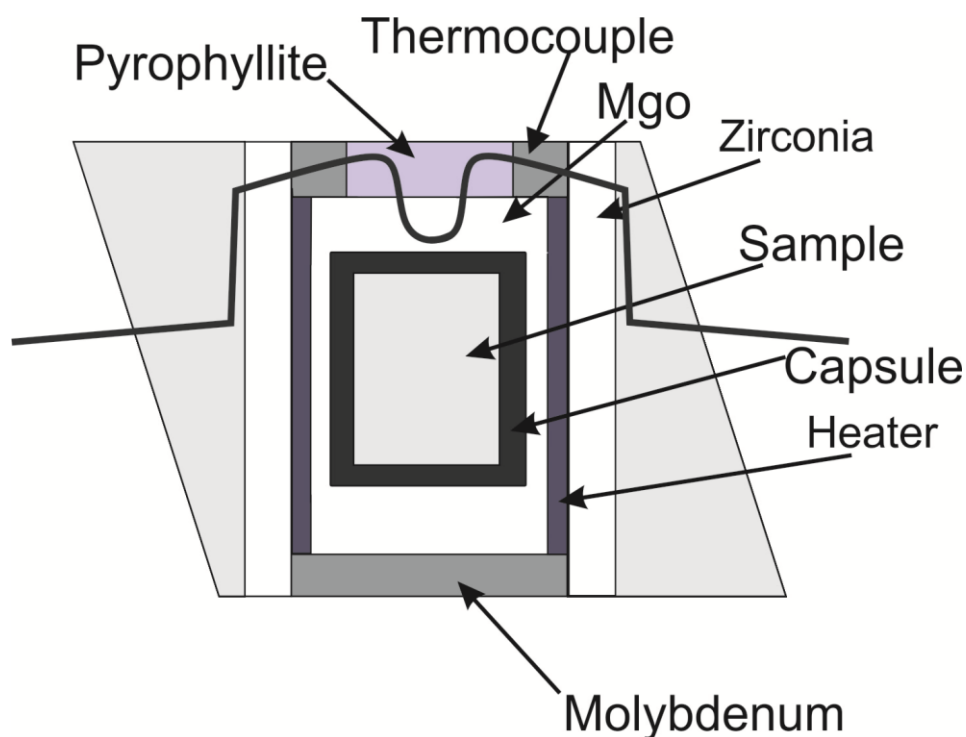


**Fig.2.1.1 Schematic section through the octahedral pressure medium employed in the 18/11 assembly.**

The great advantage of multi anvil experiments is the size of the capsule. The amount of material coming from one batch is enough for many experiments in a diamond anvil cell.

## 2.1.2 Diamond anvil cell

Characterisation of materials chemistry and physical properties at high pressures and temperatures is fundamentally important to understanding the interior of the Earth. To simulate the pressure-temperature conditions of the Earth's deep mantle and core, Mbar pressures and temperatures of several thousand K are required. The only experimental device capable of generating and maintaining these conditions is the laser-heated diamond anvil cell.

### 2.1.2.1 Principle of diamond anvil cell technique

Diamond anvil cell (DAC) is a piston-cylinder design apparatus that can generate extremely high-pressures by compressing samples between two diamonds (Fig.2.1.2-1 (a)). Diamonds are extremely strong and transparent in a wide range of electromagnetic radiation, including X-rays, gamma-rays, and visible light.

The schematic picture of a diamond anvil cell is shown in Fig. 2.1.2-1(b). Diamonds are glued to the supporting seats made of tungsten carbide. Diamonds with culets of 250  $\mu\text{m}$  are used for experiments up to 60 GPa, while diamonds with culets of 125  $\mu\text{m}$  are used for pressure generation up to 150 GPa. A 200  $\mu\text{m}$  thick rhenium gasket, pre-indented to a thickness of  $\sim 25\text{-}35$   $\mu\text{m}$ , is used to contain the sample. In the center of the indentation a hole is drilled; its diameter is usually approximately a half of the diameter of the diamond's culet.

When gasket is placed on a diamond anvil, single crystal together with a ruby chip (pressure standard) is loaded inside the experimental chamber (Fig. 2.1.2-1(c)). In order to achieve quasi-hydrostatic conditions and minimize deviatoric stress, DACs are loaded with a pressure/insulation media, such as neon. Details of the gas loading procedure can be found in Kurnosov et al. (2008). Gas loadings were done following the same procedure at BGI, European Synchrotron Radiation Facility (ESRF), and Advanced Photon Source (APS).

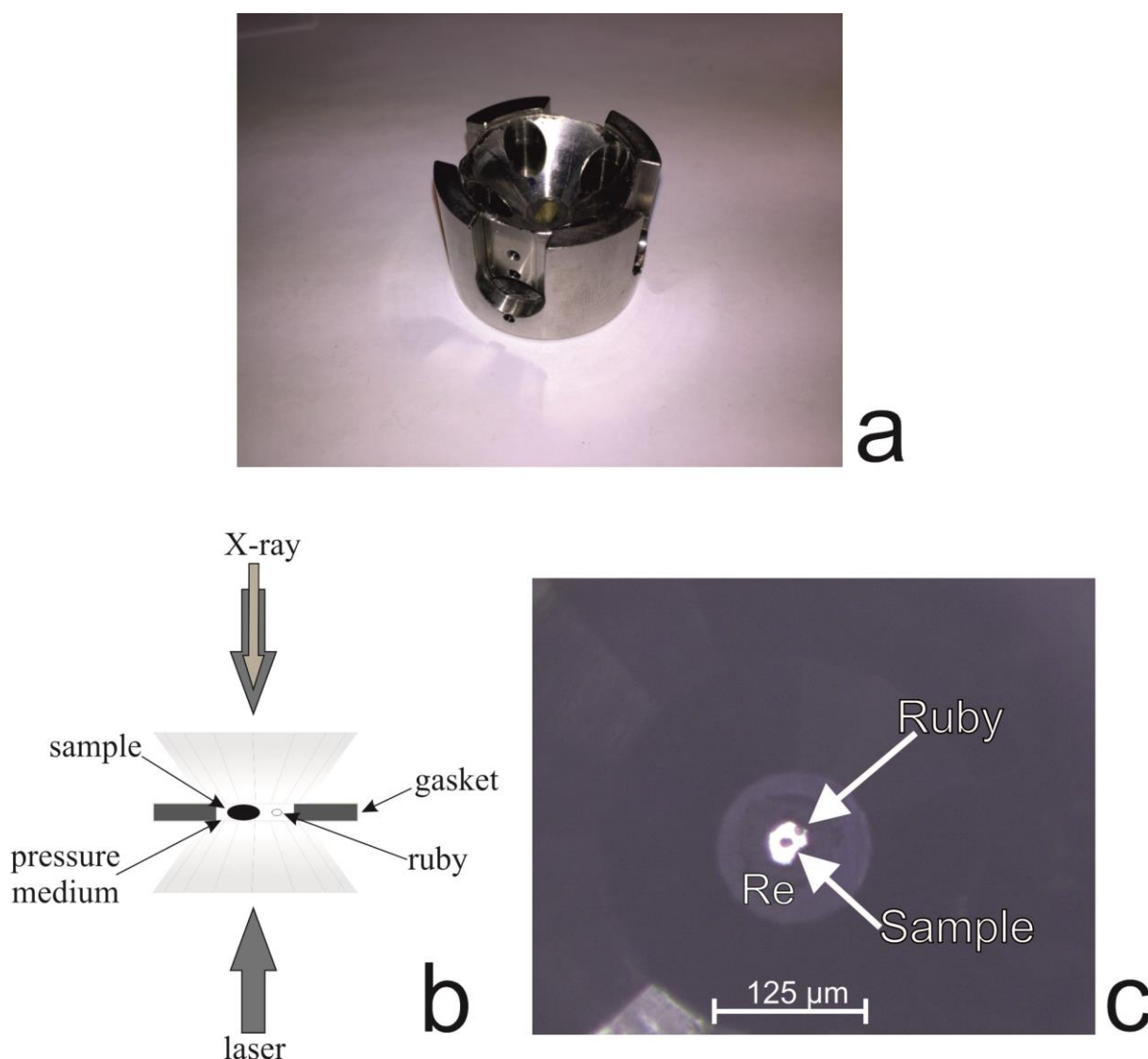


**Figure 2.1.2-1 (a) Photograph of a body of a diamond anvil cell; (b) schematic picture of a standard set up of a diamond anvil cell; (c) Microscope image of a sample and ruby inside the sample chamber drilled through rhenium (Re) gasket. View through diamond anvils.**

#### 2.1.2.2 Pressure measurement

There are different ways of measuring the pressure inside a diamond anvil cell. One of the commonly used methods involves the ruby fluorescence pressure scale. A small ruby chip of 5-10 μm in size is placed at the edge of the sample chamber. Ruby ( $\text{Cr}^{3+}$ -doped  $\text{Al}_2\text{O}_3$ ) shows a strong luminescence when excited by a red or green laser. Two

peaks dominating the luminescence spectrum shift towards higher wavenumbers upon compression. The ruby fluorescence calibration method was developed by Mao et al. (1986). The significant disadvantage of such method is weakening of the signal, when the pressure reaches Mbar conditions. As an alternative to the ruby scale, X-ray diffraction allows to measure changes in volume of standard materials. For many pressure calibrants equations of state are determined, so pressure can be calculated easily from the known lattice parameters of the material. For example, neon that serves as a quasi-hydrostatic pressure medium, solidifies at pressures of about 10 GPa and its equation of state can be used (Fei et al. 2007).

### **2.1.2.3 Laser heating**

To reach the deep Earth's interior conditions, in addition to high-pressures high-temperatures up to 3000 K should be generated. Laser heating allows achieving such high temperatures, but this technique is difficult. It requires isolation of the sample from the highly thermally conductive diamonds (common pressure-transmitting media are NaCl, LiF, Ne and He); the maintenance of a stable temperature regime is challenging, and high thermal gradient, when a sample is heated from one side of the anvil must be considered. To minimize the effect of radial temperature gradients double-side laser heating set-up developed in BGI with a Nd:YAG laser source is used (Kupenko et al. 2012). At the APS laser heating set up designed by Prakapenka et al. (2008) is used. Temperature uncertainties in laser-heated experiments are typically on the order of 100 K.

## **2.2 Analytical techniques**

### **2.2.1 Synchrotron techniques**

Synchrotron radiation is a perfect technique to investigate samples inside the diamond anvil cell due to its high brilliance and small beam size. However, the procedure of the sample preparation in DACs is challenging. To achieve Mbar pressures, the sample must not be larger than 10-20  $\mu\text{m}$  in diameter to fit in the sample chamber together with the ruby chip. Additionally, it shouldn't be thicker than 10  $\mu\text{m}$  to prevent bridging

between a pair of diamonds. Measuring small samples with small beam size (around 10  $\mu\text{m}$ ) requires a perfect alignment. The beam must remain focused on the sample while rotating the stage. Thus, alignment of the DAC should be checked at every pressure point to have reliable data coverage.

### 2.2.1.1 Synchrotron X-ray diffraction

X-ray diffraction is the primary method for the phase identification and crystal structure measurements. The Bragg's equation for constructive interference of X-rays scattered on solids is:

$$n\lambda = 2d\sin\theta,$$

Where  $\theta$  is the scattering angle,  $n$  is a positive integer,  $\lambda$  is the wavelength of an incident X-ray beam, and  $d$  is the interplanar distance for a set of crystallographic planes. Bragg's law is usually used to find the  $d$ -spacings, which can be used to calculate the lattice constants of a crystal structure (Hammond 2009).

X-ray diffraction experiments at high pressure in DACs were performed using synchrotron radiation at the ESRF (beamlines ID09A,  $\lambda = 0.415 \text{ \AA}$  and ID27,  $\lambda = 0.371 \text{ \AA}$ ), PETRA III, DESY (P02 beamline,  $\lambda = 0.2903 \text{ \AA}$ ), and the APS ( $\lambda = 0.31 \text{ \AA}$ ). Diffraction data were collected using the following data collection strategy: "wide scans" were collected during continuous rotation of DAC about  $\omega$  axes from  $+20^\circ$  to  $-20^\circ$  (step of  $40^\circ$ ) and exposure time of 2 s per frame; "step scans" were collected from  $+40^\circ$  to  $-40^\circ$  with a step of  $0.5/1^\circ$  and 1 s per frame. "Wide scans" were used for initial data checking and pressure measurements (on diffraction lines of solidified neon), and "step scans" for accurate data evaluation. Two-dimensional images were first analyzed using the Dioptas program (Prescher and Prakapenka 2015), afterwards data integration was performed using the CrysAlis Pro (Oxford Diffraction 2006) software, structure solution and refinement - using Jana2006 or SHELX (Sheldrick 2008) software. In case of powdered samples (for example, after laser heating) data evaluation was performed using GSAS (Larson and Von Dreele 2004) with the graphical interface EXPGIU (Toby 2001).

### Equation of state

High-pressure diffraction experiments provide direct measurements of the unit cell parameters and the unit cell volume of the sample. The equation of state (EOS) is a thermodynamic equation describing the state of matter under a given set of physical conditions. Measured equations of state are usually parameterized in terms of the value of the bulk modulus  $K_0$  and its pressure derivatives  $K'$ :

$$K_0 = -V_0 \left( \frac{\partial P}{\partial V} \right)_{P=0}$$

$$K'_0 = \left( \frac{\partial K}{\partial P} \right)_{P=0}$$

Parameters  $K_0$ ,  $K'_0$  corresponds to the zero-pressure.

The isothermal equation most commonly used to fit P-V data in geoscience is the Birch-Murnaghan equation.

$$P = 3K_0 f_E (1 + 2f_E)^{5/2} \left( 1 + \frac{3}{2}(K'_{0T} - 4)f_E \right. \\ \left. + \frac{3}{2} \left( K_0 K''_{0T} + (K'_{0T} - 4)(K'_{0T} - 3) + \frac{35}{9} \right) f_E^2 \right)$$

This equation is based upon assumption that the strain energy (F) of a solid under compression can be expressed as a Taylor series in the finite Eulerian strain,  $f_E = [(V_{0T}/V_{PT})^{2/3} - 1]/2$  (Birch 1947).

If this equation is truncated to 2<sup>nd</sup>-order in the energy, then the coefficient of  $f_E$  must be equal zero, which requires that the  $K'_{0T}$  is fixed to 4. The 3<sup>rd</sup> order truncation (the coefficient of  $f_E^2$  is set to 0) yields a three-parameter ( $V_{0T}$ ,  $K_{0T}$ ,  $K'_{0T}$ ) EoS with an implied value of  $K''_{0T}$ :

$$K''_{0T} = \frac{-1}{K_{0T}} \left[ (3 - K'_{0T})(4 - K'_{0T}) + \frac{35}{9} \right]$$

More detailed information about the theory of the equation of state can be found in (Angel et al. 2009). The Birch-Murnaghan equations of state coefficients were refined using the program EoSFit-7c (Angel et al. 2014).

### 2.2.1.2 Synchrotron Mössbauer source (SMS) spectroscopy

Iron is the most abundant element of the Earth. In the Earth's crust, mantle, and core complex it can exhibit three different valence states ( $\text{Fe}^0$ ,  $\text{Fe}^{2+}$ ,  $\text{Fe}^{3+}$ ). Mössbauer spectroscopy is an ideal technique to study valence and spin states of iron at high pressures in diamond anvil cells.

The Mossbauer effect is the recoilless nuclear resonant absorption of  $\gamma$ -rays. When a gamma-quantum falls to the nucleus and its energy exactly coincides with the energy level difference of two nuclear energy states, it can be absorbed and the absorbing nucleus would transform to its excited state. The measured resonance absorption line position therefore gives directly the energy difference between the different nuclear levels, characterizing many important properties of the absorbing atom from hyperfine parameters.

In order to observe resonant absorption, the energy of the initial  $\gamma$ -quantum should match that of the absorbing nucleus. The natural line width of the nuclear transition is so small that only the excited atom of the same kind (the same isotope) could be a source of Mössbauer spectroscopy. For example, a  $^{57}\text{Co}$  source is used to study Mössbauer active  $^{57}\text{Fe}$ . When the source moves towards or backwards relative to the absorber, energy shifts to a higher or lower value (Doppler effect). The absorption spectrum shows peaks related to the nuclear states. The number and position of the absorbance peaks is defined by the hyperfine parameters of studied material. They are the isomer shift (IS) – determines its centroid, and the quadrupole splitting (QS) – determines the separation of a pair of peaks. The isomer shift depends on the valence and the spin state of iron, and on the sample density, so it varies with changing pressure and temperature due to compression and thermal expansion.

The use of synchrotron radiation dictated by the fact that it is much more intense than  $\gamma$ -rays emitted by an in house radioactive source. In synchrotron Mossbauer spectroscopy (SMS), X-rays monochromatized to the resonant energy of the target nucleus are absorbed by the sample and are re-emitted with some delay.

Isomer shift and quadrupole splitting are given in the units of Doppler velocity, normally in mm/s. Due to a small sample size for high-pressure studies, starting materials should be enriched with  $^{57}\text{Fe}$  to improve Mossbauer spectra. All Mossbauer spectra were measured at ID18 beamline at the ESRF, more details can be found in (Rüffer and Chumakov 1996).

### **2.2.1.3 X-ray absorption near edge structure (XANES)**

X-ray absorption near edge structure (XANES) covers the low energy part of absorption spectra, extending 50-100 eV beyond the absorption edge. Element selectivity of the method and its sensitivity to the chemical and orbital moment of a target atom provides useful information that complements results obtained by the other techniques (e.g. XRD, Mössbauer spectroscopy). The XANES part of a spectrum contains information on the electronic structure of the absorbing atom, covalence of the chemical bonding with the nearest ligands, and characteristics of the coordination polyhedron. This information could not be extracted directly from the XANES spectra, and mostly was used for comparison between XANES spectra and theoretical calculations. XANES measurements at the Fe K-edge were performed at the energy dispersive X-ray absorption beamline ID24 at ESRF. Detailed description of the experimental setup is given elsewhere (Pascarelli et al. 2006)

### **2.2.2 Electron microprobe**

Chemical composition of the samples was characterized using wavelength- dispersive X-ray (WDX) microprobe analysis. Analyses have been performed using a JEOL JXA-8200 microprobe equipped with a tungsten cathode and WDX spectrometers. The accelerating voltage was 15 keV and beam current was 15nA. The focused beam was about 2  $\mu\text{m}$  in diameter and each analysis took of about 1 minute. Metallic Fe and quartz were used as standards for Fe and Si, respectively, with atomic number effects, absorption, and fluorescence (ZAF) correction. Analyses, which varied by more than 2 wt.% from 100 wt.% totals, were rejected from the calculations.

# 3 SYNOPSIS

In this work, I present the experimental systematic study of garnets and post-garnet phases, such as perovskite and post-perovskite in the FeO-Fe<sub>2</sub>O<sub>3</sub>-SiO<sub>2</sub> system.

During my PhD project two papers were published, one paper is current in press, and one paper is prepared to be submitted.

In this chapter I shortly overview the results presented in the 5 chapter.

In the 5.1 subsection, I present high-pressure high-temperature synthesis of single crystals of skiagite-majorite garnet with composition Fe<sub>3</sub><sup>2+</sup>(Fe<sub>0.234(2)</sub><sup>2+</sup> Fe<sub>1.532(1)</sub><sup>3+</sup> Si<sub>0.234(2)</sub><sup>4+</sup>)Si<sub>3</sub>O<sub>12</sub> realized for the first time. I characterize this material using the results of single-crystal X-ray diffraction, synchrotron Mössbauer source (SMS) spectroscopy, nuclear forward scattering (NFS), and X-ray absorption near edge structure (XANES) spectroscopies.

In the 5.2 subsection, I present synthesis of garnets with different amount of the Fe majorite component. I show that the solubility of iron majorite (Fe<sub>4</sub>Si<sub>4</sub>O<sub>12</sub>) garnet may extend up to 76 %, thus considerably extending the range of solid solutions studied before. Synchrotron single crystal X-ray diffraction up to 90 GPa shows that the increase of Fe majorite component leads to the increase of a bulk modulus. Synchrotron Mössbauer source (SMS) spectroscopy shows pressure-induced spin transition of octahedrally coordinated Fe<sup>3+</sup> at the pressure range between 50 and 60 GPa.

In the 5.3 subsection, I describe the results of the study of Fe- Al- bearing bridgmanite and the details of the synthesis of pure Fe-bridgmanite realized for the first time, as well as geophysical implications of these experiments. I show that iron in bridgmanite is stabilized by the presence of ferric iron and that iron occupies exclusively the large 12-coordinated polyhedra, while octahedral site is occupied only by silicon. The P-V data shows that compressibility of iron bridgmanite is anomalously low.

In the 5.4 subsection, I show the first synthesis of pure iron post-perovskite. I show that its density is higher than that of magnesium post-perovskite. This result suggests iron post-perovskite can contribute to ultra-low velocity zones near the core-mantle boundary.

### 3.1 High-pressure synthesis of skiagite-majorite garnet

Garnet is a common mineral in mantle assemblages and often occurs as inclusions in natural diamonds. Due to the compositional complexity of natural garnets, the relationship between their composition and the pressure-temperature conditions of their formation is still not well constrained (Akaogi and Akimoto 1977; Irifune 1987; Collerson et al. 2010; Stachel et al. 2010).

Silicate garnets have the general formula  $[X]_3[Y]_2Si_3O_{12}$  where  $[X]$  and  $[Y]$  are cations occupying the dodecahedral and octahedral sites, respectively. In garnets from the crust and upper mantle the dodecahedral site is occupied by a divalent cation (e.g.,  $Fe^{2+}$ ,  $Mg^{2+}$ ,  $Ca^{2+}$ ) and the octahedral site by a trivalent cation (e.g.,  $Fe^{3+}$ ,  $Al^{3+}$ ,  $Cr^{3+}$ ). Garnets from mantle xenoliths and inclusions in diamonds contain both ferrous ( $Fe^{2+}$ ) and ferric ( $Fe^{3+}$ ) iron. Thus, information about the properties and high-pressure behaviour of the iron end-member skiagite,  $Fe^{2+}_3Fe^{3+}_2(SiO_4)_3$ , is important for mineral physics and the geochemistry of the Earth's upper mantle and transition zone. Moreover, the fate of iron-rich silicate material incorporating a skiagite component is unknown at conditions of the deep lower mantle and the core-mantle boundary.

Synthesis experiments were performed using a split-sphere type multi-anvil apparatus at 9.5 GPa and 1100 °C at Bayerisches Geoinstitut (Bayreuth, Germany) (BGI). The starting material (corresponding to the nominal composition  $Fe_3Fe_2Si_3O_{12}$ ) was a powdered mixture of chemically pure oxides  $Fe_{1-x}O$ ,  $^{57}Fe_2O_3$ , and  $SiO_2$ . The sample was heated for about 30 min and afterwards rapidly quenched.

The composition of skiagite garnet was obtained by averaging 30 microprobe analyses (in wt% with standard deviations given in parentheses):  $SiO_2$  35.21(11),  $FeO$  60.67(9), total 95.88(14), which led to a chemical formula of  $Fe^{2+}_3$  ( $Fe^{2+}$  0.276(1)

$\text{Fe}^{3+}_{1.44(1)}\text{Si}_{0.276(1)}\text{Si}_3\text{O}_{12}$  on the basis of 12 oxygen atoms assuming stoichiometry and that the dodecahedral position is occupied exclusively by  $\text{Fe}^{2+}$ . The  $\text{Fe}^{3+}$ -corrected values of the microprobe analyses are (in wt%):  $\text{SiO}_2$  35.21(11),  $\text{FeO}$  42.11(36),  $\text{Fe}_2\text{O}_3$  20.63(80), total 97.95(88). No chemical zoning was observed in the run products. As evident from the formula, there is an excess of Si over the ideal three atoms per formula unit.

Structure refinement revealed that the octahedral site is fully occupied by Fe and Si atoms, yielding the chemical composition  $\text{Fe}_3(\text{Fe}^{2+}_{0.234(2)}\text{Fe}^{3+}_{1.532(2)}\text{Si}^{4+}_{0.234(2)})(\text{SiO}_4)_3$ , which is in good agreement with the results of electron microprobe analysis. According to the obtained structural formula, there is a significant amount of Si [0.234(2)] and  $\text{Fe}^{2+}$  [0.234(2)] on the octahedral position. This suggests that ~23 mol% of the end-member iron-majorite ( $\text{Fe}_4\text{Si}_4\text{O}_{12}$ ) component is present in the synthesized skiagite-rich garnet.

A typical SMS spectrum of skiagite-rich garnet contains two doublets that can be assigned to  $\text{Fe}^{2+}$  on the dodecahedral site and  $\text{Fe}^{3+}$  on the octahedral site. The NFS spectrum collected at ambient conditions is consistent with the SMS spectrum and the fit gave similar hyperfine parameters.

The experimental XANES spectra of skiagite-rich garnet and simulated XANES spectra for the adopted structural model suggest that the simulated spectra are representative of the experimental ones.

The structural formula obtained from EMPA and single-crystal X-ray diffraction data shows that the skiagite-rich garnet synthesized in our experiment contains excess Si and  $\text{Fe}^{2+}$  entering the Y site. The cell parameter of this garnet is higher ( $a = 11.7511$  (2) Å) compared to the one ( $a = 11.7286$  Å) reported by Woodland and O'Neil (1993) for pure skiagite. This can be explained by incorporation of the iron majorite component (23 mol %  $\text{Fe}_4\text{Si}_4\text{O}_{12}$ ) into skiagite due to the reaction  $\text{Fe}^{2+}_3\text{Fe}^{3+}_2\text{Si}_3\text{O}_{12} = 2\text{Fe}^{2+}\text{SiO}_3 + \text{Fe}^{2+}\text{Fe}^{3+}_2\text{O}_4 + \text{SiO}_2$ . Additionally, our structural data provide evidence for increase of the unit cell parameter from skiagite to iron majorite. If the data are linearly extrapolated, the unit cell parameter of iron majorite in our study is found to be  $a =$

11.833 Å, which is higher than the value obtained by Akaogi and Akimoto (1977) ( $a = 11.595$  Å) through extrapolation of iron majorite – almandine solubility data (Figure 3.1 -1).

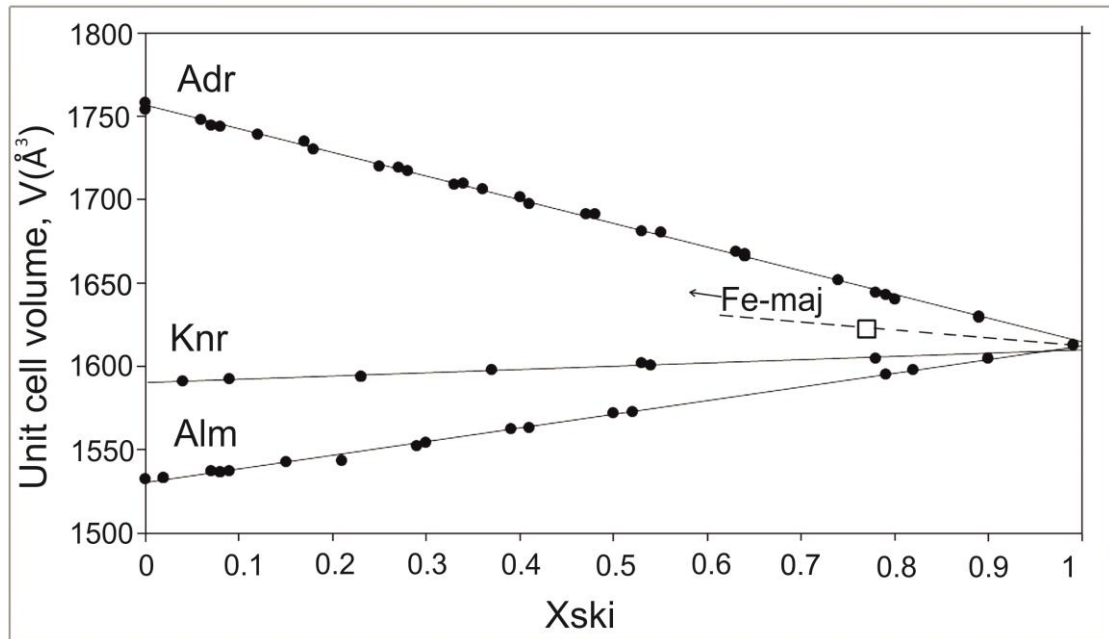


**Figure 3.1-1** Unit cell volume,  $V$ , plotted as a function of the skiagite content in andradite-skiagite, almandine-skiagite, and knorringite-skiagite solid solutions. Data for almandine-skiagite and andradite-skiagite are from Woodland and Ross (1994), and for knorringite-skiagite from Woodland et al. (2009). The open square indicates the skiagite-majorite solid solution from this study. Uncertainties are less than the size of the symbols.

Single-crystal X-ray diffraction data revealed that at least 23 mol % of iron-majorite can be dissolved in skiagite at high pressure and high temperature conditions. The relationship between skiagite and majorite provides evidence for similarity in their crystal chemical behavior, but, at the same time, suggests a consequent reaction on pressure increase. Our data motivates a detailed investigation of structural changes in the skiagite–majorite series as a function of pressure and temperature.

### 3.2 Effect of composition on compressibility of skiagite – Fe-majorite garnets.

Since garnets are among the most abundant phases in the upper mantle and transition zone, the data on their behaviour under extreme conditions plays important role in understanding of the composition, structure, and dynamics of the deep Earth's interior. While most of cations in garnets occur in a single oxidation state ( $\text{Al}^{3+}$ ,  $\text{Ca}^{2+}$ ,  $\text{Mg}^{2+}$ ,  $\text{Cr}^{3+}$ ), iron commonly occurs as both  $\text{Fe}^{2+}$  and  $\text{Fe}^{3+}$ . Skiagite garnet ( $\text{Fe}_3\text{Fe}_2\text{Si}_3\text{O}_{12}$ ) contains both  $\text{Fe}^{2+}$  and  $\text{Fe}^{3+}$  and is important for the description of phase equilibria in mantle rocks. At a great depth, skiagitic garnet accommodates an excess of Si that results in the formation of the solid solution with Fe-majorite ( $\text{Fe}_4\text{Si}_4\text{O}_{12}$ ). However, the effect(s) of majoritic substitution ( $2\text{Fe}^{3+} \leftrightarrow \text{Fe}^{2+} + \text{Si}^{4+}$ ) in the octahedral position is unknown.

Iron-bearing majorite garnets with different composition were selected for this study. Single-crystal X-ray diffraction revealed that synthesized garnets contain from 23.4(1) mol. % to 76(5) mol. % of the end member iron-majorite ( $\text{Fe}_4\text{Si}_4\text{O}_{12}$ ). An increase in Fe-majorite content causes a decrease in the molar volume of the garnet (Figure 3.2 - 1). The crystal structure refinement shows that a change in the unit-cell volume is associated with a decrease of the (Fe,Si)-O bond length in (Fe,Si) $\text{O}_6$  octahedra. With an increase of an iron-majorite component along the skiagite-majorite join from (Ski<sub>100</sub>) to (Ski<sub>24</sub>), the bond length decreases from 1.98 Å to 1.957(5) Å, and the polyhedral volume from 10.40 Å<sup>3</sup> (Ski<sub>100</sub>) to 9.9780 Å<sup>3</sup> (Ski<sub>24</sub>).

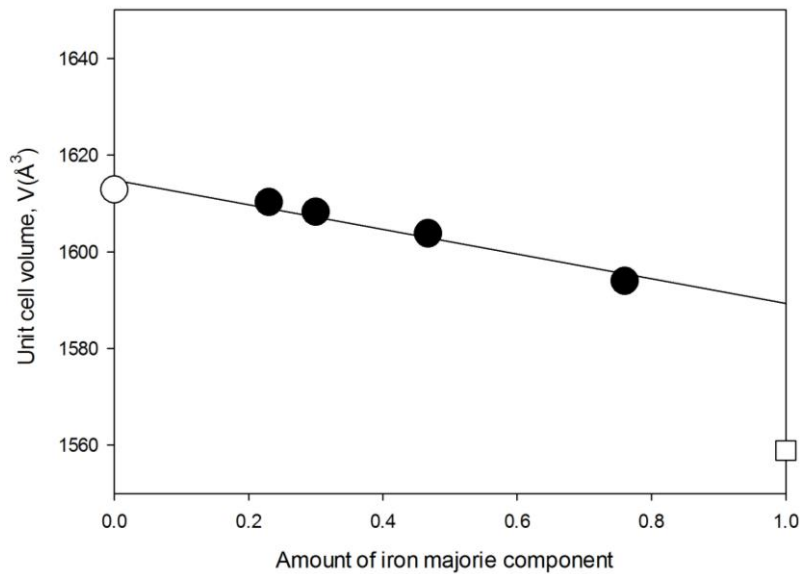


**Figure 3.2-1 Unit cell volume across the skiagite-majorite join showing the linear behavior as a function of composition. Filled circles- this study, the open circle - (Woodland and Ross 1994), the open square – pure iron majorite as obtained by extrapolation of solid solution data along the almandine-majorite join (Akaogi and Akimoto 1977). Errors are less than the size of symbols.**

The unit cell volume variations with pressure were measured for  $\text{Ski}_{76.6}\text{Maj}_{23.4}$  up to 89 GPa and for  $\text{Ski}_{69}\text{Maj}_{31}$ ,  $\text{Ski}_{54}\text{Maj}_{46}$ , and  $\text{Ski}_{24}\text{Maj}_{76}$  up to 60 GPa. For all of them the volume reduction in the interval of 40 to 50 GPa is of about 3.1-3.5 %, while between 50 and 60 GPa it is of about 4.7-5.5 %. Combining single crystal diffraction and high-pressure synchrotron Mössbauer spectroscopy results it's demonstrated that such changes in the compressional behaviour associate with changes in an electronic state of Fe in the octahedral site.

The isothermal bulk modulus and bulk sound velocities of iron majoritic garnets increases with increasing of majoritic component (Figure 3.2-2 a). Extrapolation of our data for the pure Fe-majorite composition gives the value of 6.2 km/s. It is significantly lower than any estimates for the end member of Mg-majorite (Figure 3.2-2 b).

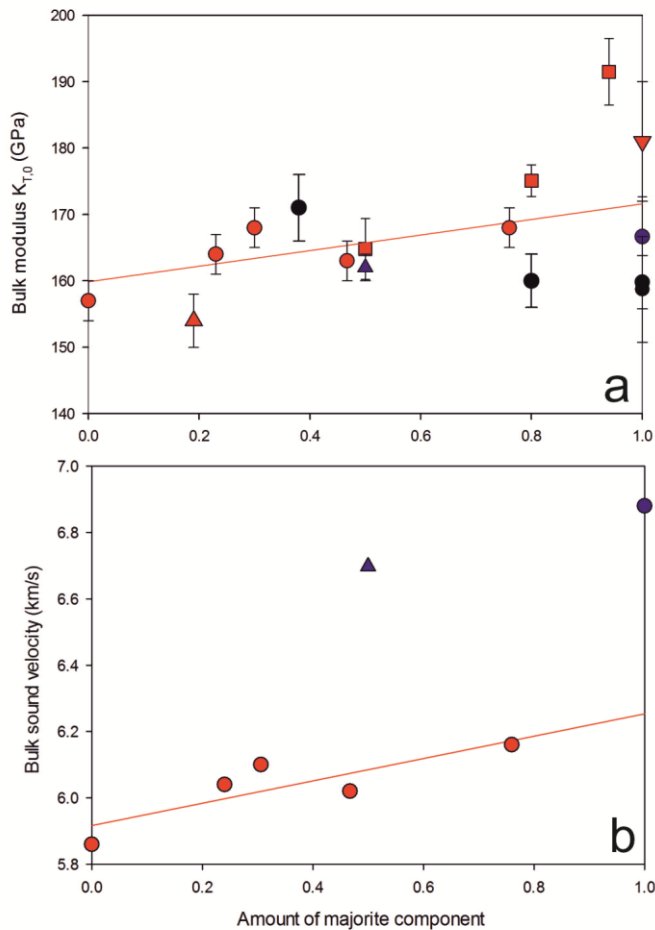


**Figure 3.2-2** Variation of isothermal bulk moduli (a) and bulk sound velocities (b) of garnets at 300 K as a function of the majorite content as revealed by the present study and literature data. Red circles – skiagite-majorite garnets (this study) and pure skiagite (Woodland et al. 1999); red squares – Ca-bearing and Na-bearing majorite (Hazen et al. 1994); red triangle up – majoritic knorringite (Dymshits et al., 2014); red triangle down – Na-majorite (Dymshits et al., 2014), blue triangle up – “pyrolite minus olivine” majorite garnet  $\text{Py}_{23}\text{Alm}_6\text{Mj}_{50}\text{Gr}_{21}$  (Irifune et al. 2008); blue circle – Mg-majorite  $\text{Mg}_4\text{Si}_4\text{O}_{12}$  (Li and Liebermann 2007); black circles – Mg-majorite garnets (Liu et al. 2000, Sinogeikin and Bass, 2000). Red lines represent linear fits of our experimental data. Error bars show the experimental uncertainties.

These results firmly establish that both the total iron content in majorite and the  $\text{Fe}^{2+}/\text{Fe}^{3+}$  ratio affect notably its elastic properties and the bulk sound velocity and have to be taken in to account in the analysis of seismological data and modeling of the composition of the Earth's upper mantle and transitions zone.

### **3.3 Stability of Fe,Al-bearing bridgmanite in the lower mantle and synthesis of pure Fe-bridgmanite**

The lower mantle constitutes more than half of the Earth's interior by volume and is believed to consist predominantly of bridgmanite (perovskite-structured  $(\text{Mg,Fe})(\text{Si,Al})\text{O}_3$ ) with up to approximately 20% ferropericlase  $(\text{Mg,Fe})\text{O}$  by volume (Murakami et al. 2012; Tschauer et al. 2014). Thus, the physical properties, crystal chemistry, and stability of bridgmanite at high pressures and temperatures are critical for understanding the structure and dynamics of our planet, as well as the interior of other terrestrial planets as well as exoplanets.

Single crystals of bridgmanite with different compositions,  $\text{Mg}_{0.83}\text{Fe}_{0.17}\text{Al}_{0.06}\text{Si}_{0.94}\text{O}_3$  (FE17),  $\text{Mg}_{0.86}\text{Fe}_{0.14}\text{Al}_{0.04}\text{Si}_{0.96}\text{O}_3$  (FE14), and  $\text{Mg}_{0.60}\text{Fe}_{0.40}\text{Si}_{0.63}\text{Al}_{0.37}\text{O}_3$  (FE40), as determined from single crystal X-ray diffraction structural refinement and microprobe analysis, were selected from samples synthesized in a multi-anvil apparatus at 25 GPa and 1300 °C. The samples were loaded in diamond anvil cells and compressed to pressures ranging from 32 to 130 GPa and heated using a double-sided laser setup at temperatures between 2200 and 3100 K over relatively long time periods ranging from 20 to 100 min.

The only observed changes upon laser heating for all investigated samples were shifts in the positions of reflections due to variations in temperature and pressure. Detailed inspection of diffraction patterns did not reveal the appearance of any non-identified reflections during or after heating. When pressure remained the same before and after laser heating, the lattice parameters of bridgmanite also remained the same within experimental uncertainty, suggesting that the integrity of the material was not affected by prolonged laser heating.

Synthetic skiagite-majorite garnet was used as starting material for experiments to study the high-pressure high-temperature behavior of Mg,Al-free Fe<sup>3+</sup>-bearing silicate with composition Fe<sup>2+</sup><sub>3</sub>(Fe<sup>2+</sup><sub>0.234(2)</sub>Fe<sup>3+</sup><sub>1.532(1)</sub>Si<sup>4+</sup><sub>0.234(2)</sub>)(SiO<sub>4</sub>)<sub>3</sub>. Laser heating of skiagite-majorite garnet in the DAC up to ~40 GPa and 1500 to 2300 K resulted in decomposition to stishovite (SiO<sub>2</sub>) and Fe<sub>4</sub>O<sub>5</sub>. Upon heating at pressures above ~45 GPa we observed different sequences of transformations. For example, at 51(1) GPa and 1800(100) K skiagite-majorite garnet decomposes to stishovite, high-pressure orthorhombic *h*-Fe<sub>3</sub>O<sub>4</sub> (Dubrovinsky et al. 2003), and perovskite-structured phase. At higher temperatures (2100(100) K diffraction lines of stishovite are absent, the intensity of reflections of *h*-Fe<sub>3</sub>O<sub>4</sub> decreases, and the diffraction pattern is dominated by perovskite phase. The same phase was synthesized by heating skiagite-majorite garnet at different pressures up to over 100 GPa. Once synthesized, the phase maintains its structure on compression up to ~125 GPa and decompression down to at least 13 GPa. Based on the results of six different experiments it can be expressed as (Fe<sup>2+</sup><sub>0.64(2)</sub>Fe<sup>3+</sup><sub>0.24(2)</sub>)Si<sub>1.00(3)</sub>O<sub>3</sub> (Figure 3.3-1)

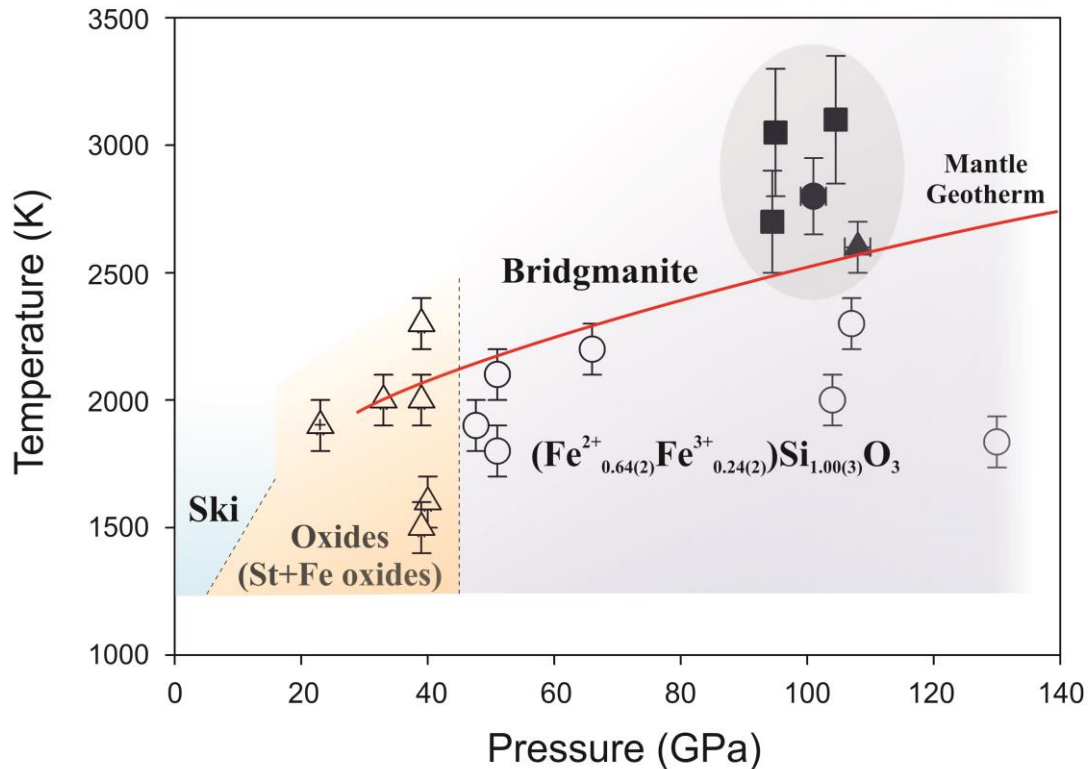


**Figure 3.3-1** Stability fields of skiaigite garnet, oxides (open triangles) and bridgmanite (Ski – skiaigite-majorite garnet  $\text{Fe}^{2+}_3(\text{Fe}^{2+}_{0.234(2)}\text{Fe}^{3+}_{1.532(1)}\text{Si}^{4+}_{0.234(2)})(\text{SiO}_4)_3$  (open circles),  $\text{Mg}_{0.86}\text{Fe}_{0.14}\text{Al}_{0.04}\text{Si}_{0.96}\text{O}_3$  (FE14, filled squares),  $\text{Mg}_{0.83}\text{Fe}_{0.17}\text{Al}_{0.06}\text{Si}_{0.94}\text{O}_3$  (FE17, filled triangle), and  $\text{Mg}_{0.60}\text{Fe}_{0.40}\text{Si}_{0.63}\text{Al}_{0.37}\text{O}_3$  (FE40, filled circle).

Ferric iron-bearing Fe-bridgmanite has a remarkable crystallochemistry. First, all iron is in the A-site and within the accuracy of determination of the occupancies of structural positions (better than 5%) there is no iron in the octahedra (B- site). Second, it is obvious that the material synthesized between 50 and 100 GPa contains a significant amount of vacancies (about 12%) at the A-site according to the substitution scheme  $3\text{Fe}^{2+} \rightarrow 2\text{Fe}^{3+} + \text{Vacancy}$  (Figure 3.3-2)

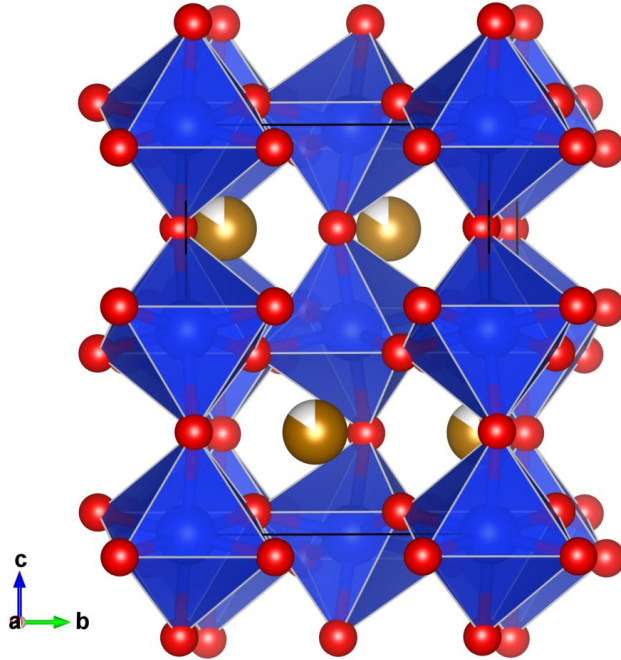


**Figure 3.3-2 Polyhedral structural model of orthorhombic bridgmanite. The bridgmanite structure (space group  $Pbmn$ , #62) has two cation positions – a distorted bi-capped prism (“A”-site, brown) and octahedra (“B-site”, blue). Vacancies in the B site indicated in white.**

The effect of pressure on the lattice parameters of  $Fe^{3+}$ -bearing Fe-bridgmanite is very different from the variation observed for any other silicate perovskites (Ballaran et al. 2012; Dorfman et al. 2012; Glazyrin et al. 2014; Kuppenko et al. 2015); in that the a- and b-axes are much more compressible. Vacancies on the A-site lead to significant softening of the material; it has a bulk modulus  $K_{300}=190(4)$  GPa ( $K'=4$ ,  $V_0=178.98(6)$   $\text{\AA}^3$ /unit cell) which is drastically lower than values known for other Fe- or/and Al-rich bridgmanites (Saikia et al. 2009; Ballaran et al. 2012; Dorfman et al. 2012, 2013; Glazyrin et al. 2014).

The estimated density and the bulk modulus of pure iron bridgmanite will be  $\rho_{80}=5.99(1)$  g/cm<sup>3</sup> and  $K_{80}=480(15)$  GPa, and bulk velocity heterogeneity parameter,

$\partial \ln V_B / \partial X_{Fe}$ , 0.16 (vs  $\sim 0.10$  in (Dorfman and Duffy 2014; Glazyrin et al. 2014)). Consequently, for oxidized parts of the lower mantle (subducted slabs, for example) and for relevant chemical compositions, the variation of  $Fe^{3+}/\Sigma Fe$  can lead to significant changes in the bulk sound velocity of bridgmanite (exceeding 2%), clearly demonstrating the importance of iron oxidation state for interpreting seismic tomography data.

### 3.4 Synthesis of pure iron post-perovskite

Since the discovery of the post-perovskite phase (ppv) in  $MgSiO_3$  (Murakami et al. 2004) it received much interest for its potential to explain seismic observations near the base of the lower mantle. The pressure range at which the post-perovskite transition occurs has been found to be raised, lowered, and/or broadened by changes in composition, depending on Fe and Al content and Fe oxidation state (Shim et al. 2008). However, pure iron post-perovskite hasn't been synthesized.

As a starting material skiagite-majorite garnets with the composition  $Ski_{77}Maj_{23}Fe^{2+}_3(Fe^{2+}_{0.234(2)}Fe^{3+}_{1.532(1)}Si^{4+}_{0.234(2)})(SiO_4)_3$  was used. Upon laser heating in diamond anvil cell of skiagite-majorite garnet at 125(1) GPa and 2500(100) K for 30 min it transformed to postperovskite (ppv) phase coexisting with perovskite (pv) structured phase (Figure 3.4-1). In the second run already synthesized single phase of iron pv was compressed to 146(1) GPa and laser-heated at 2500(100) K, it transformed to a single post-perovskite phase (Figure 3.4-2).

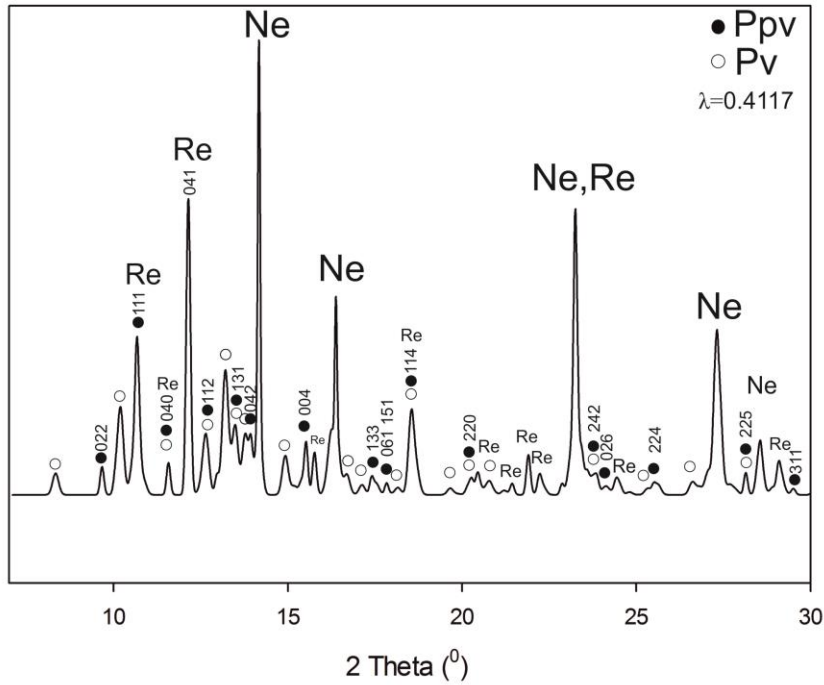


**Figure 3.4-1 X-ray diffraction pattern for skiagite-majorite postperovskite at 125(1) GPa. Filled circles – post perovskite, empty circles – iron perovskite, Re- reneium gasket, Ne- pressure medium**

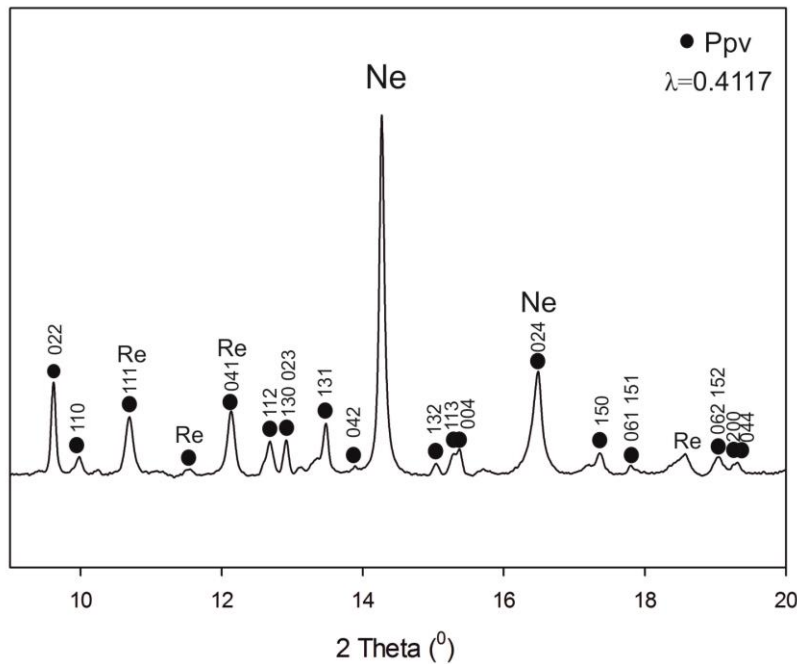


**Figure 3.4-2 X-ray diffraction pattern for skiaigite-majorite postperovskite at 146(1) GPa. Filled circles – post perovskite, Re- rhenium gasket, Ne- pressure medium. Background was subtracted.**

Comparing data in this study with previous data reported on ppv volumes with variable Fe content at ~125 GPa and 300 K at 125 GPa, the volume increases by 3.5 % from pure iron post-perovskite to Fe-free  $\text{MgSiO}_3$  by (Guignot et al. 2007). The data show the trend with increasing Fe content the volume increases, reaching it maximum with studied pure iron post-perovskite. If synthesized post-perovskite retains the same chemical compositions as an initial skiaigite-majorite garnet, calculated density ( $\rho_{127}$ ) will be  $6.736 \text{ g/cm}^3$ , which is higher than the value for pure Mg post-perovskite.

The incorporation of iron in silicate post-perovskite increases the density and, consequently, may result in a decrease of bulk sound velocity. Thus affinity of Fe to ppv as demonstrated by synthesis of pure Fe-ppv support the idea that Fe-ppv is

responsible (or at least contribute) in to formation of ultra-low velocity of the base of the mantle.

# 4 LIST OF MANUSCRIPTS AND INDIVIDUAL CONTRIBUTION OF ALL AUTHORS

Paper 1:

Leyla Ismailova, Andrey Bobrov, Maxim Bykov, Elena Bykova, Valerio Cerantola, Innokenty Kantor, Ilya Kuppenko, Catherine McCammon, Vadim Dyadkin, Dmitry Chernyshov, Sakura Pascarelli, Aleksandr Chumakov, Natalia Dubrovinskaia and Leonid Dubrovinsky High-pressure synthesis of skiagite-majorite garnet and investigation of its crystal structure. *American Mineralogist*, 100, (2015)

L.I. synthesized samples, performed microprobe analyses and selected crystal for X-ray diffraction study. L.I.,M.B., E.B.,V.D.,D.M performed synchrotron single crystal X-ray diffraction. L.I.,V.C.,I.K.,C.M.,S.P.,A.C. collected and assisted with SMS,NFS, XANES synchrotron X-ray measurements. I.K. performed the simulation of XANES spectra. L.I.,A.V.,C.M.,N.D and L.D interpreted the results and wrote the manuscript with contributions of all authors.

I contributed 80% to this work.

Paper 2:

Leyla Ismailova, Maxim Bykov, Elena Bykova, Andrey Bobrov, I.Kuppenko, Valerio Cerantola, Denis Vasiukov, Natalia Dubrovinskaia, Catherine McCammon, Konstantin Glazyrin, Hans-Peter Lierman, Michael Hanfland, Alexander Chumakov, Leonid Dubrovinsky. Effect of composition on compressibility of skiagite-Fe-majorite garnets. *American Mineralogist*, in press

L.I. and A.B. synthesized all starting materials. L.I.,M.B.,E.B. performed synchrotron single crystal X-ray diffraction experiments and analysed the data. K.G., H.P., M.H. assisted at synchrotron X-ray diffraction experiments. L.I., I.K.,V.C. collected synchrotron mössbauer source spectra. L.I., D.V., C.M. interpreted Mössbauer spectra. A.C. assisted at synchrotron mössbauer source spectra collection. L.I., A.V., L.D., N.D. and C.M. wrote the manuscript.

I contributed 80% to this work

Paper 3:

Leyla Ismailova, Elena Bykova, Maxim Bykov, Valerio Cerantola, Catherine McCammon, Tiziana Boffa Ballaran, Andrei Bobrov, Ryosuke Sinmyo, Natalia Dubrovinskaia, Konstantin Glazyrin, Hans-Peter Liermann, Ilya Kuppenko, Michael Hanfland, Clemens Prescher, Vitali Prakapenka, Volodymyr Svitlyk, Leonid Dubrovinsky. Stability of Fe,Al-bearing bridgmanite in the lower mantle and synthesis of pure Fe-bridgmanite. *Science Advances* 2016 2: e1600427

L.I., L.D. and N.D. conceptualized, planned, designed, and coordinated the research; L.I., R.S., M.C., and A.B. synthesized and characterized the starting materials; E.B., M.B., L.I., V.C., C.M., H.-P.L., I.K., M.H., C.P.,V.P.,V.S. conducted synchrotron X-ray diffraction experiments; E.B., L.I., L.D., and T.B.B. performed X-ray diffraction analyses; L.I.,E.B., and L.D. prepared figures; L.D. and L.I. wrote the manuscript. All authors discussed the results and commented on the paper.

I contributed 70% to this work

Paper 4:

Leyla Ismailova, Maxim Bykov, Elena Bykova, Natalia Dubrovinskaia, Michael Hanfland, Leonid Dubrovinsky. Synthesis of pure iron post-perovskite. *To be submitted to American Mineralogist*.

L.I.,M.B.,E.B.,L.D collected and analysed X-ray diffraction data. M.H. assisted at synchrotron experiments. L.I. wrote the manuscript with further improvement by N.D. and L.D.

I contributed 80% to this work.

# 5 RESULTS

## 5.1 High-pressure synthesis of skiagite-majorite garnet and investigation of its crystal structure

Leyla Ismailova<sup>1,2</sup>, Andrey Bobrov<sup>3</sup>, Maxim Bykov<sup>1</sup>, Elena Bykova<sup>1,2</sup>, Valerio Cerantola<sup>2</sup>, Innokenty Kantor<sup>4</sup>, Ilya Kupenko<sup>4</sup>, Catherine McCammon<sup>2</sup>, Vadim Dyadkin<sup>4</sup>, Dmitry Chernyshov<sup>4</sup>, Sakura Pascarelli<sup>4</sup>, Aleksandr Chumakov<sup>4</sup>, Natalia Dubrovinskaia<sup>1</sup> and Leonid Dubrovinsky<sup>2</sup>

<sup>1</sup>Laboratory of Crystallography, Universität Bayreuth, 95447 Bayreuth, Germany

<sup>2</sup>Bayerisches Geoinstitut, Universität Bayreuth, 95447 Bayreuth, Germany

<sup>3</sup>Department of Petrology, Geological Faculty, Moscow State University, 119234 Moscow, Russia

<sup>4</sup>ESRF, European Synchrotron Radiation Facility, CS40220 38043 Grenoble Cedex 9, France

*Published in American Mineralogist, Volume 100, pages 2650-2654, 2015*

### Abstract

Skiagite-rich garnet was synthesized as single crystals at 9.5 GPa and 1100 °C using a multi-anvil apparatus. The crystal structure [cubic, space group  $Ia\bar{3}d$ ,  $a = 11.7511(2)$  Å,  $V = 1622.69(5)$  Å<sup>3</sup>,  $D_{\text{calc}} = 4.4931$  g/cm<sup>3</sup>] was investigated using single-crystal synchrotron X-ray diffraction. Synchrotron Mössbauer source spectroscopy revealed that Fe<sup>2+</sup> and Fe<sup>3+</sup> predominantly occupy dodecahedral (X) and octahedral (Y) sites, respectively, as expected for the garnet structure, and confirmed independently using nuclear forward scattering. Single-crystal X-ray diffraction suggests the structural formula of the skiagite-rich garnet to be  $\text{Fe}_3^{2+}(\text{Fe}_{0.234(2)}^{2+} \text{Fe}_{1.532(2)}^{3+} \text{Si}_{0.234(2)}^{4+})(\text{SiO}_4)_3$ , in agreement with electron microprobe chemical analysis. The formula is consistent

with X-ray absorption near-edge structure spectra. The occurrence of Si and Fe<sup>2+</sup> in the octahedral Y-site indicates the synthesized garnet to be a solid solution of end-member skiagite with ~23 mol% of the Fe-majorite end-member Fe<sub>3</sub><sup>2+</sup>(Fe<sup>2+</sup>Si<sup>4+</sup>)(SiO<sub>4</sub>)<sub>3</sub>.

**Keywords:** Skiagite, majorite, garnets, single-crystal X-ray diffraction, Mössbauer spectroscopy, nuclear forward scattering, XANES

### 5.1.1 Introduction

Garnet is a common mineral in mantle assemblages and often occurs as inclusions in natural diamonds. Due to the compositional complexity of natural garnets, the relationship between their composition and the pressure-temperature conditions of their formation is still not well constrained (Akaogi and Akimoto 1977; Irifune 1987; Collerson et al. 2010; Stachel et al. 2010).

Silicate garnets have the general formula [X]<sub>3</sub>[Y]<sub>2</sub>Si<sub>3</sub>O<sub>12</sub> where [X] and [Y] are cations occupying the dodecahedral and octahedral sites, respectively. In garnets from the crust and upper mantle the dodecahedral site is occupied by a divalent cation (e.g., Fe<sup>2+</sup>, Mg<sup>2+</sup>, Ca<sup>2+</sup>) and the octahedral site by a trivalent cation (e.g., Fe<sup>3+</sup>, Al<sup>3+</sup>, Cr<sup>3+</sup>). Garnets from mantle xenoliths and inclusions in diamonds contain both ferrous (Fe<sup>2+</sup>) and ferric (Fe<sup>3+</sup>) iron. Thus information about the properties and high-pressure behavior of the iron end-member skiagite, Fe<sub>3</sub><sup>2+</sup>Fe<sub>2</sub><sup>3+</sup>(SiO<sub>4</sub>)<sub>3</sub>, is important for mineral physics and the geochemistry of the Earth's upper mantle and transition zone. Moreover, the fate of iron-rich silicate material incorporating a skiagite component is unknown at conditions of the deep lower mantle and the core-mantle boundary.

The stability field of skiagite has been investigated in several studies. Karpinskaya et al. (1982) were probably the first to synthesize skiagite, which was produced at 12 GPa and 800 °C. Woodland and O'Neill 1993 measured the variation of garnet unit-cell parameter along the almandine-skiagite solid solution join. Woodland and Ross 1994 studied the crystal chemistry of skiagite solid solutions along the joins Fe<sub>3</sub>Al<sub>2</sub>(SiO<sub>4</sub>)<sub>3</sub>–Fe<sub>3</sub>Fe<sub>2</sub>(SiO<sub>4</sub>)<sub>3</sub> (almandine-skiagite) and Ca<sub>3</sub>Fe<sub>2</sub>(SiO<sub>4</sub>)<sub>3</sub>–Fe<sub>3</sub>Fe<sub>2</sub>(SiO<sub>4</sub>)<sub>3</sub> (andradite-skiagite) at pressures between 1.7 and 9.7 GPa and temperatures of 1080 to 1100 °C. Woodland and O'Neill 1995 investigated the stability of Ca-bearing garnets on the join

$\text{Ca}_3\text{Fe}_2(\text{SiO}_4)_3$ – $\text{Fe}_3\text{Fe}_2(\text{SiO}_4)_3$  (andradite-skiagite) as a function of pressure at 1100 °C. Simple  $\text{Cr}^{3+}$ - $\text{Fe}^{3+}$  exchange in the octahedral sites of the skiagite–Fe-knorringite [ $\text{Fe}_3\text{Fe}_2(\text{SiO}_4)_3$ – $\text{Fe}_3\text{Cr}_2(\text{SiO}_4)_3$ ] binary join was studied by (Woodland et al. 2009). However, so far the iron-skiagite end-member has not yet been synthesized so that it can be investigated by mineral physics methods, including single-crystal X-ray diffraction and Mössbauer spectroscopy.

Here we report the high-pressure high-temperature synthesis of single crystals of skiagite-rich garnet,  $\text{Fe}_3^{2+}(\text{Fe}_{0.234(2)}^{2+}\text{Fe}_{1.532(2)}^{3+}\text{Si}_{0.234(2)}^{4+})(\text{SiO}_4)_3$ , and the results of its characterization using single-crystal synchrotron X-ray diffraction, synchrotron Mössbauer source (SMS) spectroscopy, nuclear forward scattering (NFS), and X-ray absorption near-edge structure (XANES) spectroscopies.

### 5.1.2 Experimental methods

Synthesis experiments were performed using a split-sphere type multi-anvil apparatus at 9.5 GPa and 1100 °C at Bayerisches Geoinstitut (Bayreuth, Germany) (BGI). The starting material (corresponding to the nominal composition  $\text{Fe}_3\text{Fe}_2\text{Si}_3\text{O}_{12}$ ) was a powdered mixture of chemically pure oxides ( $\text{Fe}_{1-x}\text{O}$ ,  $^{57}\text{Fe}_2\text{O}_3$ , and  $\text{SiO}_2$ ) homogenized at room temperature by milling in a mortar using ethanol and then dried in a furnace at 100 °C for 24 h. The prepared mixture was placed in a capsule of 3.5 mm length and 2 mm diameter made of platinum foil. High temperature was generated using a  $\text{LaCrO}_3$  heater and the capsule was insulated from the heater by a MgO cylinder. The cell assembly with the sample was compressed to the target pressure between eight cubic tungsten carbide anvils with corners truncated to 11.0 mm edge lengths. The accuracy in determination of pressure and temperature is estimated to be  $\pm 0.5$  GPa and  $\pm 50$  °C, respectively (Frost et al. 2004).

The sample was heated for about 30 min and rapidly quenched by switching off the power supply, causing cooling to ambient temperature with a rate of  $\sim 200$  °C/s. Chemical composition of the samples was characterized using wavelength- dispersive X-ray (WDX) microprobe analysis (JEOL JXA-8200; focused beam; accelerating voltage of 15 keV and beam current of 15 nA). Metallic Fe and quartz were used as

standards for Fe and Si, respectively, with atomic number effects, absorption, and fluorescence (ZAF) correction. SMS spectra were recorded at the Nuclear Resonance Beamline (Rüffer and Chumakov 1996) ID18 of the European Synchrotron Radiation Facility (ESRF) (Grenoble, France) using the (111) Bragg reflection of a  $^{57}\text{FeBO}_3$  single crystal mounted on a Wissel velocity transducer driven with a sinusoidal wave form (Potapkin et al. 2012). The X-ray beam was focused to 20 mm vertical and 10 mm horizontal dimensions using Kirkpatrick-Baez mirrors. The line width of the SMS and the absolute position of the center shift (CS) were controlled before and after each measurement using a  $\text{K}_2\text{Mg}^{57}\text{Fe}(\text{CN})_6$  reference single line absorber. The velocity scale was calibrated using 25 mm thick natural  $\alpha$ -Fe foil. Each spectrum took  $\sim 1\text{--}2$  h to collect. Spectra were fitted using a full transmission integral with a normalized Lorentzian-squared source lineshape using the MossA software package (Prescher et al. 2012).

NFS data were collected at the same beamline in 4-bunch mode, with the beam focused to  $6 \times 11 \text{ mm}^2$  using Kirkpatrick-Baez mirrors. The spectra were collected for 10 to 60 min each. NFS data were fitted using the CONUSS package (Sturhahn 2000).

XANES spectra were collected at the energy-dispersive X-ray absorption spectroscopy beamline (ID24) at ESRF. The beam was focused horizontally using a curved polychromator Si (111) crystal in Bragg geometry and vertically with Kirkpatrick-Baez (KB) mirrors. The size of the X-ray beam spot on the sample was about  $3.5 \times 5 \text{ mm}^2$  FWHM. The measured XANES spectra were normalized using FDMNES software (Bunau and Joly 2009). The second-order polynomial pixel to energy conversion parameters were calibrated using a reference  $\alpha$ -Fe foil. Crystals for all studies were selected at BGI using a three-circle Bruker diffractometer equipped with a SMART APEX CCD detector and a high-brilliance Rigaku diffractometer equipped with a rotating anode (Rotor Flex FR-D, MoK $\alpha$  radiation), Osmic focusing X-ray optics, and Bruker Apex CCD detector.

Single-crystal X-ray diffraction data were collected at the Swiss-Norwegian beamline (BM01A) at ESRF on a single-crystal diffractometer (KUMA KM6-CH) by  $360^\circ \varphi$

scans ( $\Delta\phi = 0.5^\circ$ ) employing a Pilatus 2M pixel detector. The crystal was cooled to 280 K using an Oxford Cryostream low-temperature device. Data processing (peak intensity integration, background evaluation, cell parameters, space group determination, and absorption correction) was performed with the CrysAlis Pro 171.36.28 program. The program JANA2006 was used for structure refinement (Petříček et al. 2014).

### **5.1.3 Results and discussion**

#### **5.1.3.1 Phase assemblage and chemical composition**

The recovered sample is a multi-phase assemblage that includes fine anhedral garnet crystals that appear red under a light microscope and typically have dimensions less than  $30 \times 10 \times 10 \text{ mm}^3$ . There are also minor amounts of magnetite, coesite, and clinopyroxene Figure 5.1.3-1 that were confirmed by X-ray diffraction data and microprobe analysis. The presence of other phases in addition to garnet may indicate a non-homogeneous pressure-temperature distribution within the pressure chamber and/or different kinetics of chemical reactions in the starting mixture.

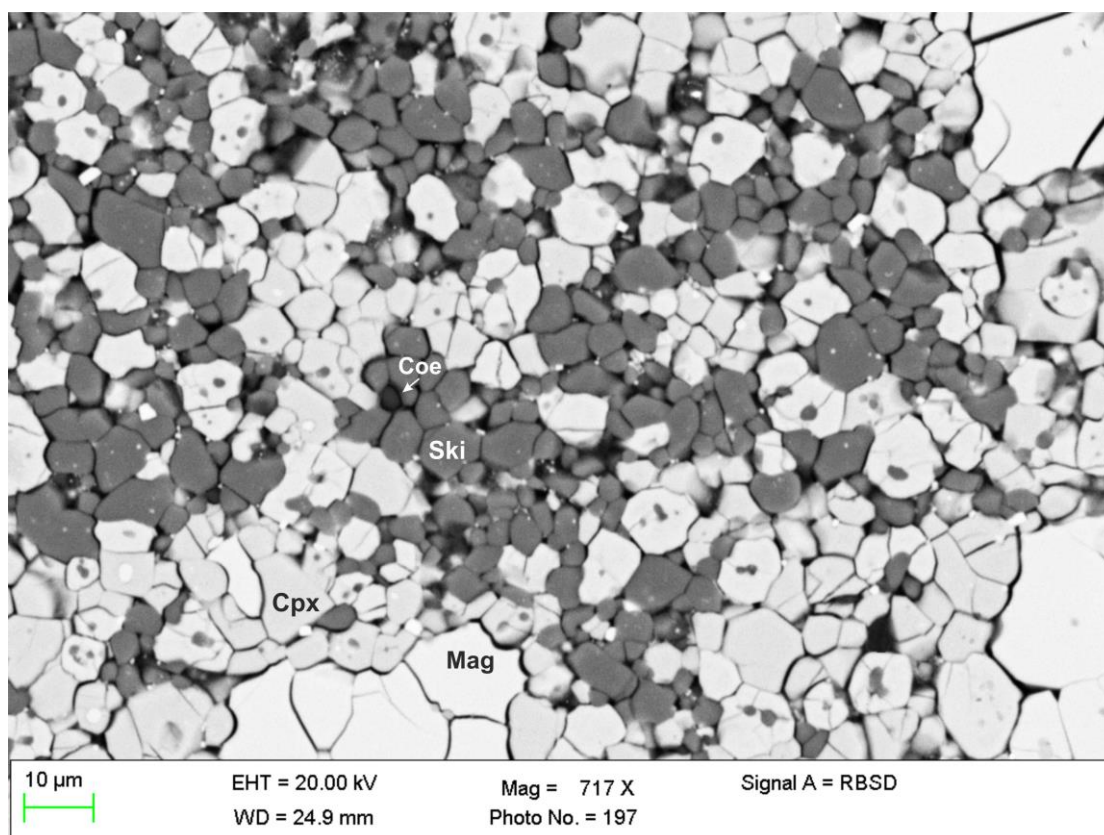


**Figure 5.1.3-1 Backscattered electron image of the sample (S5962) synthesized at 9.5 GPa and 1100 °C consisting of skiagite-rich garnet (Ski = gray), clinopyroxene (Cpx = light gray), coesite (Coe = black), and magnetite (Mag = white).**

The composition of skiagite garnet was obtained by averaging 30 microprobe analyses (in wt% with standard deviations given in parentheses): SiO<sub>2</sub> 35.21(11), FeO 60.67(9), total 95.88(14), which led to a chemical formula of Fe<sup>2+</sup><sub>3</sub> (Fe<sup>2+</sup> 0.276(1) Fe<sup>3+</sup> 1.44(1) Si<sub>0.276(1)</sub>) Si<sub>3</sub>O<sub>12</sub> on the basis of 12 oxygen atoms assuming stoichiometry and that the dodecahedral position is occupied exclusively by Fe<sup>2+</sup>. The Fe<sup>3+</sup>-corrected values of the microprobe analyses are (in wt%): SiO<sub>2</sub> 35.21(11), FeO 42.11(36), Fe<sub>2</sub>O<sub>3</sub> 20.63(80), total 97.95(88). No chemical zoning was observed in the run products. As evident from the formula, there is an excess of Si over the ideal three atoms per formula unit.

### 5.1.3.2 Single-crystal X-ray diffraction and structure refinement

The experimental details and crystallographic data obtained by means of synchrotron X-ray diffraction from a small (red) crystal of skiagite garnet are summarized . Fractional atomic coordinates and isotropic or equivalent isotropic displacement parameters ( $\text{\AA}^2$ ), atomic displacement parameters ( $\text{\AA}^2$ ), selected geometric parameters (in angstroms and degrees) are listed in Table 5.1.3 2-4. Full-matrix least-squares refinement on F provided good reliability factors  $RF[I > 3s(I)] = 0.0281$  and  $wRF(\text{all}) = 0.0427$ . Atomic coordinates and anisotropic displacement parameters of Fe1 and Si1 were constrained to be equal, and their overall occupancy was fixed. Structure refinement revealed that the octahedral site is fully occupied by Fe and Si atoms, yielding the chemical composition  $\text{Fe}_3(\text{Fe}^{2+}_{0.234(2)}\text{Fe}^{3+}_{1.532(2)}\text{Si}^{4+}_{0.234(2)})(\text{SiO}_4)_3$ , which is in good agreement with the results of electron microprobe analysis. The minor difference in the chemical composition determined by these two methods is likely due to the bulk averaging of the microprobe data compared to the diffraction data that measures a single crystal; therefore, the values obtained from single-crystal X-ray diffraction are considered to be more representative. According to the obtained structural formula, there is a significant amount of Si [0.234(2)] and  $\text{Fe}^{2+}$  [0.234(2)] on the octahedral position. This suggests that ~23 mol% of the end-member iron-majorite ( $\text{Fe}_4\text{Si}_4\text{O}_{12}$ ) component is present in the synthesized skiagite-rich garnet.

**Table 5.1.3-1 Crystal data and structure refinement**

Chemical formula	$\text{Fe}^{2+}_3(\text{Fe}^{2+}_{0.234}\text{Fe}^{3+}_{1.532}\text{Si}_{0.234})\text{Si}_3\text{O}_{12}$
Formula weight (g/mol)	548.98
Crystal system, space group	Cubic, $Ia\bar{3}d$
Temperature (K)	280.0(1)
$a$ (Å)	11.7511 (2)
$V$ (Å <sup>3</sup> )	1622.69 (5)
$Z$	8
Radiation type	Synchrotron, $\lambda = 0.6946$ Å
$\mu$ (mm <sup>-1</sup> )	10.997
Crystal size (mm)	$0.02 \times 0.019 \times 0.01$
Density (calculated)	4.494 g/cm <sup>3</sup>
Data collection	
Absorption correction	Multi-scan (SCALE3 ABSPACK)
$T_{\min}, T_{\max}$	0.730, 1
No. of measured, independent and observed [ $I > 3\sigma(I)$ ] reflections	5517, 255, 215
$R_{\text{int}}$	0.028
$(\sin \theta/\lambda)_{\max}$ (Å <sup>-1</sup> )	0.763
$R_F[I > 3\sigma(I)]$ , $wR(\text{all})$ , $S$	0.028, 0.043, 2.33
No. of reflections	255
No. of parameters	18

$\Delta\rho_{\max}, \Delta\rho_{\min}$ (eÅ <sup>-3</sup> )	0.63, -0.69
--	-------------

**Table 5.1.3-2 Fractional atomic coordinates and equivalent isotropic ( $U_{\text{eq}}$ ) displacement parameters (Å<sup>2</sup>)**

	X	Y	Z	$U_{\text{eq}}$	Occupancy
Fe2	1/8	0	1/4	0.0122(2)	
Fe1	0	0	0	0.0077(2)	0.883(7)
Si2	3/8	0	1/4	0.0085(3)	
O1	0.03501(15)	0.05281(15)	0.65693(15)	0.0112(5)	
Si1	0	0	0	0.0077(2)	0.117(7)

**Table 5.1.3-3 Atomic displacement parameters (Å<sup>2</sup>)**

	$U^{11}$	$U^{22}$	$U^{33}$	$U^{12}$	$U^{13}$	$U^{23}$
Fe2	0.0081 (4)	0.0143 (3)	0.0143 (3)	0	0	0.0012 (3)
Fe1	0.0077 (4)	0.0077 (4)	0.0077 (4)	0.00007(17)	0.00007(17)	0.00007(17)
Si2	0.0072 (6)	0.0092 (4)	0.0092 (4)	0	0	0
O1	0.0109 (8)	0.0126 (8)	0.0100 (8)	0.0010 (7)	-0.0007 (7)	-0.0001 (6)
Si1	0.0077 (4)	0.0077 (4)	0.0077 (4)	0.00007(17)	0.00007(17)	0.00007(17)

**Table 5.1.3-4 Selected geometric parameters: interatomic distances (Å), bond angles in degrees.**

Fe2—Fe1	3.2845 (19)	Fe2—O1 <sup>ii</sup>	2.3831 (17)
Fe2—Si2	2.9378 (10)	Fe1—O1 <sup>iii</sup>	1.9888 (17)
Fe2—O1 <sup>i</sup>	2.2620 (18)	Si2—O1 <sup>i</sup>	1.6430 (18)
O1 <sup>iv</sup> —Fe2—O1 <sup>i</sup>	115.19 (6)	O1 <sup>i</sup> —Fe2—O1 <sup>viii</sup>	123.62 (6)
O1 <sup>v</sup> —Fe2—O1 <sup>i</sup>	71.69 (6)	O1 <sup>i</sup> —Fe2—O1 <sup>ii</sup>	73.03 (6)
O1 <sup>v</sup> —Fe2—O1 <sup>ii</sup>	111.13 (6)	O1 <sup>viii</sup> —Fe2—O1 <sup>ii</sup>	161.88 (6)
O1 <sup>vi</sup> —Fe2—O1 <sup>i</sup>	93.00 (6)	O1 <sup>ix</sup> —Fe1—O1 <sup>iii</sup>	91.89 (7)
O1 <sup>vi</sup> —Fe2—O1 <sup>ii</sup>	71.89 (6)	O1 <sup>x</sup> —Fe1—O1 <sup>xi</sup>	88.11 (7)
O1 <sup>vii</sup> —Fe2—O1 <sup>i</sup>	67.55 (6)	O1 <sup>xi</sup> —Fe1—O1 <sup>iii</sup>	180.0 (5)
O1 <sup>vii</sup> —Fe2—O1 <sup>viii</sup>	73.03 (6)	O1 <sup>xii</sup> —Si2—O1 <sup>i</sup>	114.47 (9)
O1 <sup>vii</sup> —Fe2—O1 <sup>ii</sup>	123.62 (6)	O1 <sup>vii</sup> —Si2—O1 <sup>i</sup>	99.87 (9)

Symmetry code(s):

- (i)  $x+1/4, z-3/4, y+1/4$ ;
- (ii)  $-z+3/4, y-1/4, -x+1/4$ ;
- (iii)  $y, z-1/2, -x$ ; (iv)  $-x, -y, -z+1$ ;
- (v)  $z-1/2, x, -y+1/2$ ; (vi)  $z-1/2, -x, y$ ;
- (vii)  $x+1/4, -z+3/4, -y+1/4$ ;
- (viii)  $-z+3/4, -y+1/4, x+1/4$ ;
- (ix)  $x, -y, -z+1/2$ ;

(x)  $-z+1/2, x, -y$ ; (xi)  $-y, -z+1/2, x$ ; (xii)  $-x+1/2, -y, z-1/2$ .

### 5.1.3.3 Mössbauer spectroscopy and nuclear forward scattering

Skiagite-rich garnet crystals, identified using single-crystal X-ray diffraction, were loaded into a DAC and studied at ambient pressure. We collected SMS spectra from several crystals and fit them to doublets with conventional constraints (equal doublet component widths and areas). All spectra gave hyperfine parameters that were the same within experimental uncertainty except for relative intensities of the different doublets. This difference likely arises from varying ratios of different iron isotopes due to the starting mixture containing unenriched  $\text{Fe}_{1-x}\text{O}$  and  $^{57}\text{Fe}$ -enriched  $\text{Fe}_2\text{O}_3$ , where partial isotopic differentiation occurred during the chemical reaction.

A typical SMS spectrum of skiagite-rich garnet contains two doublets Figure 5.1.3-2 that according to literature data (Amthauer et al. 1976; Woodland and Ross 1994) can be assigned to  $\text{Fe}^{2+}$  on the dodecahedral site and  $\text{Fe}^{3+}$  on the octahedral site. Some of the crystals showed an additional doublet consistent with  $\text{Fe}^{2+}$  on the octahedral site, although with low intensity likely due to the isotopic effect mentioned above. The NFS spectrum collected at ambient conditions Figure 5.1.3-3 is consistent with the SMS spectrum and the fit gave similar hyperfine parameters Table 5.1.3-5. Since the absolute CS value cannot be determined from the NFS data, it was fixed to the value determined from the SMS spectrum.

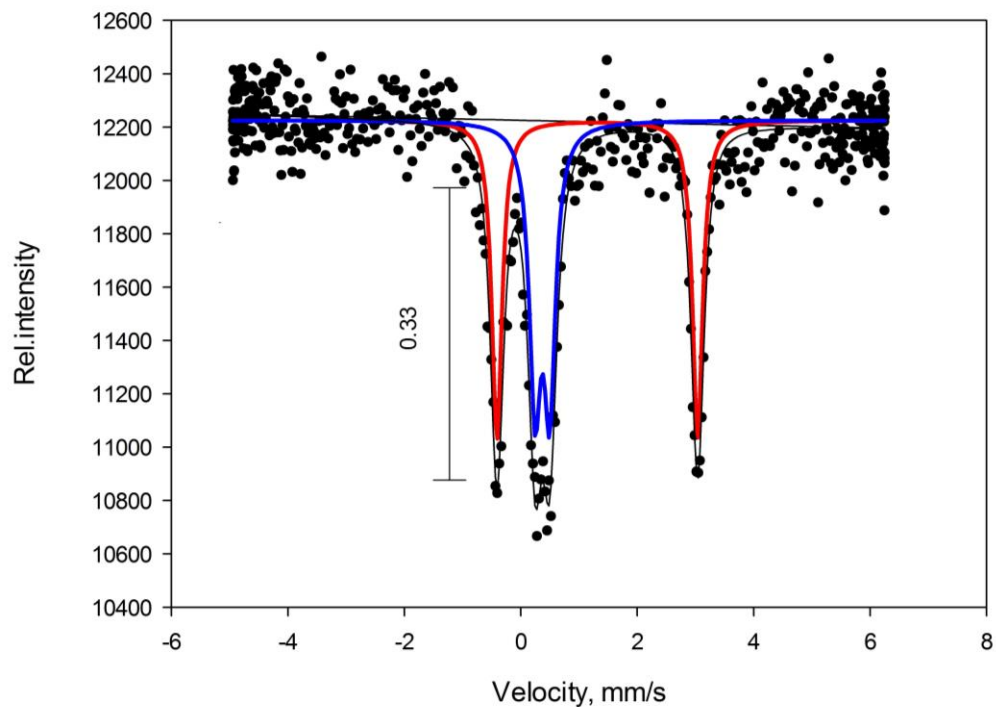


**Figure 5.1.3-2**  $^{57}\text{Fe}$  SMS spectrum of skiaegite-rich garnet at ambient conditions. The solid line shows the fit with parameters given in Table 5. Red and blue doublets represent  $\text{Fe}^{2+}$  and  $\text{Fe}^{3+}$ , respectively.

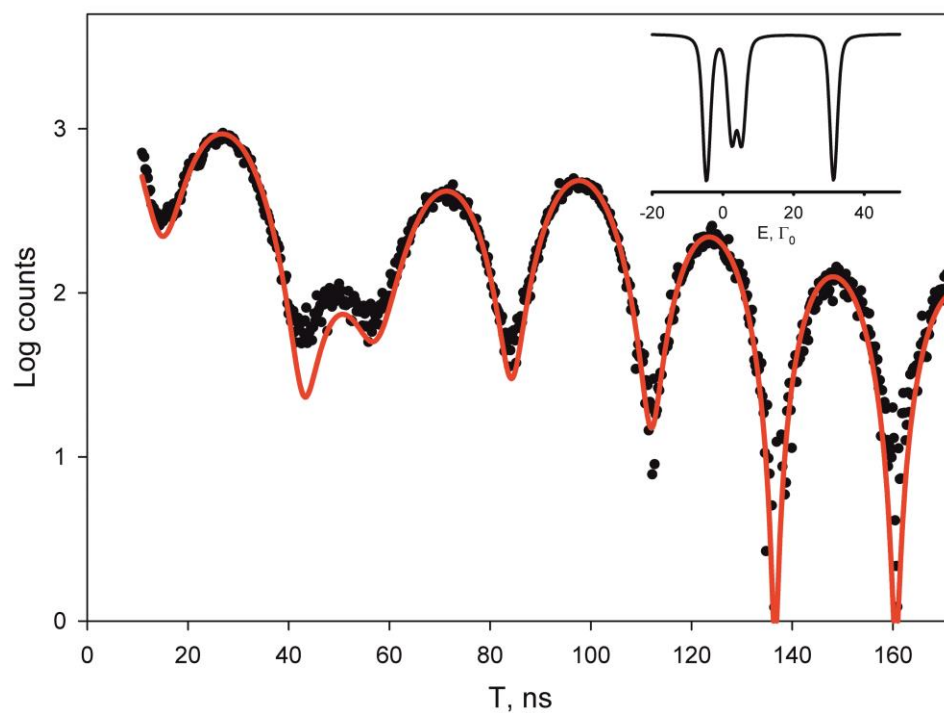


**Figure 5.1.3-3 NFS spectrum of skiagite-rich garnet at ambient conditions. The solid line shows the fit with parameters given in Table 5. The inset shows the energy domain spectrum represented by the time domain data.**

**Table 5.1.3-5 Hyperfine parameters of skiagite-rich garnet at ambient conditions.**

Oxidation state	Position	Center shift (CS)* [mm/s]	Quadrupole splitting (QS) [mm/s]	FWHM [mm/s]
SMS spectroscopy				
Fe <sup>2+</sup>	Dodecahedral	1.31(1)	3.45(2)	0.15(3)
Fe <sup>3+</sup>	Octahedral	0.37(1)	0.26(2)	0.19(4)
NFS spectroscopy				
Fe <sup>2+</sup>	Dodecahedral	1.31**	3.49(5)	
Fe <sup>3+</sup>	Octahedral	0.40(5)	0.27(1)	

**5.1.3.4 XANES**

XANES spectra were simulated using *ab initio* multiple scattering calculations with the FEFF9 code (Rehr et al. 2009). The atomic clusters for Fe1 and Fe2 positions were calculated from the structural model obtained in the single-crystal X-ray diffraction study. Full multiple scattering calculations were performed in a 6 Å radius cluster, while self-consistent potentials were calculated for a 4 Å radius cluster. The Hedin-Lundqvist self-energy exchange correlation was used and multipole (dipole + quadrupole) transitions were calculated to simulate the pre-edge transition peak.

Figure 5.1.3-4 shows the experimental XANES spectra of skiagite-rich garnet and simulated XANES spectra for the adopted structural model. Energies of simulated spectra were shifted so as to fit each simulated curve to the corresponding observed spectra.

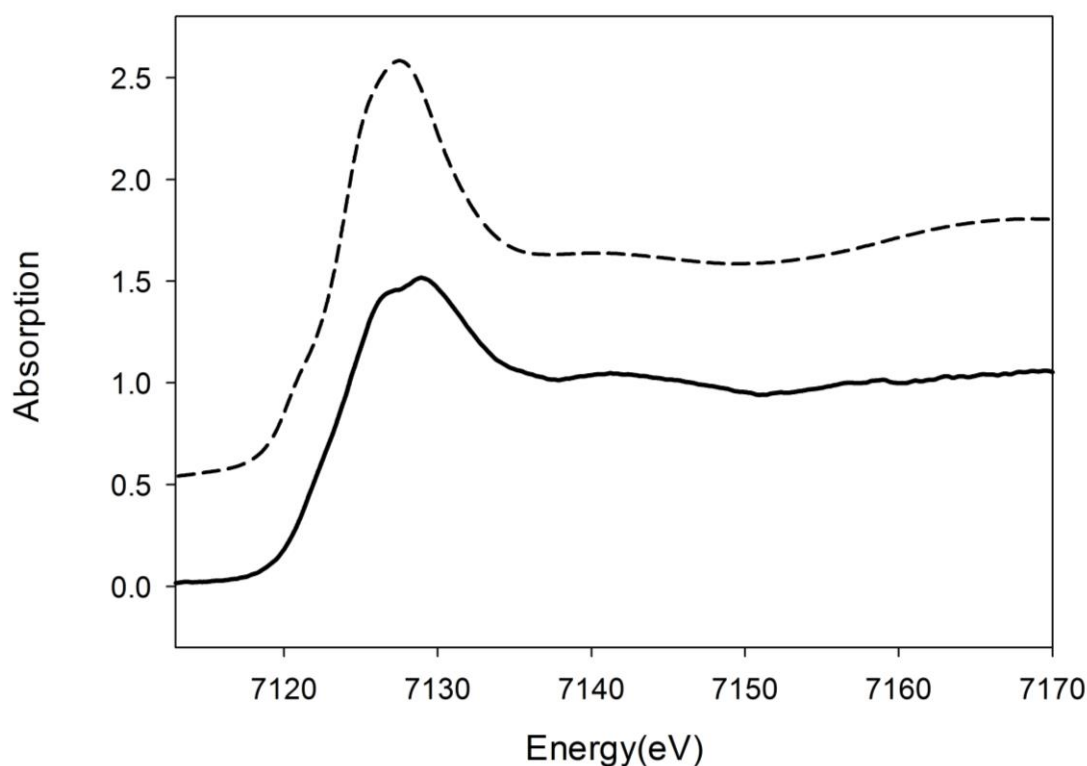


**Figure 5.1.3-4 Normalised Fe K-edge XANES spectra (solid line – experimental and dashed line – simulated) of skiagite-rich garnet at ambient conditions.**

Each spectrum is characterized by two parts: a pre-edge region (~7113 eV) and a main-edge region (7120-7150 eV). Because skiagite-rich garnet is cubic, there is no linear polarization effect and spectra are the same for any crystal orientation. Our experimental setup at the beamline did not allow the collection of spectra with sufficient quality in the pre-edge region. However, comparison of the main-edge regions suggests that the simulated spectra are representative of the experimental ones.

#### **5.1.3.5 Comparison of the crystal structures of Fe-bearing garnet end-members**

The most abundant end-members of Fe-bearing garnets are almandine,  $\text{Fe}^{2+}_3\text{Al}_2\text{Si}_3\text{O}_{12}$ , and andradite,  $\text{Ca}_3\text{Fe}^{3+}_2(\text{SiO}_4)_3$ , which are stable at ambient pressure. Knorringite,  $\text{Fe}_3\text{Cr}_2\text{Si}_3\text{O}_{12}$ , is stable above 6 GPa (Fursenko 1981). Majorite,  $\text{Mg}_3(\text{Fe}^{2+}\text{Si})(\text{SiO}_4)_3$ , is considered to be an abundant garnet component at depths >350 km (Ringwood 1975). All of the end-members form solid solutions with skiagite Figure 5.1.3-5.

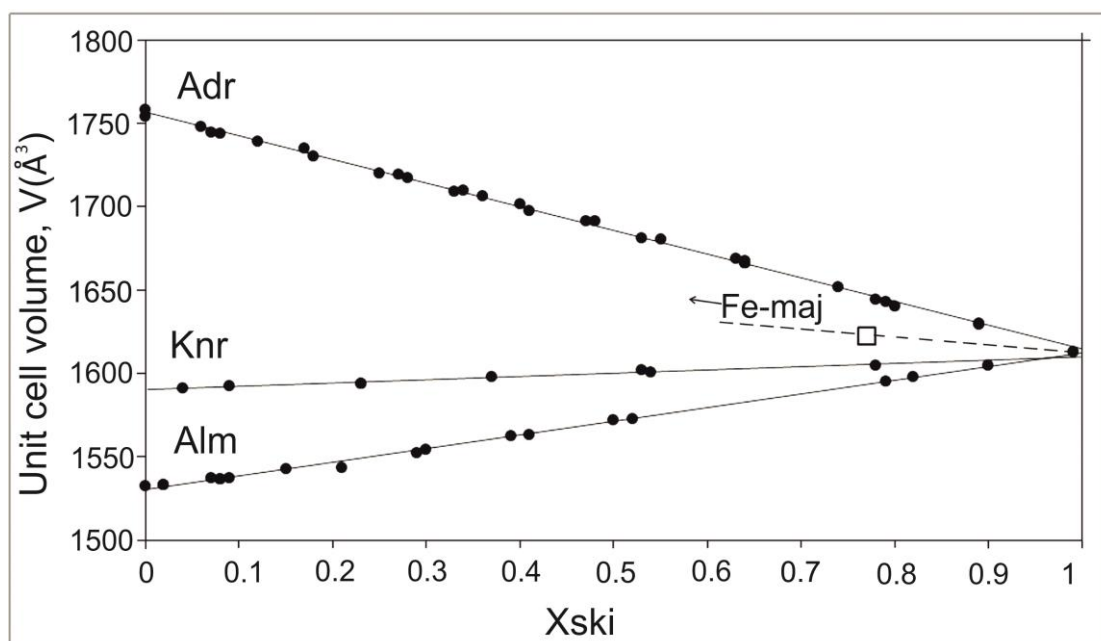


**Figure 5.1.3-5 Unit cell volume,  $V$ , plotted as a function of the skiagite content in andradite-skiagite, almandine-skiagite, and knorringite-skiagite solid solutions. Data for almandine-skiagite and andradite-skiagite are from Woodland and Ross (1994), and for knorringite-skiagite from Woodland et al. (2009). The open square indicates the skiagite-majorite solid solution from this study. Uncertainties are less than the size of the symbols.**

Woodland and Ross (1994) carried out a single-crystal X-ray diffraction study of two almandine-skiagite and five andradite-skiagite crystals in order to investigate variations in bond length with increasing skiagite content. In andradite-skiagite solid solutions  $\text{Fe}^{2+}$  substitutes for the larger  $\text{Ca}^{2+}$  on the dodecahedral sites, so that an increase of the skiagite-component leads to shortening of average  $((\text{Fe}^{2+}, \text{Ca}) - \text{O})_1$  and  $((\text{Fe}^{2+}, \text{Ca}) - \text{O})_2$  bond lengths. Since six of the twelve octahedral edges are shared with neighboring dodecahedra, the octahedral Fe-O bond lengths also shorten. In almandine-skiagite solid solutions an increase of the skiagite-component means that  $\text{Al}^{3+}$  is substituted by larger  $\text{Fe}^{3+}$  cations on octahedral sites that results in an increase of the cation-oxygen octahedral  $(\text{Fe}^{3+}, \text{Al}) - \text{O}$  bond lengths, whereas the lengths of the two non-equivalent dodecahedral bonds  $(\text{Fe} - \text{O})_1$  and  $(\text{Fe} - \text{O})_2$  remain almost constant Figure 5.1.3-6.

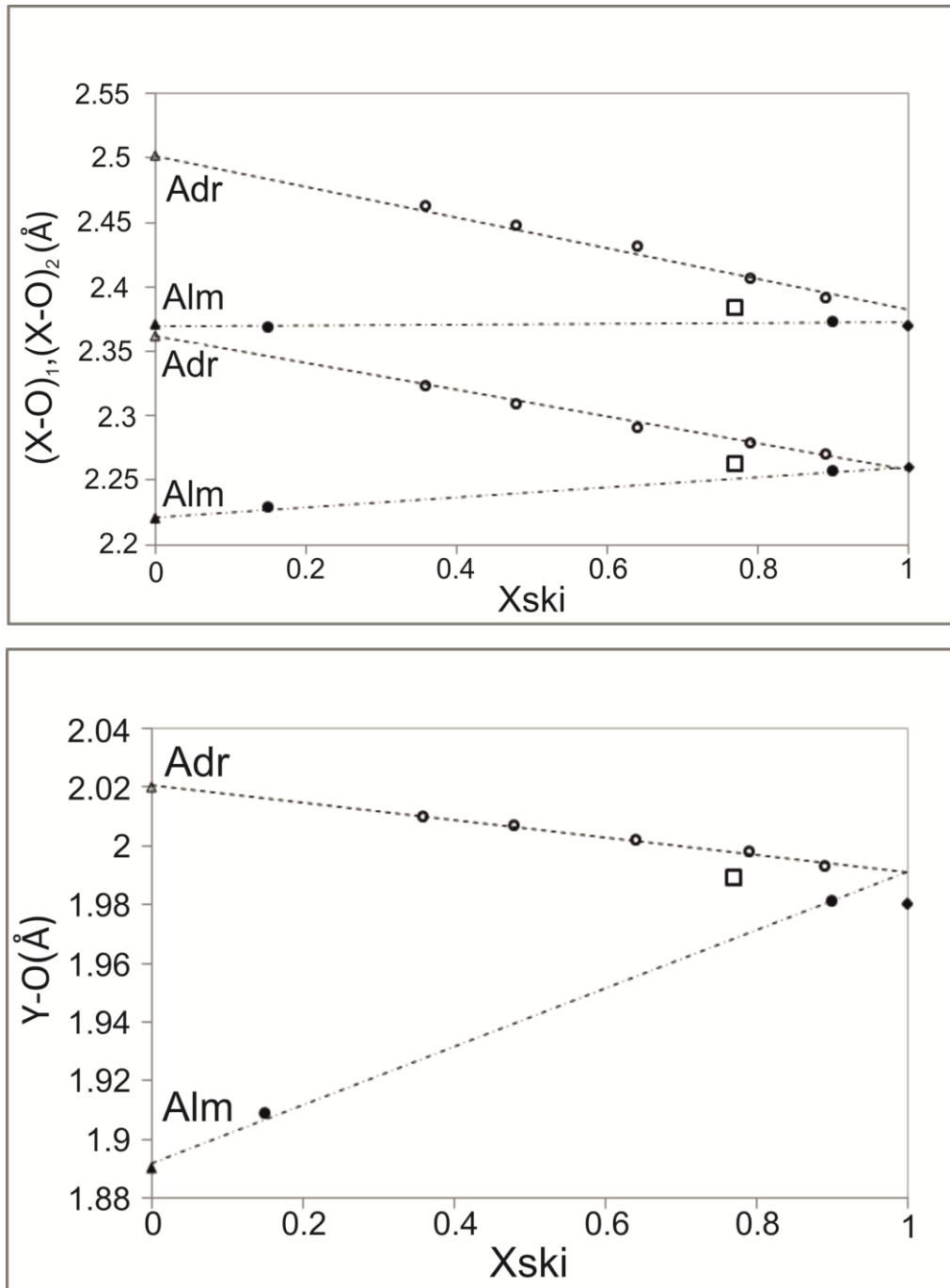


**Figure 5.1.3-6** Variation of the X-O and Y-O bonds lengths with the proportion of skiagite-component in andradite-skiagite and almandine-skiagite solid solutions (X and Y indicate cations in dodecahedral (X) and octahedral (Y) sites) after Woodland and Ross (1994). Data for the andradite (solid triangles) and almandine (open triangles) endmembers are from Armbruster et al. (1992) and Armbruster

**and Geiger (1993). Open squares indicate the skiagite-majorite garnet from this study.**

The tetrahedral (Si-O) bond lengths remain constant across all joins and undergo only minor changes of  $\sim 0.005$  Å in almandine-skiagite garnets and  $\sim 0.01$  Å in andradite-skiagite garnets. The change in Si-O bond lengths along the andradite-skiagite join is likely a response to the large decrease in the volume of neighboring dodecahedra, which leads to a slight distortion of tetrahedra.

### 5.1.3.6 Majoritic component in synthetic garnets

Iron majorite (Fe-maj,  $\text{Fe}_4\text{Si}_4\text{O}_{12}$ ) is the hypothetical endmember of iron-bearing high-pressure garnets. As demonstrated by Akaogi and Akimoto 1977, the solubility of iron majorite in almandine reaches a maximum of 40 mol % between 9.0 and 10.0 GPa at 1000°C. They estimated a unit-cell parameter of 11.595 Å ( $V = 1558.89$  Å<sup>3</sup>) for the  $\text{Fe}^{2+}_4\text{Si}_4\text{O}_{12}$  end-member by extrapolation.

The solubility of the iron majorite component in skiagite has not been previously demonstrated. Woodland and O'Neill (1993) showed that no significant excess of silicon ( $>3$  cations pfu) was detected in garnet synthesized at 10 GPa and 1100°C from a starting material with 60% skiagite and 40% majorite. This was confirmed by the observed cell parameter that did not deviate from that of pure skiagite ( $a = 11.7286$  Å) (Woodland and O'Neill 1993).

The structural formula obtained from EMPA and single-crystal X-ray diffraction data shows that the skiagite-rich garnet synthesized in our experiment contains excess Si and  $\text{Fe}^{2+}$  entering the Y site. The cell parameter of this garnet is higher ( $a = 11.7511$  (2) Å) compared to the one ( $a = 11.7286$  Å) reported by Woodland and O'Neil (1993) for pure skiagite. This can be explained by incorporation of the iron majorite component (23 mol %  $\text{Fe}_4\text{Si}_4\text{O}_{12}$ ) into skiagite due to the reaction  $\text{Fe}^{2+}_3\text{Fe}^{3+}_2\text{Si}_3\text{O}_{12} = 2\text{Fe}^{2+}\text{SiO}_3 + \text{Fe}^{2+}\text{Fe}^{3+}_2\text{O}_4 + \text{SiO}_2$ . Additionally, our structural data provide evidence for increase of the unit cell parameter from skiagite to iron majorite (dashed line in Figure 5.1.3-6). If the data are linearly extrapolated (Figure 5.1.3-6), the unit cell parameter of iron majorite in our study is found to be  $a = 11.833$  Å, which is higher than the value

obtained by Akaogi and Akimoto (1977) ( $a = 11.595 \text{ \AA}$ ) through extrapolation of iron majorite – almandine solubility data.

### 5.1.4 Implications

The results of our study provide information on the solubility of the iron-majorite end-member in skiagite. We have demonstrated the possibility to synthesize high quality single crystals of majorite-skiagite garnet and through single-crystal X-ray diffraction data revealed that at least 23 mol % of iron-majorite can be dissolved in skiagite at high pressure and high temperature conditions. The studied garnet contains octahedral Si, which can be an important pressure indicator for garnets in mantle assemblages (Akaogi and Akimoto 1977). The relationship between skiagite and majorite provides evidence for similarity in their crystal chemical behavior, but, at the same time, suggests a consequent reaction on pressure increase. Although both are high-pressure components of garnet, the proportion of iron majorite component relative to skiagite should decrease with increasing pressure. Our data motivates a detailed investigation of structural changes in the skiagite–majorite series as a function of pressure and temperature.

### Acknowledgments

This study was partly supported by the Russian Foundation for Basic Research (project no. 15-05-08261 to Leyla Ismailova and Andrey Bobrov). We acknowledge the European Radiation Facility for provision of synchrotron radiation facilities (BM01 SNBL, ID18, ID24). We would like to thank U. Trenz and D. Krauß for support during the SEM and microprobe measurements.

## 5.2 Effect of composition on compressibility of skiagite-Fe-majorite garnet

Leyla Ismailova<sup>1,2</sup>, Maxim Bykov<sup>1</sup>, Elena Bykova<sup>1</sup>, Andrey Bobrov<sup>3</sup>, Ilya Kuppenko<sup>4</sup>, Valerio Cerantola<sup>1,4</sup>, Denis Vasiukov<sup>1,2</sup>, Natalia Dubrovinskaia<sup>2</sup>, Catherine McCammon<sup>1</sup>, Michael Hanfland<sup>4</sup>, Konstantin Glazyrin<sup>5</sup>, Hanns-Peter Lierman<sup>5</sup>, Alexander Chumakov<sup>4</sup>, Leonid Dubrovinsky<sup>1</sup>

<sup>1</sup>Bayerisches Geoinstitut, University of Bayreuth, Universitätsstraße 30, D-95440 Bayreuth, Germany.

<sup>2</sup>Laboratory of Crystallography, University of Bayreuth, Universitätsstraße 30, D-95440 Bayreuth, Germany.

<sup>3</sup>Department of Petrology, Geological Faculty, Moscow State University, 119234 Moscow, Russia

<sup>4</sup>European Synchrotron Radiation Facility, BP 220, Grenoble F-38043, France.

<sup>5</sup>Photon Sciences, Deutsches Elektronen-Synchrotron, Notkestrasse 85, D-22603 Hamburg, Germany.

*American Mineralogist, in press*

### Abstract

Skiagite-Fe-majorite garnets were synthesized using a multianvil apparatus at 7.5-9.5 GPa and 1400-1600 K. Single-crystal X-ray diffraction at ambient conditions revealed that synthesized garnets contain 23 to 76 % of an Fe-majorite component. We found that the substitution of Fe<sup>2+</sup> and Si<sup>4+</sup> for Fe<sup>3+</sup> in the octahedral site decreases the unit-cell volume of garnet at ambient conditions. Analysis of single-crystal X-ray diffraction data collected on compression up to 90 GPa of garnets with different compositions reveals that with increasing majorite component the bulk modulus increases from 164(3) to 169(3) GPa. Our results and literature data unambiguously demonstrate that the total iron content and the Fe<sup>3+</sup>/Fe<sup>2+</sup> ratio in (Mg,Fe)-majorites have a large influence on their elasticity. At pressures between 50 and 60 GPa we observed a significant deviation from a monotonic dependence of the molar volumes of skiagite-Fe-majorite garnet with pressure, and over a small pressure interval the volume dropped by about 3%. By combining results from single-crystal X-ray diffraction and high-pressure

synchrotron Mössbauer source spectroscopy we demonstrate that these changes in the compressional behavior are associated with changes of the electronic state of Fe in the octahedral site.

### 5.2.1 Introduction

Garnets are among the most abundant phases in the upper mantle and transition zone; hence data on their behavior under extreme conditions is important for understanding the composition, structure, and dynamics of the deep Earth's interior. According to the pyrolite composition model, the Earth's upper mantle below 50 km is dominated by four major phases: olivine ((Mg,Fe)<sub>2</sub>SiO<sub>4</sub>), orthopyroxene ((Mg,Fe)SiO<sub>3</sub>), clinopyroxene ((Ca,Mg)Si<sub>2</sub>O<sub>6</sub>), and garnet ((Mg,Fe,Ca)<sub>3</sub>(Al,Fe<sup>3+</sup>,Cr)<sub>2</sub>Si<sub>3</sub>O<sub>12</sub>) (Ringwood 1975; Ita and Stixrude 1992). With increasing pressure, upper mantle minerals undergo several important phase transitions. Olivine transforms to wadsleyite at a pressure of ~13.5 GPa, and then to ringwoodite at ~18 GPa (Irifune et al. 2008). Ortho- and clinopyroxene progressively dissolve in garnet, resulting in an excess of Mg and Si in the structure (Wood, 2000). The volume fraction of garnet thereby increases from ~10 % to ~40% or more in the transition zone, where garnet(s) become majoritic (Si-rich) (Duffy and Anderson 1989; Irifune et al. 2008; Wood et al. 2013).

Natural garnets are usually complex solid solutions because the garnet structure can accommodate a number of different divalent and trivalent cations. High-pressure garnet endmembers include Mg-majorite Mg<sub>4</sub>Si<sub>4</sub>O<sub>12</sub>, Fe<sup>2+</sup>-majorite Fe<sup>2+</sup><sub>4</sub>Si<sub>4</sub>O<sub>12</sub>, Na-majorite Na<sub>2</sub>MgSi<sub>5</sub>O<sub>12</sub> (Bobrov et al. 2008) and knorringite Mg<sub>3</sub>Cr<sub>2</sub>Si<sub>3</sub>O<sub>12</sub> (Bykova et al., 2013; Dymshits et al., 2014). While most cations in garnet occur in a single oxidation state (Al<sup>3+</sup>, Ca<sup>2+</sup>, Mg<sup>2+</sup>, Cr<sup>3+</sup>), iron commonly occurs as both Fe<sup>2+</sup> and Fe<sup>3+</sup>. The major Fe<sup>3+</sup>-bearing garnets are andradite (Ca<sub>3</sub>Fe<sub>2</sub>Si<sub>3</sub>O<sub>12</sub>), khoharite (Mg<sub>3</sub>Fe<sub>2</sub>Si<sub>3</sub>O<sub>12</sub>), and skiagite (Fe<sub>3</sub>Fe<sub>2</sub>Si<sub>3</sub>O<sub>12</sub>) (Amthauer et al., 1976; Luth et al., 1990; Woodland and Ross, 1994; Ismailova et al., 2015).

Skiagite garnet is important for the description of phase equilibria in mantle rocks. At a fixed oxygen fugacity relative to a standard buffer such as fayalite-magnetite-quartz (FMQ), garnet will be increasingly enriched in Fe<sup>3+</sup> with increasing

pressure (Wood et al. 1996). Similarly, with increasing depth, garnet with fixed  $\text{Fe}^{3+}$  content will be stabilized at progressively lower oxygen fugacities relative to the FMQ buffer.  $\text{Fe}^{3+}/\sum\text{Fe}$  may also increase due to the redistribution of  $\text{Fe}^{3+}$  from clinopyroxene to garnet (Woodland and Koch 2003) due to the expanding skiaigite stability field. At greater depths, skiaigitic garnet accommodates an excess of Si that stabilizes a solid solution with  $\text{Fe}^{2+}$ -majorite ( $\text{Fe}_4\text{Si}_4\text{O}_{12}$ ) (Woodland et al., 2009; Ismailova et al., 2015).

Mössbauer spectroscopy studies on garnet indicate that  $\text{Fe}^{3+}$  occupies an octahedral site (e.g., Amthauer et al., 1976). Thus, it is important to study the effect(s) of the majoritic substitution ( $2\text{Fe}^{3+} \leftrightarrow \text{Fe}^{2+} + \text{Si}^{4+}$ ) in the octahedral position. There is additional interest in studies of iron in garnets at high pressure due to the possibility of compression-induced spin-crossover (Friedrich et al. 2014, 2015; Stan et al. 2015).

In this paper we report results of a study of synthetic pure-iron skiaigite-majorite garnet with different compositions using single crystal X-ray diffraction and synchrotron Mössbauer source spectroscopy up to 90 GPa. We combine our data with those reported earlier for different garnets in order to evaluate the effect of majoritic substitution on material properties.

## 5.2.2 Methods

Iron-bearing skiaigite-majorite garnets with different compositions were synthesized from stoichiometric mixtures of pure oxides:  $\text{SiO}_2$ ,  $\text{Fe}_2\text{O}_3$ , and  $\text{Fe}_{1-x}\text{O}$ . High temperatures and high pressures were generated using a Kawai-type multi-anvil apparatus at Bayerisches Geoinstitut (Bayreuth, Germany) (Frost et al. 2004). Experimental conditions and compositions are listed in Table 5.2.3-1 More details of the synthesis experiments can be found in Ismailova et al., (2015).

Crystals for single-crystal X-ray diffraction studies were selected based on the quality of their diffraction peak profiles using an *in-house* high-brilliance rotating anode diffractometer (Dubrovinsky et al. 2006). Pre-selected isometric crystals of  $\sim 10$   $\mu\text{m}$  in the longest dimension were loaded in diamond anvil cells (DACs) into holes drilled through Re gaskets indented to 20-35  $\mu\text{m}$  thickness. First, the single-crystal data

were collected at ambient conditions. After that DACs were loaded with Ne at ~1.4 kbar. Neon serves as a quasi-hydrostatic pressure transmitting medium. Below 10 GPa the pressure was determined from ruby fluorescence, while above 10 GPa we used the diffraction lines of crystallized Ne to determine the pressure (<http://kantors50webs.com>). We used Boehler-Almax diamond anvils with 250  $\mu\text{m}$  culets for measurements up to ~60 GPa, and beveled diamonds with 120  $\mu\text{m}$  culets were used to achieve pressures up to 90 GPa.

Single-crystal X-ray diffraction experiments were performed at the beamline ID09A at ESRF, Grenoble, France ( $\lambda = 0.4151 \text{ \AA}$ ) (Merlini and Hanfland, 2013) and at the extreme conditions beamline ECB P02.2 at PETRA III, DESY, Hamburg, Germany ( $\lambda = 0.2903 \text{ \AA}$ ) (Liermann et al. 2015). Diffraction images were collected at various pressures using the following strategy: wide scans were collected during  $\omega$  rotation scans of  $\pm 20^\circ$  with a  $40^\circ$  step and an exposure time of 2s; step scans were collected with rotation of the cell of  $\pm 38^\circ$  with a step  $0.5^\circ$  and 1s/frame. Diffraction images were first analyzed using Dioptas software (Prescher and Prakapenka 2015). The indexing of Bragg reflections, the intensity data reduction and the empirical absorption correction were performed with the Agilent™ CrysAlisPro software (Oxford Diffraction 2006). Crystal structures were refined using Jana2006 (Petříček et al. 2014). Polyhedral volumes were calculated using VESTA software (Momma and Izumi 2011). The Birch-Murnaghan equations of state coefficients were refined using the program EoSFit-7c (Angel et al. 2014).

Synchrotron Mossbauer Source (SMS) spectra were recorded at the Nuclear Resonance Beamline ID18 at ESRF (Rüffer and Chumakov 1996) using the (111) Bragg reflection of a  $^{57}\text{FeBO}_3$  single crystal mounted on a Wissel velocity transducer driven with a sinusoidal wave form (Potapkin et al. 2012). The X-ray beam was focused to 20  $\mu\text{m}$  vertical and 10  $\mu\text{m}$  horizontal dimensions using Kirkpatrick-Baez mirrors. The linewidth of the SMS and the absolute position of the center shift (CS) were controlled before and after each measurement using a  $\text{K}_2\text{Mg}^{57}\text{Fe}(\text{CN})_6$  reference single line absorber. The velocity scale was calibrated using a 25  $\mu\text{m}$  thick natural  $\alpha$ -Fe foil. Each spectrum took ~ 1-2 hours to collect. Spectra were fitted using a full transmission

integral with a normalized Lorentzian-squared source line shape using the MossA software package (Prescher et al. 2012).

## 5.2.3 Results

### 5.2.3.1 Structures of skiagite-Fe-majorite garnets at ambient conditions

Single crystals of garnets were measured first at ambient conditions. Synthesis conditions, compositions, unit-cell volumes, and crystallographic data of skiagite-majorite garnets collected at ambient conditions are given in Table 5.2.3-1. All garnets have structures with a cubic space group  $Ia\bar{3}d$  (#230) symmetry. The structural refinement revealed that the dodecahedral and tetrahedral sites are fully occupied by Fe and Si atoms, respectively. The octahedral site is also fully filled, but has a mixed (Fe and Si) occupancy.

**Table 5.2.3-1 Results of the crystal structure refinement based on single-crystal X-ray diffraction data for skiagite-majorite garnets with four different compositions.**

Run number and composition	S6073 Ski <sub>76.6</sub> Maj <sub>23.4</sub>	S6176 Ski <sub>69</sub> Maj <sub>31</sub>	S6177 Ski <sub>54</sub> Maj <sub>46</sub>	S6160 Ski <sub>24</sub> Maj <sub>76</sub>
P, T conditions of XRD experiment	9.5 GPa 1400 K	9.5 GPa 1600 K	9.5 GPa 1500 K	7.5 GPa 1400 K
Crystal system	cubic			
Space group	Ia $\bar{3}$ d			
Z	8			
$\lambda$ (Å)	0.4151			
$a$ (Å)	11.7210(2)	11.71620(10)	11.7053(4)	11.68130(10)
$V$ (Å <sup>3</sup> )	1610.25(5)	1608.28(2)	1603.79(9)	1593.95(2)
$F(000)$	2117	2114	2100	2068
Theta range for data collection (°)	2.658/17.585	1.742/17.821	1.748/17.795	2.49/22.03
Index ranges	-15 < $h$ < 12,	-15 < $h$ < 17,	-17 < $h$ < 14,	-20 < $h$ < 21,
	-18 < $k$ < 17,	-20 < $k$ < 19,	-15 < $k$ < 13,	-16 < $k$ < 13,
	-17 < $l$ < 13	-15 < $l$ < 13	-20 < $l$ < 19	-15 < $l$ < 16
No. of measured, independent, and observed [ $I > 3s(I)$ ] reflections	1626/269/219	1765/281/221	1655/267/181	1955/296/182

$R_{\text{int}}$	0.0337	0.0316	0.0752	0.0415
No.of parameters/restraints/ constraints	18/0/2	18/0/2	18/0/2	18/0/2
Final $R$ indices [ $I > 3\sigma(I)$ ] $R_1 / wR_2$	0.0326/0.0417	0.0300/0.0470	0.0653/0.0821	0.0868/0.1020
$R$ indices (all data) $R_1 / wR_2$	0.0394/0.0443	0.0381/0.0497	0.0781/0.0852	0.1491/0.1630

The earlier data we reported on the volume of skiagite-majorite garnet (Ismailova et al.,2015) larger than the value in the current study. Such difference we may attribute to the different synchrotron set up, measurement techniques, choice of a standard, and based on systematic measurements consider data in this study to be more reliable.

Structural refinement also revealed that the synthesized garnets contain from 23.4(1) mol. % to 76(5) mol. % of the end member iron-majorite ( $\text{Fe}_4\text{Si}_4\text{O}_{12}$ ). An increase in Fe-majorite content causes a decrease in the molar volume of the garnet (Figure 5.2.3-1). If we linearly extrapolate our data along the iron majorite-skiagite join, we obtain a unit cell volume for pure majorite  $\text{Fe}_4\text{Si}_4\text{O}_{12}$  of  $1589.2 \text{ \AA}^3$ , which is higher than the value obtained by Akaogi and Akimoto (1977) ( $1558.89 \text{ \AA}^3$ ) from extrapolation of iron majorite ( $\text{Fe}_4\text{Si}_4\text{O}_{12}$ )-almandine ( $\text{Fe}_3\text{Al}_2\text{Si}_3\text{O}_{12}$ ) solubility data.

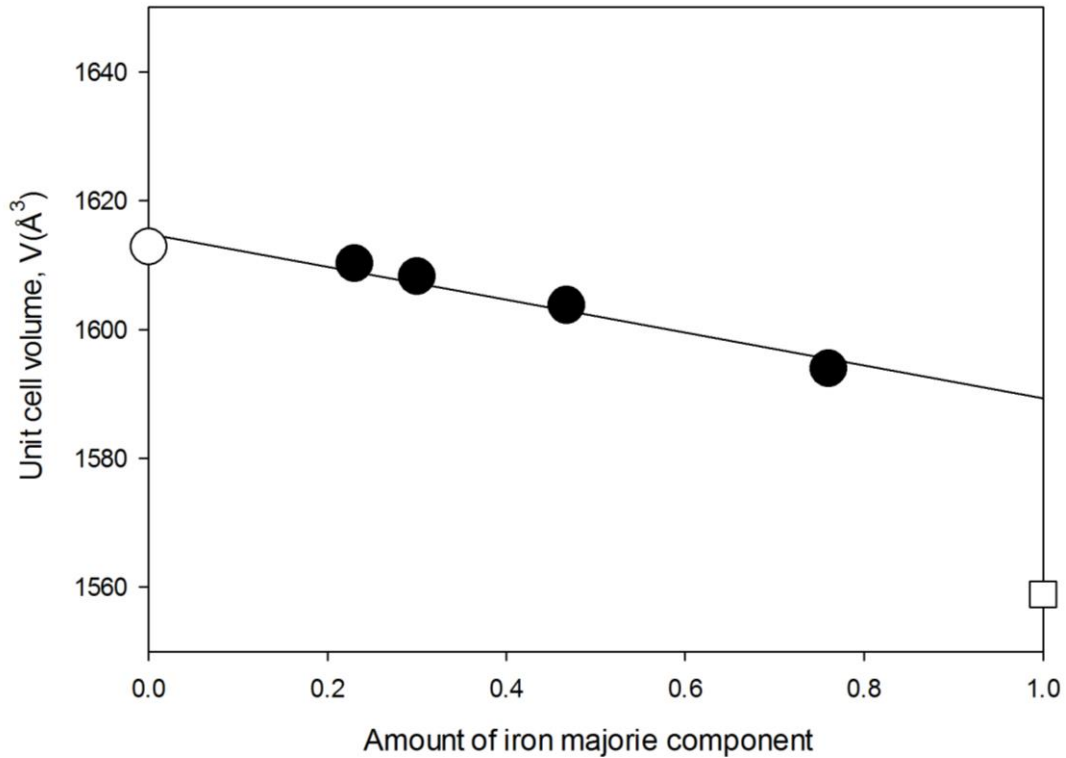


**Figure 5.2.3-1 Unit cell volume across the skiagite-majorite join showing linear behavior as a function of composition. Filled circles- this study, open circle - (Woodland and Ross 1994), open square – pure iron majorite as obtained by extrapolation of solid solution data along the almandine-majorite join (Akaogi and Akimoto 1977). Errors are less than the symbol size.**

The crystal structure refinement shows that a change in the unit-cell volume is associated with a decrease in the (Fe,Si)-O bond length of (Fe,Si)O<sub>6</sub> octahedra. Variations in the bond length and polyhedral volumes are shown in Table 5.2.3-2 in comparison with the values for pure skiagite predicted by Novak and Gibbs (1971). With increasing iron-majorite component along the skiagite-majorite join from (Ski<sub>100</sub>) to (Ski<sub>24</sub>), the bond length decreases from 1.98 Å to 1.957(5) Å, and the polyhedral volume reduces from 10.40 Å<sup>3</sup> (Ski<sub>100</sub>) to 9.9780 Å<sup>3</sup> (Ski<sub>24</sub>). Remarkably, garnet maintains cubic symmetry up to 76% of iron-majorite content. In pyrope-majorite garnets a transition from cubic to tetragonal symmetry occurs at 80 % of Mg<sub>4</sub>Si<sub>4</sub>O<sub>12</sub> (Heinemann et al. 1997); Na-majorite-pyrope remains cubic with up to 70% of Na-

majorite component, and knorringite-majorite garnet - with up to 97% of Mg-majorite (Dymshits et al. 2013).

**Table 5.2.3-2 Bond lengths and volumes of octahedra in skiagite-majorite garnets.**

Composition	Ski <sub>100</sub> *	Ski <sub>76.6</sub> Maj <sub>23.4</sub>	Ski <sub>69</sub> Maj <sub>31</sub>	Ski <sub>54</sub> Maj <sub>46</sub>	Ski <sub>24</sub> Maj <sub>76</sub>
(Fe,Si)-O, Å	1.98	1.9818(13)	1.969(4)	1.9771(15)	1.957(5)
(Fe,Si)O <sub>6</sub> , Å <sup>3</sup>	10.40	10.3646	10.2914	10.1732	9.9780

\*predicted by Novak and Gibbs (1971)

### 5.2.3.2 Equation of state of skiagite-majorite garnets at pressures up to 50 GPa

For measurements at high pressure we used garnet single crystals with four different compositions along skiagite-majorite join:

- **Ski<sub>76.6</sub>Maj<sub>23.4</sub>** Fe<sup>2+</sup><sub>3</sub>(Fe<sup>2+</sup><sub>0.234(2)</sub>Fe<sup>3+</sup><sub>1.532(1)</sub>Si<sup>4+</sup><sub>0.234(2)</sub>)Si<sub>3</sub>O<sub>12</sub>;
- **Ski<sub>69</sub>Maj<sub>31</sub>** Fe<sup>2+</sup><sub>3</sub>(Fe<sup>2+</sup><sub>0.31(2)</sub>Fe<sup>3+</sup><sub>1.39(2)</sub>Si<sup>4+</sup><sub>0.31(2)</sub>)Si<sub>3</sub>O<sub>12</sub>;
- **Ski<sub>54</sub>Maj<sub>46</sub>** Fe<sup>2+</sup><sub>3</sub>(Fe<sup>2+</sup><sub>0.46(2)</sub>Fe<sup>3+</sup><sub>1.08(2)</sub>Si<sup>4+</sup><sub>0.46(2)</sub>)Si<sub>3</sub>O<sub>12</sub>;
- **Ski<sub>24</sub>Maj<sub>76</sub>** Fe<sup>2+</sup><sub>3</sub>(Fe<sup>2+</sup><sub>0.76(5)</sub>Fe<sup>3+</sup><sub>0.48(5)</sub>Si<sup>4+</sup><sub>0.76(5)</sub>)Si<sub>3</sub>O<sub>12</sub>.

The unit cell volume variations with pressure were measured for Ski<sub>76.6</sub>Maj<sub>23.4</sub> up to 89 GPa and for Ski<sub>69</sub>Maj<sub>31</sub>, Ski<sub>54</sub>Maj<sub>46</sub>, and Ski<sub>24</sub>Maj<sub>76</sub> up to 60 GPa (Figure 5.2.3-2, Table S 5.2.6-1-4). All studied garnets in the skiagite-majorite join show similar compressional behavior with unit cell volumes decreasing monotonically with pressure increase up to 50 GPa.

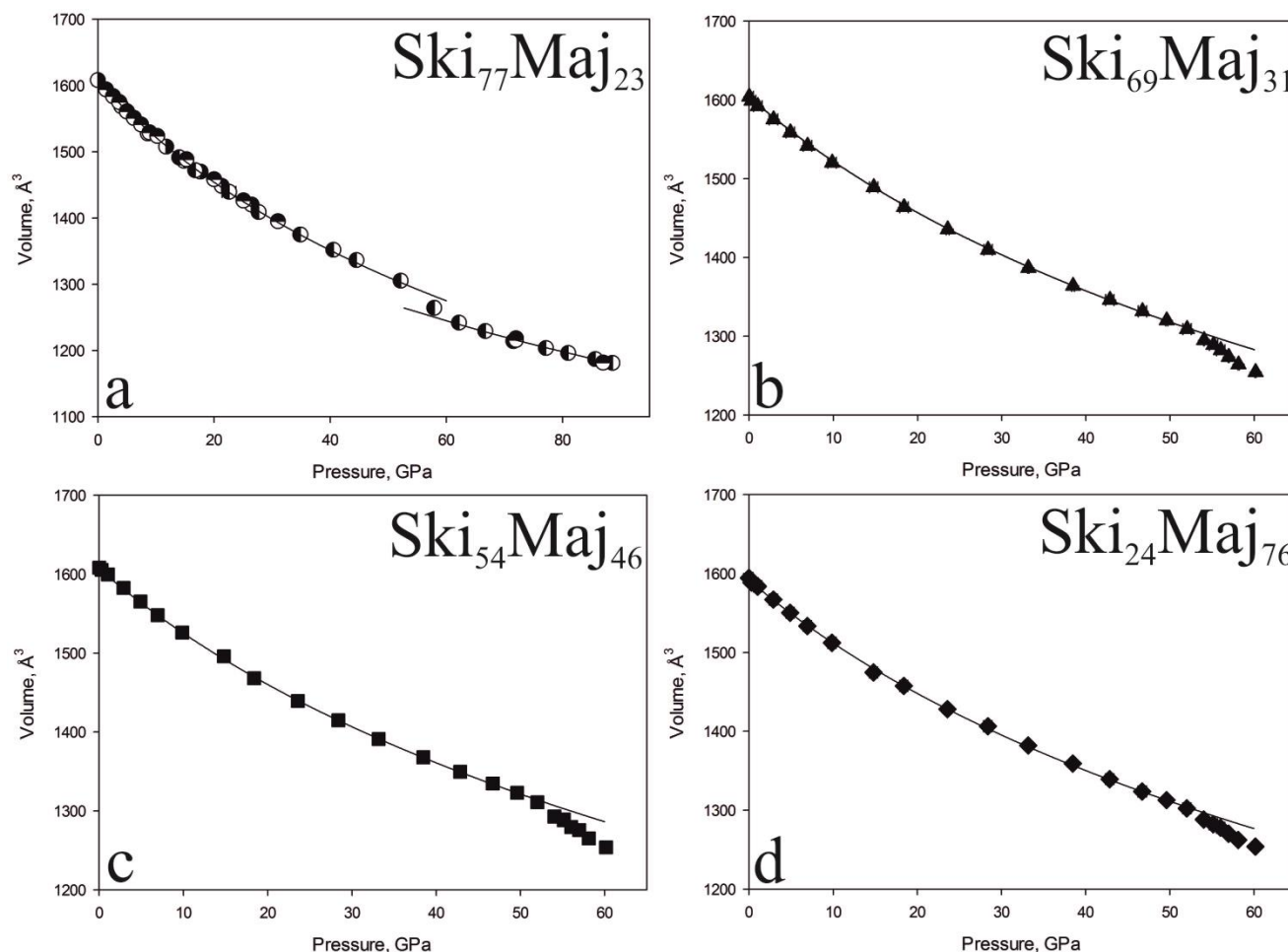


**Figure 5.2.3-2 Compressibility of skiagite-majorite garnet with four different compositions (a –  $\text{Fe}^{2+}_3(\text{Fe}^{2+}_{0.234(2)}\text{Fe}^{3+}_{1.532(1)}\text{Si}^{4+}_{0.234(2)})\text{Si}_3\text{O}_{12}$  ; b –  $\text{Fe}^{2+}_3(\text{Fe}^{2+}_{0.31(2)}\text{Fe}^{3+}_{1.39(2)}\text{Si}^{4+}_{0.31(2)})\text{Si}_3\text{O}_{12}$  ; c –  $\text{Fe}^{2+}_3(\text{Fe}^{2+}_{0.46(2)}\text{Fe}^{3+}_{1.08(2)}\text{Si}^{4+}_{0.46(2)})\text{Si}_3\text{O}_{12}$  ; d –  $\text{Fe}^{2+}_3(\text{Fe}^{2+}_{0.76(5)}\text{Fe}^{3+}_{0.48(5)}\text{Si}^{4+}_{0.76(5)})\text{Si}_3\text{O}_{12}$  . The error bars are comparable to the symbol size. The results of fits using a 3<sup>rd</sup> order Birch-Murnaghan equation of state are shown by solid lines**

A drastic change in the compressional behavior appears at pressures above 50 GPa (Figure 5.2.3-2). The pressure-volume relation obtained for  $\text{Ski}_{76.6}\text{Maj}_{23.4}$  up to 89 GPa can be fit by two curves showing a clear discontinuity in the volume change at pressures between 50 and 60 GPa and a similar tendency is observed for other garnets

(Figure 5.2.3-2). In all cases the volume reduction in the interval of 40 to 50 GPa is about 3.1-3.5 %, while between 50 and 60 GPa it is about 4.7-5.5 %. Despite the clear discontinuity in the compressional behavior, no structural transitions were detected from the structure refinements and skiagite-majorite garnets maintained cubic symmetry even at highest pressures achieved. We refined the garnet compositions at every pressure point and no changes were observed.

We used the pressure-volume (P-V) data up to 50 GPa and a 3<sup>rd</sup> order Birch-Murnaghan equation of state (EOS) to obtain the EOS parameters for the four investigated garnets (Table 5.2.3-3). The ambient pressure bulk moduli  $K_{300,0}$  obtained in our study (164(3)-169(3) GPa) are systematically higher than that of pure skiagite  $\text{Fe}_3\text{Fe}_2\text{Si}_3\text{O}_{12}$  (157(3) GPa,  $K'=6.7(8)$ ) obtained by Woodland et al. (1999). The pressure derivatives of the bulk moduli ( $K'$ ) in our fits are within the range 3.88(15) and 4.6(1).

**Table 5.2.3-3 Equation of state coefficients obtained with a 3<sup>rd</sup> Birch-Murnaghan EOS.**

Composition	$V_0, \text{\AA}^3$	$K_{0,300}, \text{GPa}$	$K'$	References
Ski <sub>100</sub>	1611.8(3)	157(3)	6.7(8))	(Woodland et al. 1999)
Ski <sub>76.6</sub> Maj <sub>23.4</sub>	1607.5(9)	164(3)	3.88(15)	this study
Ski <sub>69</sub> Maj <sub>31</sub>	1608(2)	168(3)	4.2(2)	this study
Ski <sub>54</sub> Maj <sub>46</sub>	1603(2)	163(3)	4.6(1)	this study
Ski <sub>24</sub> Maj <sub>76</sub>	1592.69(94)	169(3)	4.4(3)	this study

### 5.2.3.3 Behavior of coordination polyhedra upon compression.

Accurate crystal structure refinement allows us to calculate the volumes of different polyhedra and follow them as a function of pressure. The skiagite-Fe-majorite solid

solution is characterized by the substitution of  $\text{Fe}^{3+}$  for  $\text{Fe}^{2+}$  and  $\text{Si}^{4+}$  in the octahedral site:  $2\text{Fe}^{3+} \leftrightarrow \text{Fe}^{2+} + \text{Si}^{4+}$ ; the dodecahedral site is occupied exclusively by  $\text{Fe}^{2+}$  and the tetrahedral site is occupied only by  $\text{Si}^{4+}$ . In order to avoid uncertainties introduced by correlations between  $K$  and  $K'$  we fit the data using a 2<sup>nd</sup> order Birch-Murnaghan equation of state ( $K'=4$ ). Results of the P-V fit ( $V_0$  and  $K_{300,0}$ ) for each individual polyhedron for all studied garnets are given in Table S 5.2.6-5 and the pressure dependence of the volumes for tetrahedra, octahedra, and dodecahedra for garnet with composition  $\text{Ski}_{76.6}\text{Maj}_{23.4}$  are shown in Figure 5.2.3-3.

As expected,  $\text{SiO}_4$  tetrahedra are stiff with bulk moduli between 386 and 483 GPa. These values are typical for  $\text{SiO}_4$  tetrahedra in silicate garnets and are in good agreement with data (327 to 434 GPa) reported earlier from both experimental and theoretical studies on silicate garnets (Milman et al. 2001; Friedrich et al. 2014, 2015). The  $\text{Fe}^{2+}\text{O}_8$  polyhedra are much more compressible with bulk moduli of 101-115 GPa. At pressures up to about 50 GPa, the compressibility of  $(\text{Fe,Si})\text{O}_6$  octahedra for all studied garnets are similar and fall in the range 216-233 GPa. At 50 GPa iron-bearing octahedra show a drastic decrease in volume with a reduction of about 7%. In contrast,  $\text{FeO}_8$  and  $\text{SiO}_4$  polyhedra show monotonically varying behavior upon compression up to the highest pressure achieved in this study (Figure 5.2.3-3).

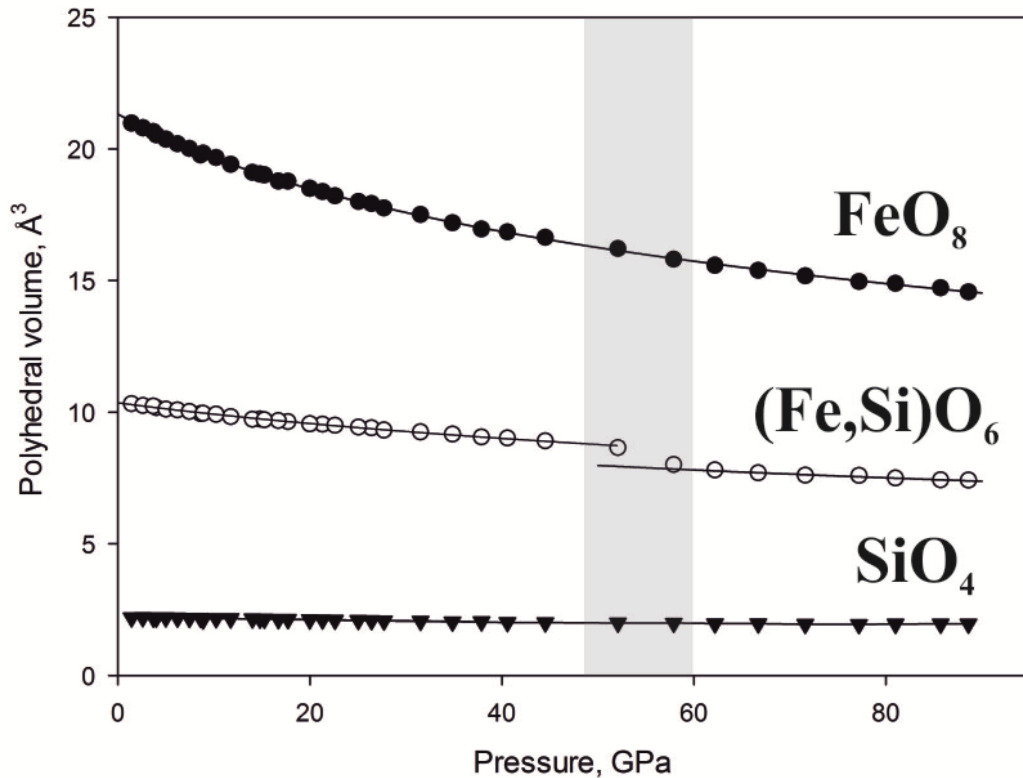


**Figure 5.2.3-3 Polyhedral volume compression of skiagite-majorite garnet  $\text{Ski}_{76.6}\text{Maj}_{23.4}$ . Solid lines represent the fit of the P-V data using a 2<sup>nd</sup> order Birch-Murnaghan equation of state ( $K' = 4$ ). Errors are smaller than the symbol size. The gray bar indicates the pressure region of the iron high-spin to low-spin transition.**

#### 5.2.3.4 Synchrotron Mössbauer source spectroscopy

Synchrotron Mössbauer source spectra of  $\text{Ski}_{76.6}\text{Maj}_{23.4}$  garnet were collected at several pressures between ambient and 90 GPa (selected spectra are shown in Figure 5.2.3-4 and hyperfine parameters are presented in Table 5.2.3-4). Here we present the results directly related to the changes in garnet crystal structure observed above 50 GPa, while detailed spectral analysis and their interpretation will be published elsewhere (Vasuikov et al., in preparation). At pressures below ~50 GPa Mössbauer spectra contain two components – one with higher and one with lower center shift (CS) and quadrupole splitting (QS). The former has hyperfine parameters characteristic for  $\text{Fe}^{2+}$  in a dodecahedral oxygen environment while the latter may be assigned to mixed  $\text{Fe}^{2+}$

and  $\text{Fe}^{3+}$  in octahedra (Figure 5.2.3-4). Up to 50 GPa, there are no any drastic changes in SMS spectra and hyperfine parameters vary monotonically with pressure. Between 50 and 60 GPa there are notable changes in the appearance of the component corresponding to  $\text{Fe}^{3+}$ -dominated octahedra, while the component corresponding to  $\text{Fe}^{2+}$  in  $\text{FeO}_8$  dodecahedra remains almost the same. There are several possibilities to fit spectra above 50 GPa. One is shown in Figure 5.2.3-4(c) with two components corresponding to  $(\text{Fe},\text{Si})\text{O}_6$  octahedra – a doublet with CS even lower than those observed below 50 GPa but with higher QS, and a singlet with relatively high CS. Since CS of  $\text{Fe}^{3+}$  decreases and QS increases at the high spin to low spin crossover (Bengtson et al. 2009; Hsu et al. 2011), the changes observed above 50 GPa are consistent with the low-spin  $\text{Fe}^{3+}$  in the octahedral site in skiaegite-majorite garnet. As seen in the single-crystal XRD data, the octahedral site is filled by  $\text{Fe}^{3+}$ ,  $\text{Fe}^{2+}$ , and  $\text{Si}^{4+}$  in the studied garnets. Thus, a singlet in the SMS spectra with relatively low CS (Figure 5.2.3-4(c)) could be associated with low spin  $\text{Fe}^{2+}$ , analogous to Mössbauer spectroscopic data for  $\text{Fe}^{2+}$  in ferropericlase (Kantor et al. 2006).

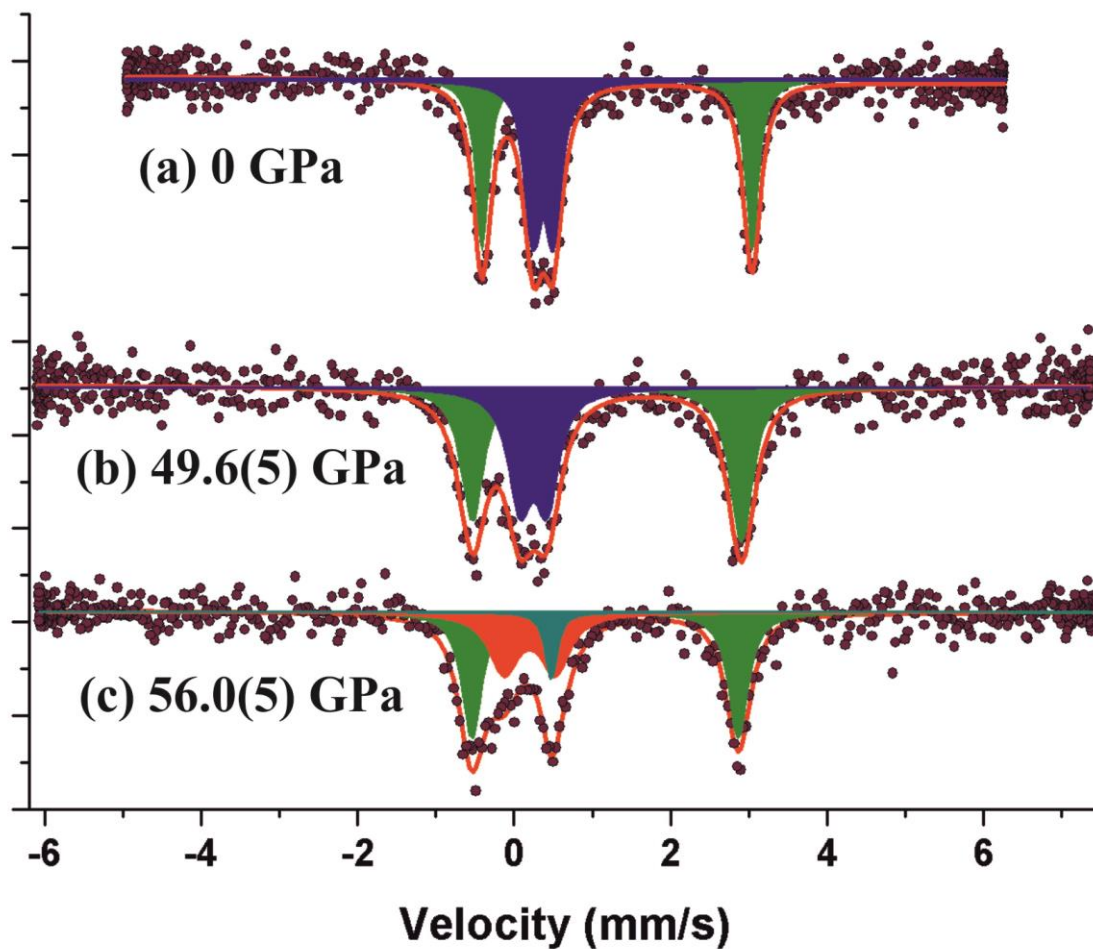


Figure 5.2.3-4 Selected Mössbauer spectra of skiagite-majorite garnet ( $\text{Fe}^{2+}_3(\text{Fe}^{2+}_{0.234(2)}\text{Fe}^{3+}_{1.532(1)}\text{Si}^{4+}_{0.234(2)})\text{Si}_3\text{O}_{12}$ ) at (a) ambient, at (b) 49.6(5) GPa, at 56.0(5) GPa. Hyperfine parameters are shown in Table 5.2.3- 4.

**Table 5.2.3-4 Hyperfine parameter at selected pressures for skiaigite-majorite garnet with composition  $(\text{Fe}^{2+}_3(\text{Fe}^{2+}_{0.234(2)}\text{Fe}^{3+}_{1.532(1)}\text{Si}^{4+}_{0.234(2)})\text{Si}_3\text{O}_{12})$ .**

Oxidation state	Position	Center shift (CS)* [mm/s]	Quadrupole splitting (QS) [mm/s]	Relative area [%]
Ambient				
Fe <sup>2+</sup>	Dodecahedral	1.31(1)	3.45(2)	58(2)
Fe <sup>3+</sup>	Octahedral	0.37(1)	0.26(2)	42(2)
49.6(5) GPa				
Fe <sup>2+</sup>	Dodecahedral	1.17(1)	3.42(2)	58(3)
Fe <sup>3+</sup>	Octahedral	0.23(2)	0.33(3)	42(3)
56.0(5) GPa				
Fe <sup>2+</sup>	Dodecahedral	1.15(1)	3.41(3)	54(8)
Fe <sup>3+</sup>	Octahedral	0.17(2)	0.4(2)	34(9)
Fe <sup>2+</sup>	Octahedral	0.5	-	12(9)

## 5.2.4 Discussion

### 5.2.4.1 Majoritic substitution in garnets

The iron majorite endmember  $\text{Fe}_4\text{Si}_4\text{O}_{12}$  is not stable, but the solid-solution  $\text{Fe}_3\text{Al}_2\text{Si}_3\text{O}_{12}$ – $\text{Fe}_4\text{Si}_4\text{O}_{12}$  has been shown to extend to at least 40 mol. %  $\text{FeSiO}_3$  (Akaogi and Akimoto 1977). There have been several studies in the system  $\text{Mg}_4\text{Si}_4\text{O}_{12}$ – $\text{Fe}_4\text{Si}_4\text{O}_{12}$  majorite focusing on phase stability and crystal structures of garnets (Kato

1986; Matsubara et al. 1990; Ohtani et al. 1991; Tomioka et al. 2002; McCammon and Ross 2003). However, the effect of iron-majorite substitution on the compressibility of garnets is unknown.

Pyrope-majorite garnets have been studied using Brillouin spectroscopy (Sinogeikin and Bass 2002; Gwanmesia et al. 2009). Their results demonstrated that the zero-pressure bulk modulus of  $\text{Py}_{50}\text{-Mj}_{50}$  and  $\text{Py}_{60}\text{Mj}_{40}$  decreases slightly (from 172(2) to 169(1) GPa, essentially within the uncertainty of measurements) with a decrease of the majorite component. Recent work by Dymshits et al. (2014) reports a small increase of the bulk modulus from 153.4(9) GPa to 157(2) GPa in knorringite-majorite garnet ( $\text{Mg}_{3.19}\text{Cr}_{1.60}\text{Si}_{3.19}\text{O}_{12}$ ) with admixture of 19% of a majorite component ( $\text{Mg}_4\text{Si}_4\text{O}_{12}$ ). Hazen et al. (1994) conducted single-crystal X-ray diffraction studies of majorites with different compositions: Ca-bearing majorite ( $\text{Ca}_{0.49}\text{Mg}_{2.51}$ )( $\text{Mg,Si}$ ) $\text{Si}_3\text{O}_{12}$  ( $K=164.8(2.3)$  GPa), Na-bearing majorite ( $\text{Na}_{0.37}\text{Mg}_{2.48}$ )( $\text{Mg}_{0.13}\text{Al}_{1.07}\text{Si}_{0.80}$ ) $\text{Si}_3\text{O}_{12}$  ( $K=175.1(1.3)$  GPa), and ( $\text{Na}_{1.88}\text{Mg}_{1.22}$ )( $\text{Mg}_{0.06}\text{Si}_{1.94}$ ) $\text{Si}_3\text{O}_{12}$  ( $K=191.5(2.5)$  GPa). The isothermal bulk modulus of these garnets increases with increasing majorite component.

Figure 5.2.4-1(a) shows the variation of the bulk moduli of different garnets as a function of majorite content. It is obvious that an increase of the majorite component causes an increase of the bulk modulus for Fe-bearing (this study, Woodland et al. 1999), Cr-bearing (Dymshits et al. 2014), and Na and Ca-bearing (Hazen et al., 1994; Dymshits et al., 2014) majorites. In contrast, the pyrope-majorite  $\text{Mg}_3\text{Al}_2\text{Si}_3\text{O}_{12}$ - $\text{Mg}_4\text{Si}_4\text{O}_{12}$  join shows a different behavior and a low ( $\sim 160$  GPa) value of the bulk modulus for pure Mg-majorite (Liu et al. 2000; Sinogeikin and Bass 2000). A similarly low value of 168 GPa is reported by Li and Liebermann, 2007) for Mg-majorite. We note that extrapolation of our data gives 171 GPa for pure Fe-majorite. Knowledge of the density  $\rho$  and the bulk modulus  $K$  allows a calculation of the bulk sound velocity  $V_B = \sqrt{K/\rho}$  (Table 5.2.4-1 b). Extrapolation of our data for the pure Fe-majorite composition gives a value of 6.2 km/s, which is significantly lower than any estimates

for the Mg-majorite end member (Figure 5.2.4-1 b).

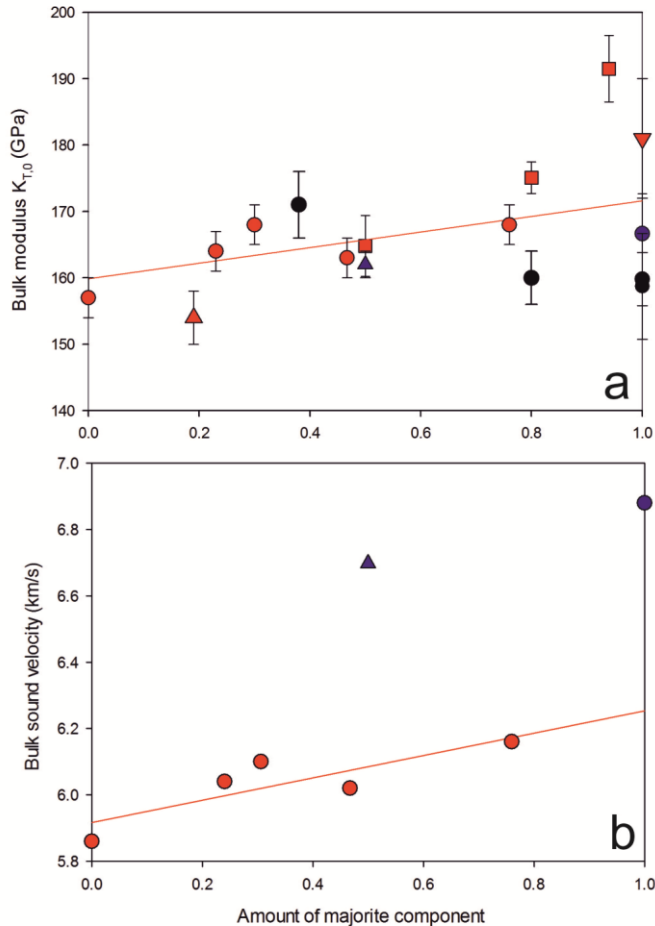


**Figure 5.2.4-1** Variation of (a) isothermal bulk moduli and (b) bulk sound velocities of garnets at 300 K as a function of majorite content as revealed by the present study and literature data. Red circles – skiaigite-majorite garnets (this study) and pure skiaigite (Woodland et al. 1999); red squares – Ca-bearing and Na-bearing majorite (Hazen et al. 1994); red triangle– majoritic knorringite (Dymshits et al., 2014); inverted red triangle– Na-majorite (Dymshits et al., 2014), blue triangle– “pyrolite minus olivine” majorite garnet  $\text{Py}_{23}\text{Alm}_6\text{Mj}_{50}\text{Gr}_{21}$  (Irfune et al. 2008); blue circle – Mg-majorite  $\text{Mg}_4\text{Si}_4\text{O}_{12}$  (Li and Liebermann 2007); black circles – Mg-majorite garnets (Liu et al. 2000, Sinogeikin and Bass, 2000). Red lines represent linear fits of our experimental data. Error bars show the

experimental uncertainties. When the value of bulk modulus was obtained with the Brillouin technique ( $K_s$ ), it was converted to  $K_0$  by applying the relationship  $K_s = K_T(1 + \alpha\gamma T)$ , where  $\alpha$  is thermal expansion,  $\gamma$  is the Grüneisen parameter, and  $T$  is temperature.

**Table 5.2.4-1 Compositions, densities and bulk sound velocities of garnets with different majorite contents.**

Composition	Density (calculated), g/cm <sup>3</sup>	Bulk sound velocity, V <sub>B</sub> (km/s)	References
Ski <sub>100</sub>	4.57	5.86	(Woodland et al. 1999)
Ski <sub>76.6</sub> Maj <sub>23.4</sub>	4.49	6.01	this study
Ski <sub>69</sub> Maj <sub>31</sub>	4.51	6.17	this study
Ski <sub>54</sub> Maj <sub>46</sub>	4.49	6.18	this study
Ski <sub>24</sub> Maj <sub>76</sub>	4.45	6.25	this study
Mg Majorite Mg <sub>4</sub> Si <sub>4</sub> O <sub>12</sub>	3.52	6.74	(Li and Liebermann 2007)
“Pyrolite minus olivine“ Py <sub>23</sub> Alm <sub>6</sub> Mj <sub>50</sub> Gr <sub>21</sub>	3.605	6.70	(Irifune et al. 2008)

Thus, our results for majorite firmly establish that the total iron content and the Fe<sup>2+</sup>/Fe<sup>3+</sup> ratio notably affect its elastic properties and the bulk sound velocity. Both therefore need to be included in the interpretation of seismological data to model the composition of the Earth’s upper mantle and transition zone. While current data on the pressure and temperature dependence of the elasticity of Fe-bearing garnets are too

limited for detailed quantitative analysis, our results provide a strong motivation for further studies in this area.

#### 5.2.4.2 Effect of spin transition on the compressibility

Recent experimental and theoretical studies on the iron spin and valence states in iron-bearing minerals suggest that pressure can induce spin-pairing transitions of  $\text{Fe}^{2+}$  and  $\text{Fe}^{3+}$  in relatively small octahedral sites such as in hematite  $\text{Fe}_2\text{O}_3$  (Badro et al., 2002; Bykova et al., 2013),  $\alpha$ - $\text{FeOOH}$  (Xu et al. 2013), siderite  $\text{FeCO}_3$  (Lavina et al. 2009; Cerantola et al. 2015),  $\text{CaFe}_2\text{O}_4$  (Merlini et al. 2010), and  $\text{Y}_3\text{Fe}_5\text{O}_{12}$  (Lyubutin et al. 2005; Gavriliuk et al. 2006; Stan et al. 2015). The reported spin-pairing transitions occur over a broad pressure range of 40 to 60 GPa. For silicate garnets, the spin-transition of  $\text{Fe}^{3+}$  was previously observed only in andradite  $\text{Ca}_3\text{Fe}_2\text{Si}_3\text{O}_{12}$  (Friedrich et al., 2014) in the pressure range of 60-70 GPa. Recently Friedrich et al. (2015) showed that  $\text{Mn}^{3+}$  can also undergo a spin transition, namely in silicate hydrogarnet henritermierite  $\text{Ca}_3\text{Mn}_2[\text{SiO}_4]_2[\text{O}_4\text{H}_4]$ , but the spin transition starts at a slightly lower pressure (55-70 GPa).

As seen in our X-ray diffraction and Mössbauer spectroscopy data for skiagite-Fe-majorite garnet, there are changes in both octahedral  $\text{Fe}^{3+}$  and  $\text{Fe}^{2+}$  between 50 and 60 GPa. The transformation is associated with a notable volume collapse that we assign to spin-pairing. To obtain the EOS coefficients of skiagite-majorite garnet  $\text{Ski}_{76.6}\text{Maj}_{23.4}$  below and above the spin crossover, we used the P-V X-ray diffraction data in two pressure intervals. The spin transition causes a reduction of the garnet unit cell volume by ~3%, which is associated with a ~7% reduction in the volume of  $(\text{Fe,Si})\text{O}_6$  octahedra (Table S 5.2.6-1).

The bulk moduli of  $\text{Ski}_{76.6}\text{Maj}_{23.4}$  garnet with iron in the high-spin and low-spin states are remarkably different at the pressure of the spin crossover 50-60 GPa:  $K_{300, 60}(\text{High Spin}) = 381(2)$  GPa and  $K_{300, 60}(\text{Low Spin}) = 531(19)$  GPa. The latter value was obtained from a fit using a 2<sup>nd</sup> order Birch-Murnaghan equation of state ( $K'$  fixed at 4) of the P-V data at pressures above 60 GPa. The bulk moduli of  $(\text{Fe,Si})\text{O}_6$  octahedra with iron in the high-spin and low-spin states are also significantly different:

$K((\text{Fe,Si})\text{O}_6)_{300,60} = 435(3)$  GPa and  $K((\text{Fe,Si})\text{O}_6)_{300,60} = 496(2)$  GPa, respectively ( $K'$  fixed at 4).

### 5.2.4.3 Does the type of cation occupying the dodecahedral site define the compressibility of garnet?

Based on density functional theory, Milman et al. 2001 suggested that the bulk modulus of garnet is strongly affected by the bulk modulus of the dodecahedra, while the compressibilities of other individual polyhedra (tetrahedra and octahedra) do not correlate with the bulk compressibility of the material. Dymshits et al. (2014) claimed that, in this case, Na-majorite  $\text{Na}_2\text{Mg}_2\text{Si}_5\text{O}_{12}$  would have the smallest bulk modulus with Na in the dodecahedral position, while experimental observations show the opposite result: Na-majorite has the highest bulk modulus (184(4) GPa) with the lowest unit-cell volume (1475.9 Å<sup>3</sup>), despite the large Na (1.07 Å) atom in the dodecahedral position. (Friedrich et al. 2014, 2015) studied the Ca-bearing garnets andradite  $\text{Ca}_3\text{Fe}_2\text{Si}_3\text{O}_{12}$  and henritetmenite  $\text{Ca}_3\text{Mn}_2[\text{SiO}_4]_2[\text{O}_4\text{H}_4]$ . While the overall bulk moduli of these garnets are significantly different (andradite- 161(4) GPa and henritetmenite- 101(1) GPa), the bulk moduli of dodecahedra in these garnets (104 GPa for andradite and 101.2(4) GPa and 88.4(8) GPa for henritetmenite) are much closer.

In the skiagite-Fe-majorite garnets studied in this work, dodecahedral sites are occupied exclusively by  $\text{Fe}^{2+}$  and the bulk moduli of dodecahedra are within the range 112-115 GPa. If the compressibility of dodecahedra was indeed the main factor that determined the bulk compressibility of garnet, all of the skiagite-Fe-majorite garnets that we investigated should have had the same bulk moduli. However, all four garnets with five different compositions (considering pure skiagite) have different bulk moduli (Table S 5.2.6-5). Thus, our results support the idea of Dymshits et al. (2014) that the compression mechanism of garnet is complex, and suggests that not only the compressibility of individual polyhedra is relevant, but also the behavior of the polyhedral framework and the bending angle between the octahedra and tetrahedra.

### 5.2.5 Conclusions

We studied skiagite-Fe-majorite garnet with four different compositions by means of synchrotron single-crystal X-ray diffraction and synchrotron Mössbauer source spectroscopy at pressures up to 90 GPa. The data on the compressibility of Fe-bearing garnets acquired in this work combined with analysis of literature data unambiguously demonstrate the influence of total iron content and  $\text{Fe}^{3+}/\text{Fe}^{2+}$  ratio in majorite on its elasticity. Thus, modelling of the composition of garnet-rich regions of the Earth's interior (the upper mantle and transition zone, in particular) and interpretation of seismological data should consider the effect of iron and its oxidation state.

We note the anomalous compressional behavior of Fe-bearing garnets along the skiagite-Fe-majorite join in the pressure range of 50 to 60 GPa. The compressibility of individual cation polyhedra combined with data from Mössbauer spectroscopy suggests spin crossover of both ferrous and ferric iron in  $(\text{Fe,Si})\text{O}_6$  octahedra in the garnet structure.

### Acknowledgments

We acknowledge the ESRF and DESY for provision of synchrotron radiation facilities.

### 5.2.6 Supplementary Materials

**Table S 5.2.6-1 Results of the crystal structure refinement based on single-crystal X-ray diffraction data for skiagite-majorite garnets with the composition  $\text{Ski}_{76.6}\text{Maj}_{23.4}$  (run S6073)**

<b>N of the run</b>	<b>S6073</b>						
Crystal system	<b>cubic</b>						
Space group	<b><math>Ia\bar{3}d</math></b>						
Z	<b>8</b>						
P, GPa	4.03(5)	8.6 (5)	11.8(6)	14.8(7)	17.6(3)	21.3(2)	26.45(1)
a (Å)	11.6194(3)	11.5171(2)	11.4665(3)	11.4126(2)	11.3700(6)	11.3143(12)	11.2405(3)
V (Å <sup>3</sup> )	1568.74(6)	1527.83(7)	1507.62(7)	1486.46(5)	1469.89(4)	1448.38(2)	1420.22(4)
Fe <sub>2</sub> O <sub>8</sub> , V <sub>0</sub> , Å <sup>3</sup>	20.5332	19.7703	19.4157	19.0478	18.7728	18.3817	17.9276
FeO <sub>6</sub> , V <sub>0</sub> , Å <sup>3</sup>	10.1701	9.9449	9.8257	9.7316	9.6324	9.5376	9.4057
SiO <sub>4</sub> , V <sub>0</sub> , Å <sup>3</sup>	2.1872	2.1687	2.1579	2.1402	2.1283	2.1122	2.0814
F(000)	2122	2122	2118	2122	2122	2122	2122
Theta range for data collection (°)	2.51/20.71	2.53/20.45	2.48/19.97	2.55/20.57	2.56/20.67	2.58/20.78	2.58/20.07
Index ranges	-12 < h < 10	-18 < h < 17	-18 < h < 17	-18 < h < 17	-13 < h < 11	-13 < h < 11	-16 < h < 18
	-19 < k < 18	-18 < k < 18	-17 < k < 18	-17 < k < 18	-18 < k < 18	-18 < k < 18	-16 < k < 16

	-19 < l < 17	-10 < l < 12	-12 < l < 11	-11 < l < 12	-18 < l < 16	-18 < l < 16	-9 < l < 14
No. of measured, independent, and observed [I > 2σ(I)] reflections	2027/289/224	1900/281/205	1956/279/212	1971/278/217	1905/276/205	1855/270/203	1647/258/169
R <sub>int</sub>	4.46	4.02	5.72	5.62	3.31	3.17	4
No. of parameters/restraints/constraints	17/0/2						
Final R indices [I > 3σ(I)] R <sub>1</sub> /wR <sub>2</sub>	0.0421/0.0576	0.0483/0.0580	0.0376/0.0466	0.0351/0.0465	0.0393/0.0517	0.0395/0.0522	0.0403/0.0452
R indices (all data) R <sub>1</sub> /wR <sub>2</sub>	0.0512/0.0597	0.0597/0.0607	0.0476/0.0497	0.0435/0.0488	0.0498/0.0540	0.0505/0.0551	0.0597/0.0476
Largest diff. peak /hole (e / Å <sup>3</sup> )	0.91/0.87						

<b>N of the run</b>	<b>S6073</b>						
Crystal system	<b>cubic</b>						
Space group	<b><i>Ia</i><math>\bar{3}</math><i>d</i></b>						
Z	<b>8</b>						
P, GPa	14.0(5)	16.78(55)	22(1)	27.7(5)	34.85(5)	40.56(12)	44.54(67)
a (Å)	11.4254(2)	11.3754(5)	11.2909(8)	11.2109(5)	11.1202(6)	11.0574(5)	11.015(4)
V (Å <sup>3</sup> )	1491.47(5)	1471.9(1)	1439.42(18)	1409.03(11)	1375.11(13)	1351.95(11)	1336.52(8)

Fe <sub>2</sub> O <sub>8</sub> , V <sub>0</sub> , Å <sup>3</sup>	19.1122	18.7803	18.2215	17.7552	17.1925	16.8509	16.6429
FeO <sub>6</sub> , V <sub>0</sub> , Å <sup>3</sup>	9.7264	9.6747	9.4936	9.3180	9.1579	9.0184	8.9068
SiO <sub>4</sub> , V <sub>0</sub> , Å <sup>3</sup>	2.1542	2.1285	2.1015	2.0719	2.0386	2.0149	2.0057
F(000)					2122	2122	2122
Theta range for data collection(°)	2.55/20.22	2.56/20.66	2.58/20.82	2.6/20.26	2.62 20.44	2.64/20.56	2.64/20.61
Index ranges	-17 < h < 14	-12 < h < 12	-12 < h < 12	-12 < h < 11	-12 < h < 11	-14 < h < 17	-14 < h < 17
	-17 < k < 14	-18 < k < 15	-17 < k < 15	-17 < k < 14	-17 < k < 14	-14 < k < 17	-14 < k < 17
	-12 < l < 14	-17 < l < 15	-14 < l < 18	-14 < l < 17	-14 < l < 17	-12 < l < 11	-12 < l < 11
No. of measured, independent, and observed [I > 2σ(I)] reflections	1781/268/205	1713/274/177	1665/269/142	1548/257/167	1524/253/152	1509/251/155	1545/254/166
R <sub>int</sub>	2.17	5.3	6.2	6.1	5.85	6.81	7.19
No. of parameters/restraints/constraints	17/0/2						
Final R indices [I > 3σ(I)] R <sub>1</sub> /wR <sub>2</sub>	0.0489/0.0609	0.0589/0.0701	0.0741/0.0764	0.0692/0.0755	0.0655/0.0715	0.0664/0.0718	0.0697/0.0787
R indices (all data) R <sub>1</sub> /wR <sub>2</sub>	0.0582/0.0624	0.0735/0.0732	0.0995/0.0804	0.0879/0.0798	0.0889/0.0745	0.0831/0.0741	0.0839/0.0804
Largest diff. peak /hole (e / Å <sup>3</sup> )	0.91/0.87						

<b>N of the run</b>	<b>S6073</b>						
Crystal system	<b>cubic</b>						
Space group	<b><i>Ia<math>\bar{3}d</math></i></b>						
Z	<b>8</b>						
P, GPa	52.15(3)	57.92(4)	62.2(8)	66.73(85)	71.55(18)	77.2(5)	80.99(42)
a (Å)	10.9287(8)	10.8128(15)	10.7485(7)	10.7125(11)	10.6679(8)	10.6373(12)	10.6150(15)
V (Å <sup>3</sup> )	1305.27(15)	1264.2(3)	1241.78(15)	1229.34(22)	1214.05(16)	1203.6(2)	1196.1(3)
Fe <sub>2</sub> O <sub>8</sub> , V <sub>0</sub> , Å <sup>3</sup>	16.2218	15.8093	15.5801	15.3870	15.1782	14.9626	14.8935
FeO <sub>6</sub> , V <sub>0</sub> , Å <sup>3</sup>	8.6497	8.0129	7.8020	7.6927	7.6053	7.5959	7.4979
SiO <sub>4</sub> , V <sub>0</sub> , Å <sup>3</sup>	1.9894	1.9873	1.9660	1.9679	1.9427	1.9409	1.9474
F(000)	2122	2122	2122	2122	2122	2122	2122
Theta range for data collection(°)	2.7/20.56	2.7/20.6	2.7/20.73	2.7/20.74	2.73/20.83	2.73/20.57	2.75/20.67
Index ranges	-12 < h < 10	-14 < h < 16	-13 < h < 17	-14 < h < 17	-16 < h < 14	-11 < h < 13	-9 < h < 13
	-17 < k < 14	-11 < k < 12	-13 < k < 16	-14 < k < 16	-17 < k < 14	-14 < k < 17	-14 < k < 17
	-14 < l < 17	-11 < l < 14	-12 < l < 11	-12 < l < 11	-11 < l < 12	-16 < l < 13	-16 < l < 13

---

Results

---

No. of measured, independent, and observed [ $I > 2\sigma(I)$ ] reflections	2736/239/192	1405/234/131	1327/233/177	1437/228/171	1426/227/170	1307/219/148	999/209/144
$R_{int}$	6.81	8.92	4.3	5.53	4.9	6.23	4.42
No. of parameters/restraints/constraints	17/0/2						
Final R indices [ $I > 3\sigma(I)$ ] $R_1/wR_2$	0.0630/0.0804	0.0619/0.0616	0.0400/0.0492	0.0598/0.0726	0.0631/0.0725	0.0473/0.0626	0.0452/0.0530
R indices (all data) $R_1/wR_2$	0.0699/0.0818	0.0943/0.0675	0.0507/0.0519	0.0713/0.0748	0.0725/0.0739	0.0609/0.0641	0.0609/0.0556
Largest diff. peak /hole ( $e / \text{\AA}^3$ )	0.91/0.87						

<b>N of the run</b>	<b>S6073</b>						
Crystal system	<b>cubic</b>						
Space group	<b><math>Ia\bar{3}d</math></b>						
Z	<b>8</b>						
P, GPa	85.6(1)	88.62(84)	1.4	2.58(16)	3.7(5)	5.0(5)	6.19(3)
$a$ (Å)	10.5875(10)	10.5706(10)	11.6788(2)	11.6570(2)	11.6347(2)	11.6001(1)	11.5762(1)
$V$ (Å <sup>3</sup> )	1186.8(2)	1181.1(4)	1592.92(5)	1584.02(5)	1574.95(5)	1560.94(2)	1551.31(2)
Fe <sub>2</sub> O <sub>8</sub> , V <sub>0</sub> , Å <sup>3</sup>	14.7310	14.5706	20.9802	20.7998	20.6589	20.3712	20.1944
FeO <sub>6</sub> , V <sub>0</sub> , Å <sup>3</sup>	7.4276	7.4139	10.3646	10.3150	10.2443	10.2285	10.1063
SiO <sub>4</sub> , V <sub>0</sub> , Å <sup>3</sup>	1.9545	1.9576	2.2139	2.1942	2.1985	2.1842	2.1906
$F(000)$	2122	2122	2122	2122	2122	2122	2122
Theta range for data collection(°)	2.75/20.73	2.76/20.76	2.49/20.92	2.5/20.64	2.5/20.68	2.51/20.74	2.52/20.73
Index ranges	-13 < $h$ < 16	-12 < $h$ < 16	-13 < $h$ < 5	-18 < $h$ < 15	-16 < $h$ < 16	-10 < $h$ < 14	-9 < $h$ < 13
	-17 < $k$ < 13	-17 < $k$ < 13	-18 < $k$ < 14	-14 < $k$ < 9	-7 < $k$ < 14	-16 < $k$ < 16	-16 < $k$ < 16
	-13 < $l$ < 11	-13 < $l$ < 11	-16 < $l$ < 16	-16 < $l$ < 16	-14 < $l$ < 18	-16 < $l$ < 18	-16 < $l$ < 18

---

Results

---

No. of measured, independent, and observed [ $I > 2s(I)$ ] reflections	1310/215/136	1259/217/87	1267/282/167	2030/295/218	1821/295/180	2130/290/223	2118/290/221
$R_{\text{int}}$	7.27	11.89	2.83	4.23	4.24	3.94	4.59
No. of parameters/restraints/constraints	17/0/2						
Final $R$ indices [ $I > 3\sigma(I)$ ] $R_1/wR_2$	0.0555/0.0586	0.0616/0.0630	0.0308/0.0398	0.0261/0.0345	0.0290/0.0365	0.0310/0.0399	0.0351/0.0424
$R$ indices (all data) $R_1/wR_2$	0.0737/0.0617	0.1399/0.0727	0.0535/0.0430	0.0352/0.0365	0.0545/0.0434	0.0373/0.0423	0.0411/0.0442
Largest diff. peak /hole ( $e / \text{\AA}^3$ )	0.91/0.87						

<b>N of the run</b>	<b>S6073</b>						
Crystal system	<b>cubic</b>						
Space group	<b><math>Ia\bar{3}d</math></b>						
Z	<b>8</b>						
P, GPa	7.45(3)	8.87(5)	10.23(5)	15.24(12)	19.99(11)	25.04(10)	31.5(16)
$a$ (Å)	11.5513(1)	11.523(1)	11.5013(2)	11.4073(2)	11.3309(2)	11.2569(3)	11.1737(3)
$V$ (Å <sup>3</sup> )	1541.32(2)	1530.18(2)	1521.39(5)	1484.39(5)	1454.77(4)	1426.45(7)	1395.05(6)
Fe <sub>2</sub> O <sub>8</sub> , V <sub>0</sub> , Å <sup>3</sup>	20.0193	19.8425	19.6693	19.0159	18.5027	18.0082	17.5111
FeO <sub>6</sub> , V <sub>0</sub> , Å <sup>3</sup>	10,0797	9.9496	9.9150	9.7056	9.5548	9.4246	9.2460
SiO <sub>4</sub> , V <sub>0</sub> , Å <sup>3</sup>	1.9545	2.1164	2.1609	2.1404	2.1174	2.0946	2.0633
$F(000)$	2122						
Theta range for data collection(°)	2.75/20.73	2.53/20.89	2.53/20.93	2.55/20.83	2.57/20.74	2.59/20.53	2.61/20.75
Index ranges	-13 < $h$ < 16	-13 < $h$ < 9	-9 < $h$ < 13	-16 < $h$ < 16	-7 < $h$ < 12	-16 < $h$ < 16	-16 < $h$ < 16
	-17 < $k$ < 13	-16 < $k$ < 16	-16 < $k$ < 18	-7 < $k$ < 12	-17 < $k$ < 18	-17 < $k$ < 15	-18 < $k$ < 15
	-13 < $l$ < 11	-16 < $l$ < 18	-16 < $l$ < 16	-18 < $l$ < 16	-16 < $l$ < 17	-7 < $l$ < 12	-7 < $l$ < 12

No. of measured, independent, and observed [ $I > 2s(I)$ ] reflections	1310/215/136	2103/286/236	2085/286/232	1732/274/218	1963/276/214	1694/265/200	1654/260/188
$R_{\text{int}}$	7.27	6.22	4.16	3.52	5.3	3.0	3.04
No. of parameters/restraints/constraints	17/0/2						
Final $R$ indices [ $I > 3\sigma(I)$ ] $R_1/wR_2$	0.0555/0.0586	0.0286/0.0384	0.0288/0.0364	0.0273/0.0363	0.0301/0.0301	0.0394/0.0490	0.0387/0.0468
$R$ indices (all data) $R_1/wR_2$	0.0737/0.0617	0.0334/0.0397	0.0340/0.0379	0.0348/0.0387	0.0375/0.0375	0.0491/0.0517	0.0503/0.0491
Largest diff. peak /hole ( $e/\text{\AA}^3$ )	0.91/0.87						

**Table S 5.2.6-2 Results of the crystal structure refinement based on single-crystal X-ray diffraction data for skiagite-majorite garnets with the composition Ski<sub>69</sub>Maj<sub>31</sub> (S6176 run)**

<b>N of the run</b>	<b>S6176</b>						
Crystal system	<b>cubic</b>						
Space group	<b><i>Ia<math>\bar{3}d</math></i></b>						
Z	<b>8</b>						
P, GPa	0.3(5)	1.03(5)	2.9(5)	4.89(5)	6.94(5)	9.86(5)	14.8(5)
a (Å)	11.7094(3)	11.6945(3)	11.6530(2)	11.6100(2)	11.5679(3)	11.5120(2)	11.4363(2)
V (Å <sup>3</sup> )	1605.48(12)	1599.36(12)	1582.39(8)	1564.94(8)	1547.97(12)	1525.64(8)	1495.74(8)
Fe <sub>2</sub> O <sub>8</sub> , V <sub>0</sub> , Å <sup>3</sup>	21.2155	21.1308	20.772	20.4502	20.1509	19.7359	19.1866
FeO <sub>6</sub> , V <sub>0</sub> , Å <sup>3</sup>	10.3431	10.3179	10.2325	10.1364	10.0507	9.9419	9.7845
SiO <sub>4</sub> , V <sub>0</sub> , Å <sup>3</sup>	2.2107	1.6348	2.1963	2.1886	2.1765	2.164	2.1487
F(000)	1152	1152	1152	3242	3243	3241	3241
Theta range for data collection(°)	2.658/17.585	1.742/17.821	1.748/17.795	1.755/17.679	1.761/17.745	1.770/ 17.834	1.782/17.703
Index ranges	-18 < h < 12	-20 < h < 20	-18 < h < 15	-19 < h < 20	-18 < h < 15	-19 < h < 10	-19 < h < 19
	-18 < k < 18	-15 < k < 18	-20 < k < 20	-15 < k < 19	-19 < k < 19	-18 < k < 15	-15 < k < 17

Results

	-17 < l < 13	-15 < l < 19	-19 < l < 15	-15 < l < 18	-19 < l < 15	-15 < l < 18	-15 < l < 18
No. of measured, independent, and observed [I > 2s(I)] reflections	4001/415/304	4632/475/360	4575/472/356	4525/462/374	4464/460/348	4414/455/358	4295/449/344
R <sub>int</sub>	0.0436	0.0452	0.0371	0.0333	0.0399	0.0319	0.0434
No. of parameters/restraints	19/0						
Final R indices [I > 2σ(I)]R <sub>1</sub> /wR <sub>2</sub>	0.0407/0.1023	0.0364/0.0914	0.0365/0.0932	0.0332/0.0847	0.0341/0.0898	0.0320/0.0786	0.0296/0.0799
R indices (all data)R <sub>1</sub> /wR <sub>2</sub>	0.0616/0.1273	0.0516/0.1050	0.0487/0.1098	0.0410/0.0928	0.0426/0.0982	0.0419/0.0878	0.0443/0.0888
Largest diff. peak /hole (e / Å <sup>3</sup> )	-1.291/0.261	-1.238/0.227	-1.262/0.257	-1.191/0.262	-1.234/0.237	-0.999/0.234	-0.657/0.175

<b>N of the run</b>	<b>S6176</b>						
Crystal system	<b>cubic</b>						
Space group	<b><i>Ia<math>\bar{3}d</math></i></b>						
Z	<b>8</b>						
P, GPa	18.39(5)	23.58(17)	28.38(5)	33.17(8)	38.48(16)	42.85(5)	46.73(5)
a (Å)	11.3653(2)	11.2905(2)	11.2250(3)	11.1624(4)	11.1005(4)	11.0511(4)	11.0102(4)
V (Å <sup>3</sup> )	1468.06(8)	1439.26(8)	1414.36(11)	1390.83(15)	1367.82(15)	1349.64(15)	1334.71(15)
Fe <sub>2</sub> O <sub>8</sub> , V <sub>0</sub> , Å <sup>3</sup>	18.738	18.253	17.8229	17.4541	17.0841	16.8064	16.6071
FeO <sub>6</sub> , V <sub>0</sub> , Å <sup>3</sup>	9.6551	9.4798	9.3459	9.2228	9.1037	8.9975	8.9082
SiO <sub>4</sub> , V <sub>0</sub> , Å <sup>3</sup>	2.1197	2.101	2.0827	2.0603	2.039	2.0264	2.0142
F(000)	3241	3242	3242	3239	3240	3243	3242
Theta range for data collection(°)	1.793/17.87	1.805/17.613	1.815/17.70	1.825/17.622	1.835/17.723	1.844/17.805	1.851/17.805
Index ranges	-19 < h < 19	-15 < h < 18	-17 < h < 15	-17 < h < 14	-17 < h < 14	-17 < h < 14	-18 < h < 18
	-17 < k < 15	-19 < k < 19	-19 < k < 19	-18 < k < 19	-18 < k < 18	-17 < k < 14	-17 < k < 14
	-15 < l < 18	-15 < l < 17	-18 < l < 14	-18 < l < 14	-18 < l < 14	-18 < l < 18	-14 < l < 17

---

Results

---

No. of measured, independent, and observed [ $I > 2\sigma(I)$ ] reflections	4187/438/345	4090/433/337	3965/425/305	3901/408/294	3822/401/281	3798/401/313	3771/396/296
$R_{int}$	0.0345	0.0366	0.0409	0.0443	0.0445	0.0361	0.0399
No. of parameters/restraints	19/0						
Final R indices [ $I > 2\sigma(I)$ ] $R_1/wR_2$	0.0280/0.0702	0.0276/0.0681	0.0340/0.0896	0.0347/0.0830	0.0391/0.1034	0.0364/0.0859	0.0386/0.0929
R indices (all data) $R_1/wR_2$	0.0381/0.0841	0.0384/0.0790	0.0515/0.1054	0.0528/0.1018	0.0391/0.1034	0.0492/0.0964	0.0525/0.1042
Largest diff. peak /hole ( $e / \text{\AA}^3$ )	-0.719/0.187	-0.696/ 0.186	-0.961/0.201	-0.766/0.206	-1.188/0.226	-1.231/0.289	-1.329/0.273

<b>N of the run</b>	<b>S6176</b>							
Crystal system	<b>cubic</b>							
Space group	<b><i>Ia<math>\bar{3}d</math></i></b>							
Z	<b>8</b>							
P, GPa	49.6(12)	52.0(5)	54.04(3)	55.17(5)	56.0(5)	56.97(7)	58.13(9)	60.16(9)
a (Å)	10.9774(5)	10.9448(5)	10.8932(6)	10.8801(5)	10.8559(6)	10.8453(5)	10.8159(6)	10.7828(8)
V (Å <sup>3</sup> )	1322.81(18)	1311.06(18)	1292.6(2)	1287.95(18)	1279.4(2)	1275.63(18)	1265.3(2)	1253.7(3)
Fe <sub>2</sub> O <sub>8</sub> , V <sub>0</sub> , Å <sup>3</sup>	16.4316	16.3077	16.102	16.0653	15.982	15.942	15.8382	15.7221
FeO <sub>6</sub> , V <sub>0</sub> , Å <sup>3</sup>	8.8456	8.7276	8.4812	8.3721	8.2449	8.1895	8.0308	7.8845
SiO <sub>4</sub> , V <sub>0</sub> , Å <sup>3</sup>	2.0019	1.9936	1.9857	1.9947	1.9944	1.9886	1.9865	1.9817
F(000)	3241	3240	3238	3234	3235	3235	3235	3235
Theta range for data collection(°)	1.856/17.757	1.862/17.638	1.870/17.724	1.873/17.746	1.877/17.432	1.879/17.450	1.884/17.499	1.890/17.554
Index ranges	-18 < h < 14	-18 < h < 18	-16 < h < 14	-16 < h < 14	-18 < h < 18	-14 < h < 16	-13 < h < 16	-13 < h < 16
	-16 < k < 14	-14 < k < 16	-18 < k < 18	-18 < k < 18	-14 < k < 16	-14 < k < 17	-14 < k < 18	-14 < k < 17
	-18 < l < 18	-14 < l < 17	-18 < l < 14	-18 < l < 14	-14 < l < 17	-18 < l < 18	-18 < l < 18	-18 < l < 17

No. of measured, independent, and observed [ $I > 2\sigma(I)$ ] reflections	3718/394/293	3687/391/271	3572/386/241	3580/385/276	3522/383/259	3594/379/291	3551/377/281	3475/373/272
$R_{int}$	0.0385	0.0579	0.0694	0.0528	0.0680	0.0372	0.0470	0.0546
No. of parameters/restraints	19/0							
Final R indices [ $I > 2\sigma(I)$ ] $R_1/wR_2$	0.0375/0.0932	0.0387/0.1001	0.0533/0.1391	0.0372/0.0943	0.0485/0.1215	0.0395/0.1052	0.0545/0.1152	0.0615/0.1243
R indices (all data) $R_1/wR_2$	0.0516/0.1023	0.0594/0.1131	0.0792/0.1635	0.0565/0.1075	0.074/0.1384	0.0512/0.1140	-1.307/0.335	-1.173/0.313
Largest diff. peak /hole ( $e / \text{\AA}^3$ )	-1.196/0.258	-1.091/0.214	-0.998/0.288	-0.893/0.259	-0.809/0.300	-1.635/0.361	-0.657/0.175	-0.657/0.175

**Table S 5.2.6-3 Results of the crystal structure refinement based on single-crystal X-ray diffraction data for skiagite-majorite garnets with the composition  $\text{Ski}_{54}\text{Maj}_{46}$  (S6177 run)**

<b>N of the run</b>	<b>S6177</b>						
Crystal system	<b>cubic</b>						
Space group	<b><math>Ia\bar{3}d</math></b>						
Z	<b>8</b>						
P, GPa	0.3(5)	1.03(5)	2.9(5)	4.89(5)	6.94(5)	9.86(5)	14.8(5)
a (Å)	11.6958(3)	11.6768(3)	11.6360(3)	11.5945(3)	11.5527(3)	11.4984(3)	11.4199(3)
V (Å <sup>3</sup> )	1599.89(12)	1592.10(12)	1575.47(12)	1558.68(12)	1541.88(12)	1520.24(12)	1489.32(12)
Fe <sub>2</sub> O <sub>8</sub> , V <sub>0</sub> , Å <sup>3</sup>	21.2752	21.0777	20.7748	20.4598	20.1553	19.7663	19.1954
FeO <sub>6</sub> , V <sub>0</sub> , Å <sup>3</sup>	10.2376	10.1766	10.0838	9.9915	9.9303	9.8106	9.6539
SiO <sub>4</sub> , V <sub>0</sub> , Å <sup>3</sup>	2.1944	2.2066	2.1957	2.1879	2.1714	2.1604	2.143
F(000)	3223	3219	3220	3220	3220	3221	3221
Theta range for data collection(°)	1.742/17.849	1.745 /17.758	1.751/ 17.638	1.757/ 17.703	1.764/ 17.769	1.772/17.793	1.784/17.472
Index ranges	-19 < h < 21	-22 < h < 21	-22 < h < 21	-22 < h < 21	-22 < h < 21	-21 < h < 21	-21 < h < 20
	-13 < k < 15	-22 < k < 21	-22 < k < 14	-22 < k < 14	-22 < k < 21	-22 < k < 21	-21 < k < 21

Results

	-19 < l < 20	-15 < l < 16	-14 < l < 16				
No. of measured, independent, and observed [I > 2σ(I)] reflections	4042/518/304	4592/539/339	4568/530/373	4482/523/373	4422/510/370	4343/503/353	4259/495/317
R <sub>int</sub>	0.0528	0.0966	0.0538	0.0567	0.0528	0.0558	0.0900
No. of parameters/restraints	19/0						
Final R indices [I > 2σ(I)]R <sub>1</sub> /wR <sub>2</sub>	0.0407/0.0805	0.0394/0.0994	0.0340/0.0879	0.0353/0.0882	0.0367/0.0838	0.0320/0.0862	0.0392/0.0946
R indices (all data)R <sub>1</sub> /wR <sub>2</sub>	0.0742/0.0805	0.0628/0.1191	0.0501/0.1010	0.0513/0.1031	0.0527/0.0913	0.0560/0.1046	0.0703/0.1210
Largest diff. peak /hole (e / Å <sup>3</sup> )	-0.593/0.188	-1.235/0.256	-1.225/ 0.219	-0.958/0.209	-1.031/0.216	-0.843/0.195	-1.089/0.209

<b>N of the run</b>	<b>S6177</b>						
Crystal system	<b>cubic</b>						
Space group	<b><i>Ia<math>\bar{3}d</math></i></b>						
Z	<b>8</b>						
P, GPa	18.39(5)	23.58(17)	28.38(5)	33.17(8)	38.48(16)	42.85(5)	46.73(5)
a (Å)	11.3545(3)	11.2812(4)	11.2123(4)	11.1518(3)	11.0905(4)	11.0415(5)	11.0014(4)
V (Å <sup>3</sup> )	1463.88(12)	1435.71(9)	1409.56(9)	1386.87(11)	1364.12(15)	1346.12(18)	1331.51(8)
Fe <sub>2</sub> O <sub>8</sub> , V <sub>0</sub> , Å <sup>3</sup>	18.7565	18.2748	17.8608	17.4433	17.0804	16.824	16.6238
FeO <sub>6</sub> , V <sub>0</sub> , Å <sup>3</sup>	9.4949	9.3549	9.2176	9.085	8.9661	8.8691	8.7892
SiO <sub>4</sub> , V <sub>0</sub> , Å <sup>3</sup>	2.1282	2.1043	2.0781	2.0716	2.0492	2.036	2.016
F(000)	3221	3221	3221	5110	5110	5110	2102
Theta range for data collection(°)	1.794/17.576	1.81/17.69	1.8/17.63	1.827/17.773	1.837/17.536	1.845/17.582	1.81/17.2
Index ranges	-14 < h < 16	-16 < h < 14	-16 < h < 14	-15 < h < 13	-15 < h < 13	-13 < h < 14	-13 < h < 14
	-21 < k < 20	-21 < k < 20	-21 < k < 20	-20 < k < 20	-20 < k < 19	-19 < k < 20	-19 < k < 20
	-21 < l < 20	-21 < l < 20	-21 < l < 20	-21 < l < 19	-15 < l < 13	-19 < l < 20	-19 < l < 20

---

Results

---

No. of measured, independent, and observed [ $I > 2\sigma(I)$ ] reflections	4197/485/344	4123/482/282	4026/469/267	3971/458/ 347	3887/452/346	3810/45/341	3750/432/301
$R_{int}$	0.0528	0.0966	0.0538	0.0518	0.0491	0.0483	0.0435
No.of parameters/restraints	19/0						
Final R indices [ $I > 2\sigma(I)$ ] $R_1/wR_2$	1.020	1.027	1.081	0.0397/0.0903	0.0398/0.0887	0.0535/0.1021	0.0376/0.0481
R indices (all data) $R_1/wR_2$	0.0407/0.0805	0.0394/0.0994	0.0340/0.0879	0.0544/0.1039	0.0573/0.0985	0.0399/0.0920	0.0544/0.0505
Largest diff. peak /hole ( $e / \text{\AA}^3$ )	0.0742/0.0805	0.0628/0.1191	0.0501/0.1010	-1.412/0.338	-1.286/0.366	-1.354/0.340	-1.354/0.340

<b>N of the run</b>	<b>S6177</b>							
Crystal system	<b>cubic</b>							
Space group	<b><i>Ia<math>\bar{3}d</math></i></b>							
Z	<b>8</b>							
P, GPa	49.6(12)	52.0(5)	54.04(3)	55.17(5)	56.0(5)	56.97(7)	58.13(9)	60.16(9)
a (Å)	10.9694(5)	10.9392(4)	10.8993(4)	10.8835(4)	10.8643(4)	10.8391(4)	10.8129(4)	10.7843(4)
V (Å <sup>3</sup> )	1319.92(10)	1309.05(8)	1294.78(8)	1289.16(8)	1282.35(8)	1273.44(8)	1264.23(8)	1254.23(8)
Fe <sub>2</sub> O <sub>8</sub> , V <sub>0</sub> , Å <sup>3</sup>	16.4411	16.2985	16.1649	16.1077	16.0459	15.9789	15.8577	15.7631
FeO <sub>6</sub> , V <sub>0</sub> , Å <sup>3</sup>	8.7103	8.6057	8.4300	8.3347	8.2123	8.0683	7.9501	7.8373
SiO <sub>4</sub> , V <sub>0</sub> , Å <sup>3</sup>	2.0124	2.01	2.0045	2.0057	2.0037	2.0067	2.0033	2.0022
F(000)	5110	5110	5110	2102	2101	2102	2097	2099
Theta range for data collection(°)	1.827/17.773	1.837/17.536	1.845/17.582	1.81/17.2	1.81/17.2	1.81/17.2	1.88/17.71	1.88/17.58
Index ranges	-15 < h < 13	-15 < h < 13	-13 < h < 14	-19 < h < 20	-19 < h < 20			
	-20 < k < 20	-20 < k < 19	-19 < k < 20					
	-21 < l < 19	-15 < l < 13	-19 < l < 20	-19 < l < 20	-20 < l < 20	-20 < l < 20	-12 < l < 14	-12 < l < 14

## Results

No. of measured, independent, and observed [ $I > 2s(I)$ ] reflections	3971/458/347	3887/452/346	3810/45/341	3750/432/301	3731/434/296	3698/431/292	3545/417/275	3516/413/284
$R_{\text{int}}$	0.0518	0.0491	0.0483	0.0435	0.0575	0.0568	0.0656	0.0664
No. of parameters/restraints	18/0/2							
Final R indices [ $I > 2\sigma(I)$ ] $R_1/wR_2$	2.52	2.69	1.79	1.87	1.42	2.02	2.12	1.79
R indices (all data) $R_1/wR_2$	0.0424/0.0710	0.0475/0.0725	0.0353/0.0472	0.0377/0.0559	0.0344/0.0426	0.0398/0.0579	0.0462/0.0607	0.0400/0.0496
Largest diff. peak /hole ( $e / \text{\AA}^3$ )	0.0597/0.0730	0.0648/0.0741	0.0517/0.0489	0.0571/0.0592	0.0564/0.0472	0.0666/0.0614	0.0674/0.0632	0.0564/0.0521

**Table S 5.2.6-4 Results of the crystal structure refinement based on single-crystal X-ray diffraction data for skiagite-majorite garnets with the composition  $\text{Ski}_{24}\text{Maj}_{76}$  (S6160 run)**

<b>N of the run</b>	<b>S6160</b>						
Crystal system	<b>cubic</b>						
Space group	<b><math>Ia\bar{3}d</math></b>						
Z	<b>8</b>						
P, GPa	0.3(5)	1.03(5)	2.9(5)	4.89(5)	6.94(5)	9.86(5)	14.8(5)
$a$ (Å)	11.6685(3)	11.6556(3)	11.6149(2)	11.5736(2)	11.5321(3)	11.4785(2)	11.4079(2)
$V$ (Å <sup>3</sup> )	1588.71(12)	1583.45(12)	1566.92(8)	1550.26(8)	1533.65(12)	1512.36(8)	1484.63(8)
$\text{Fe}_2\text{O}_8$ , $V_0$ , Å <sup>3</sup>	21.205	21.125	20.817	20.504	20.181	19.7797	19.2899
$\text{FeO}_6$ , $V_0$ , Å <sup>3</sup>	9.97	9.939	9.857	9.787	9.6776	9.5734	9.4445
$\text{SiO}_4$ , $V_0$ , Å <sup>3</sup>	2.208	2.204	2.194	2.182	2.1791	2.1687	2.1445
$F(000)$	1152	1152	1152	1152	1152	1152	1152
Theta range for data collection(°)	1.746/17.771	1.748/17.852	1.754/17.856	1.760/17.798	1.767/17.424	1.775/17.508	1.786/17.620
Index ranges	$-22 < h < 21$	$-20 < h < 20$	$-18 < h < 15$	$-20 < h < 20$	$-18 < h < 15$	$-20 < h < 20$	$-20 < h < 20$

	-24 < k < 21	-21 < k < 21	-21 < k < 21	-21 < k < 21	-20 < k < 20	-21 < k < 22	-21 < k < 21
	-12 < l < 17	-18 < l < 15	-20 < l < 20	-18 < l < 15	-21 < l < 21	-15 < l < 18	-17 < l < 14
No. of measured, independent, and observed [ $I > 2s(I)$ ] reflections	4069/530/345	4627/529/369	4551/519/386	4502/516/371	4467/515/380	4377/510/387	4290/503/373
$R_{\text{int}}$	0.0441	0.0587	0.0382	0.0504	0.0460	0.0398	0.0641
No. of parameters/restraints	21/0	21/0	19/0				
Final $R$ indices [ $I > 2\sigma(I)$ ] $R_1/wR_2$	0.0338/0.0875	0.0348/0.0880	0.0286/0.0695	0.0434/0.0689	0.0327/0.0800	0.0299/0.0706	0.0333/0.0809
$R$ indices (all data) $R_1/wR_2$	0.0593/0.1057	0.0523/0.1055	0.0404/0.0821	0.0434/0.0801	0.0479/0.1003	0.0412/0.0819	0.0454/0.0930
Largest diff. peak /hole ( $e / \text{\AA}^3$ )	-0.719/0.203	-1.087/0.261	-0.900/0.199	-0.677/0.186	-1.120/ 0.220	-0.837/0.223	-1.090/0.266

<b>N of the run</b>	<b>S6160</b>							
Crystal system	<b>cubic</b>							
Space group	<b><i>Ia<math>\bar{3}d</math></i></b>							
Z	<b>8</b>							
P, GPa	49.6(12)	52.0(5)	54.04(3)	55.17(5)	56.0(5)	56.97(7)	58.13(9)	60.16(9)
<i>a</i> (Å)	10.9497(5)	10.9211(5)	10.8804(5)	10.8640(5)	10.8520(5)	10.8298(5)	10.8070(5)	10.7831(5)
<i>V</i> (Å <sup>3</sup> )	1312.82(18)	1302.56(18)	1288.06(18)	1282.24(18)	1278.00(18)	1270.17(18)	1262.16(18)	1253.81(17)
Fe <sub>2</sub> O <sub>8</sub> , V <sub>0</sub> , Å <sup>3</sup>	16.4451	16.3339	16.1645	16.1176	16.0563	15.9738	15.9662	15.8018
FeO <sub>6</sub> , V <sub>0</sub> , Å <sup>3</sup>	8.5047	8.4223	8.234	8.1582	8.0879	7.9683	7.8638	7.7668
SiO <sub>4</sub> , V <sub>0</sub> , Å <sup>3</sup>	2.0135	2.0021	1.9995	1.9936	1.9979	1.9979	1.9904	1.9905
<i>F</i> (000)	1152							
Theta range for data collection(°)	1.861/17.734	1.866/17.782	1.873/17.675	1.875/17.703	1.878/17.581	1.881/17.619	1.885/17.657	1.890/17.626
Index ranges	-20 < <i>h</i> < 19	-20 < <i>h</i> < 19	-19 < <i>h</i> < 19	-19 < <i>h</i> < 19	-19 < <i>h</i> < 19	-18 < <i>h</i> < 14	-21 < <i>h</i> < 21	-18 < <i>h</i> < 15
	-21 < <i>k</i> < 21	-21 < <i>k</i> < 21	-21 < <i>k</i> < 21	-21 < <i>k</i> < 21	-21 < <i>k</i> < 21	-21 < <i>k</i> < 21	-20 < <i>k</i> < 20	-21 < <i>k</i> < 21
	-14 < <i>l</i> < 17	-14 < <i>l</i> < 17	-14 < <i>l</i> < 17	-14 < <i>l</i> < 17	-14 < <i>l</i> < 17	-19 < <i>l</i> < 19	-18 < <i>l</i> < 14	-19 < <i>l</i> < 19
No. of measured, independent,	3723/447/321	3682/444/316	3647/438/302	3620/435/302	3622/432/307	3602/433/314	3612/434/310	3592/433/309

and observed $[I > 2\sigma(I)]$ reflections								
$R_{\text{int}}$	0.0481	0.0443	0.0545	0.0457	0.0541	0.0558	0.0560	0.0552
No. of parameters/ restraints	19/0							
Final $R$ indices $[I > 2\sigma(I)]R_1 wR_2$	0.0397/0.0970	0.0381/0.0985	0.0371/0.0963	0.0358/0.0936	0.0348/0.0904	0.0371/0.0929	0.0414/0.1060	0.0395/0.0998
$R$ indices (all data) $R_1/wR_2$	0.0566/0.1188	0.0555/0.1144	0.0547/0.1143	0.0534/0.1174	0.0515/0.1081	0.0539/0.1097	0.0596/0.1258	0.0545/0.1175
Largest diff. peak/hole ( $e / \text{\AA}^3$ )	-0.733/ 0.240	-0.673/0.223	-0.696/0.208	-0.731/0.228	-0.805/ 0.199	-0.987/ 0.221	-1.116/0.290	-1.092/ 0.302

**Table S 5.2.6-5 Results of the fit of the P-V experimental data using the 2<sup>nd</sup> order Birch-Murnaghan equation of state.**

Composition	Results of the fit with the 2 <sup>nd</sup> order Birch-Murnaghan equation of state ( $K'$ fixed at 4)			
	unit cell	(Fe,Si)O <sub>6</sub>	Fe <sub>2</sub> O <sub>8</sub>	SiO <sub>4</sub>
	V <sub>0</sub> , Å <sup>3</sup>	V <sub>0</sub> , Å <sup>3</sup>	V <sub>0</sub> , Å <sup>3</sup>	V <sub>0</sub> , Å <sup>3</sup>
	K <sub>0,300</sub> , GPa	K <sub>0,300</sub> , GPa	K <sub>0,300</sub> , GPa	K <sub>0,300</sub> , GPa
Ski <sub>76.6</sub> Maj <sub>23.4</sub>	High Spin	High Spin		
	1608.1(4)	10.349(7)		
	162.4(6)	216(2)	21.35(2)	2.214(2)
	Low Spin	Low Spin	101(1)	386(7)
	1435(11)	9.14(15)		
	306(18)	271(30)		
Ski <sub>69</sub> Maj <sub>31</sub>	1606(2)	10.336(9)	21.25(4)	2.213(1)
	172(1)	232(2)	115(1)	405(3)
Ski <sub>54</sub> Maj <sub>46</sub>	1603.91	10.335(9)	21.23	2.209(2)

	171.8(3)	233(2)	115(2)	482(9)
Ski <sub>24</sub> Maj <sub>76</sub>	1591.8(8)	9.971(13)	21.34(3)	2.208(1)
	174(2)	227(3)	112.8(9)	483(7)
Ski <sub>100</sub> (Woodland et al. 1999)	175.5(1.4)	-	-	-

### 5.3 Stability of Fe,Al-bearing bridgmanite in the lower mantle and synthesis of pure Fe-bridgmanite

Leyla Ismailova<sup>1,2</sup>, Elena Bykova<sup>1</sup>, Maxim Bykov<sup>1</sup>, Valerio Cerantola<sup>1,3</sup>, Catherine McCammon<sup>1</sup>, Tiziana Boffa Ballaran<sup>1</sup>, Andrey Bobrov<sup>4</sup>, Ryosuke Sinmyo<sup>1</sup>, Natalia Dubrovinskaia<sup>2</sup>, Konstantin Glazyrin<sup>5</sup>, Hanns-Peter Liermann<sup>5</sup>, Ilya Kupenko<sup>1,3</sup>, Michael Hanfland<sup>3</sup>, Clemens Prescher<sup>6</sup>, Vitali Prakapenka<sup>6</sup>, Volodymir Svitlyk<sup>3</sup>, Leonid Dubrovinsky<sup>1\*</sup>

*Published in Science Advances 2 : e1600427*

<sup>1</sup>Bayerisches Geoinstitut, University of Bayreuth, D-95440 Bayreuth, Germany.

<sup>2</sup>Laboratory of Crystallography, University of Bayreuth, D-95440 Bayreuth, Germany.

<sup>3</sup>European Synchrotron Radiation Facility, BP 220, Grenoble F-38043, France.

<sup>4</sup> Department of Petrology, Geological Faculty, Moscow State University, 119234 Moscow, Russia

<sup>5</sup>Photon Sciences, Deutsches Elektronen-Synchrotron, Notkestrasse 85, D-22603 Hamburg, Germany.

<sup>6</sup>Center for Advanced Radiation Sources, University of Chicago, 9700 South Cass Ave, IL 60437 Argonne, USA.

#### **Abstract**

The physical and chemical properties of the Earth's mantle as well as its dynamics and evolution depend heavily on the phase composition of the region. Based on experiments in laser-heated diamond anvil cells we demonstrate that Fe,Al-bearing bridgmanite (magnesium silicate perovskite) is stable to pressures over 120 GPa and temperatures above 3000 K. Ferric iron stabilizes Fe-rich bridgmanite such that we were able to synthesize pure iron silicate perovskite at pressures between ~45 GPa and 110 GPa. The compressibility of ferric iron-bearing bridgmanite is significantly different to any

known silicate perovskites, which has direct implications for the interpretation of seismic tomography data.

### 5.3.1 Main Text

The lower mantle constitutes more than half of the Earth's interior by volume and is believed to consist predominantly of bridgmanite (perovskite-structured  $(\text{Mg,Fe})(\text{Si,Al})\text{O}_3$ ) with up to approximately 20% ferropericlase  $(\text{Mg,Fe})\text{O}$  by volume (Tschauner et al., 2014; Murakami et al., 2004). Thus, the physical properties, crystal chemistry, and stability of bridgmanite at high pressures and temperatures are critical for understanding the structure and dynamics of our planet, as well as the interior of other terrestrial planets as well as exoplanets. Ever since the application of laser heated diamond anvil cell (DAC) techniques and X-ray diffraction allowed the major components of the lower mantle to be identified (Liu 1975), investigations of perovskite-structured silicates have been a popular focus of mineral physics studies. Over the decades there have been several claims that bridgmanite undergoes structural transformations (Andrault 2001; Shim et al. 2001; Murakami et al. 2004) or that the phase is not chemically stable at all conditions within the lower mantle (Saxena et al. 1996; Andrault and Fiquet 2001; Zhang et al. 2014). So far, however, only one phase transition in  $(\text{Mg,Fe})(\text{Si,Al})\text{O}_3$  bridgmanite has been unambiguously confirmed, namely to a  $\text{CaIrO}_3$ -type structure phase (often called post-perovskite, PPv) above  $\sim 125$  GPa and at high temperatures (Murakami et al. 2004). Earlier observations (Andrault 2001; Shim et al. 2001) of decomposition were probably due to large temperature gradients resulting in Soret or Gorsky effects arising from one-sided highly focused laser heating (Andrault and Fiquet 2001; Dorfman et al. 2012). Recently, using more advanced set ups for laser-heated diamond anvil cell experiments, Zhang et al. (Zhang et al. 2014) reported that Fe-bearing silicate perovskite is unstable at pressures of 95-101 GPa and temperatures of 2200~2400 K, where it loses its iron component and decomposes into a nearly Fe-free  $\text{MgSiO}_3$  perovskite and a Fe-rich  $(\text{Mg,Fe})\text{SiO}_3$  phase ("H-phase") with a hexagonal structure not previously known, causing a small volume reduction in bridgmanite. The hexagonal phase can be synthesized at pressures as low

as ~85 GPa. These findings may be of primary relevance for geophysical, geochemical and geodynamic models of the lower mantle below depths of 2000 km. Changes in the pseudo-binary  $\text{MgSiO}_3\text{-FeSiO}_3$  phase relations could be associated with spin crossover of iron above ~60 GPa and drastic modifications of its crystal chemistry. However, structural data on  $(\text{Mg,Fe})(\text{Si,Al})\text{O}_3$  bridgmanite in the megabar pressure range and ~2000 K are very limited, and its possible decomposition with formation of the H-phase is inconsistent with some experimental observations (Andrault 2001; Mao et al. 2004; Glazyrin et al. 2014; Wolf et al. 2015). Here we apply single crystal X-ray diffraction (SCXRD) in laser-heated diamond anvil cells (DACs) (see Methods, Supplementary Information) in order to study stability of iron (and aluminum) bearing bridgmanite at conditions of the deep part of the Earth's lower mantle.

Single crystals of bridgmanite with different compositions,  $\text{Mg}_{0.83}\text{Fe}_{0.17}\text{Al}_{0.06}\text{Si}_{0.94}\text{O}_3$  (referred to below as FE17),  $\text{Mg}_{0.86}\text{Fe}_{0.14}\text{Al}_{0.04}\text{Si}_{0.96}\text{O}_3$  (FE14), and  $\text{Mg}_{0.60}\text{Fe}_{0.40}\text{Si}_{0.63}\text{Al}_{0.37}\text{O}_3$  (FE40), as determined from SCXRD structural refinement and microprobe analysis, were selected from samples synthesized in a multi-anvil apparatus at 25 GPa and 1300 °C. According to Mössbauer spectroscopy, the ratio  $\text{Fe}^{3+}/\Sigma\text{Fe}$  is 0.93(3) (Glazyrin et al. 2014) in FE40 and 0.20(3) in FE17 and FE14 (Kupenko et al. 2014). Before being loaded into a DAC, crystals with sizes from ~10 x 10 x 5  $\mu\text{m}^3$  to ~20 x 20 x 7  $\mu\text{m}^3$  were selected and tested using an *in house* high-brilliance rotating anode diffractometer (Dubrovinsky et al. 2006). X-ray diffraction measurements were carried out in angle-dispersive mode at the 13-IDD beamline ( $\lambda=0.31$  Å, beam size 5x5  $\mu\text{m}^2$ ) at APS, USA, at the ID09a ( $\lambda=0.41$  Å, beam size 10x10  $\mu\text{m}^2$ ) and ID27 ( $\lambda=0.37$  Å, beam size 3x3  $\mu\text{m}^2$ ) beamlines at ESRF, France, and at the extreme conditions beamline P02.2 ( $\lambda=0.2903$  Å, beam size 3x8  $\mu\text{m}^2$ ) PETRA III, DESY, Germany (see *Supplementary Materials* for more details). The samples were loaded at ~1.4 kbar in Ne pressure transmitting medium and compressed to pressures ranging from 32 to 130 GPa (Figure 5.3.1-1) and heated using a double-sided laser setup at temperatures between 2200 and 3100 K over relatively long time periods ranging from 20 to 100 min. For more details see *Supplementary Materials*.

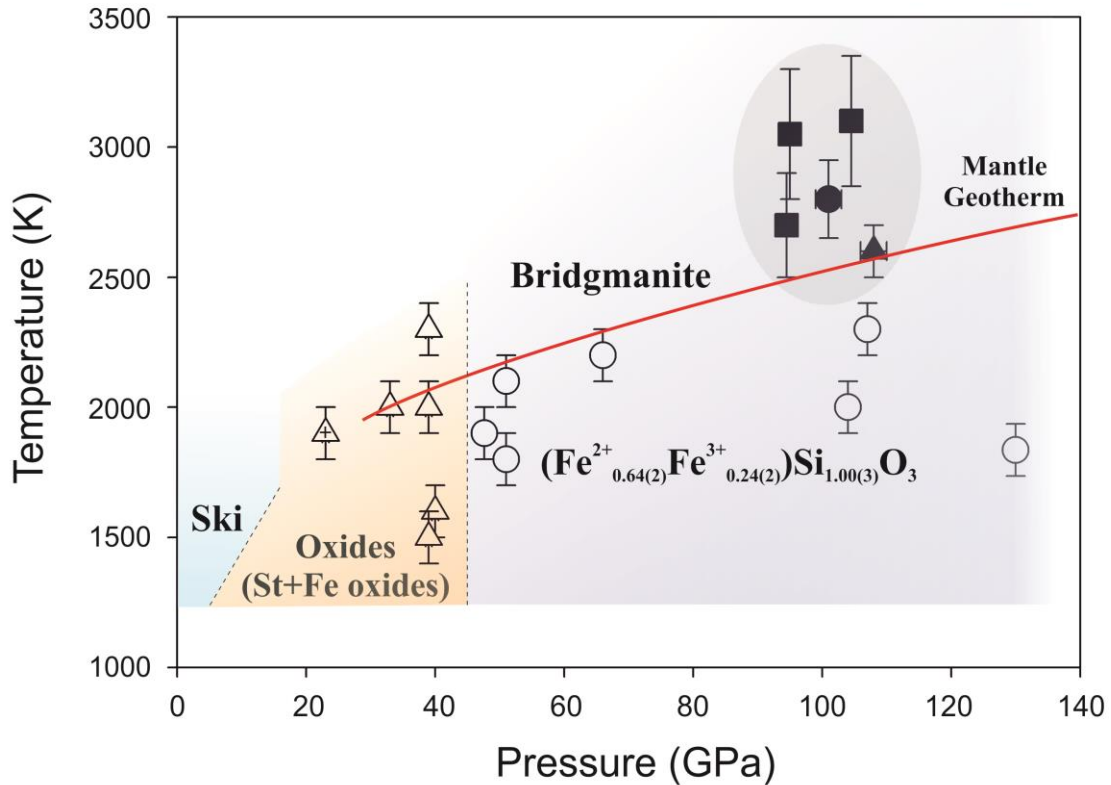


**Figure 5.3.1-1** Stability fields of skiaigite garnet, oxides and bridgmanite (Ski – skiaigite-majorite garnet  $\text{Fe}^{2+}_3(\text{Fe}^{2+}_{0.234(2)}\text{Fe}^{3+}_{1.532(1)}\text{Si}^{4+}_{0.234(2)})(\text{SiO}_4)_3$  (Ismailova et al. 2015); open triangle with cross – mixture of stishovite (St,  $\text{SiO}_2$ ),  $\text{Fe}_{1-x}\text{O}$ , and  $\text{Fe}_4\text{O}_5$ ; empty triangles – mixture of stishovite and  $\text{Fe}_4\text{O}_5$ ; solid symbols corresponds to conditions of the experiments on  $\text{Mg}_{0.86}\text{Fe}_{0.14}\text{Al}_{0.04}\text{Si}_{0.96}\text{O}_3$  (FE14, squares),  $\text{Mg}_{0.83}\text{Fe}_{0.17}\text{Al}_{0.06}\text{Si}_{0.94}\text{O}_3$  (FE17, triangle), and  $\text{Mg}_{0.60}\text{Fe}_{0.40}\text{Si}_{0.63}\text{Al}_{0.37}\text{O}_3$  (FE40, circle). Open circles shows conditions at which pure iron bridgmanite ( $\text{Fe}^{2+}_{0.64(2)}\text{Fe}^{3+}_{0.24(2)}\text{Si}_{1.00(3)}\text{O}_3$ ) was synthesized. Dark-grey area marks pressure-temperature conditions at which experiments on Fe,Al-bearing silicate perovskites were conducted. Red solid curve - expected lower mantle geotherm (Katsura et al. 2010). The error bars indicate experimental uncertainty in pressure and temperature.

The only observed changes upon laser heating for all investigated samples were shifts in the positions of reflections due to variations in temperature and pressure

(*Supplementary Information*, Figure S 5.3.2-1). Detailed inspection of diffraction patterns (Figure 5.3.1-2, *Supplementary materials*, Figure S 5.3.2-1) did not reveal the appearance of any non-identified reflections during or after heating. When pressure remained the same before and after laser heating (see, for example, *Supplementary Materials*, Table S 5.3.2-1), the lattice parameters of bridgmanite also remained the same within experimental uncertainty, suggesting that the integrity of the material was not affected by prolonged laser heating. The data sets collected for temperature-quenched samples are of sufficient quality to perform accurate structure refinements including the determination of the occupancy of iron at the two different distinct crystallographic sites of the perovskite-type structure (see Refs. (Glazyrin et al. 2014 ; E.Bykova 2015) for methodological details). Perovskite-structured orthorhombic bridgmanite (space group *Pbmn*, #62) has two cation positions (*Supplementary Materials*, Figure S 5.3.2-3) – one coordinated by a distorted bi-capped prism (“A”-site) and one octahedrally coordinated (“B-site”). We found that in accordance with previous observations (Glazyrin et al. 2014) and within the uncertainties of our method (about 5% of a total iron content), there is no evidence for redistribution of Fe between the two crystallographic sites and there are no changes in the chemical composition (*Supplementary Materials*, Table S 5.3.2-1).

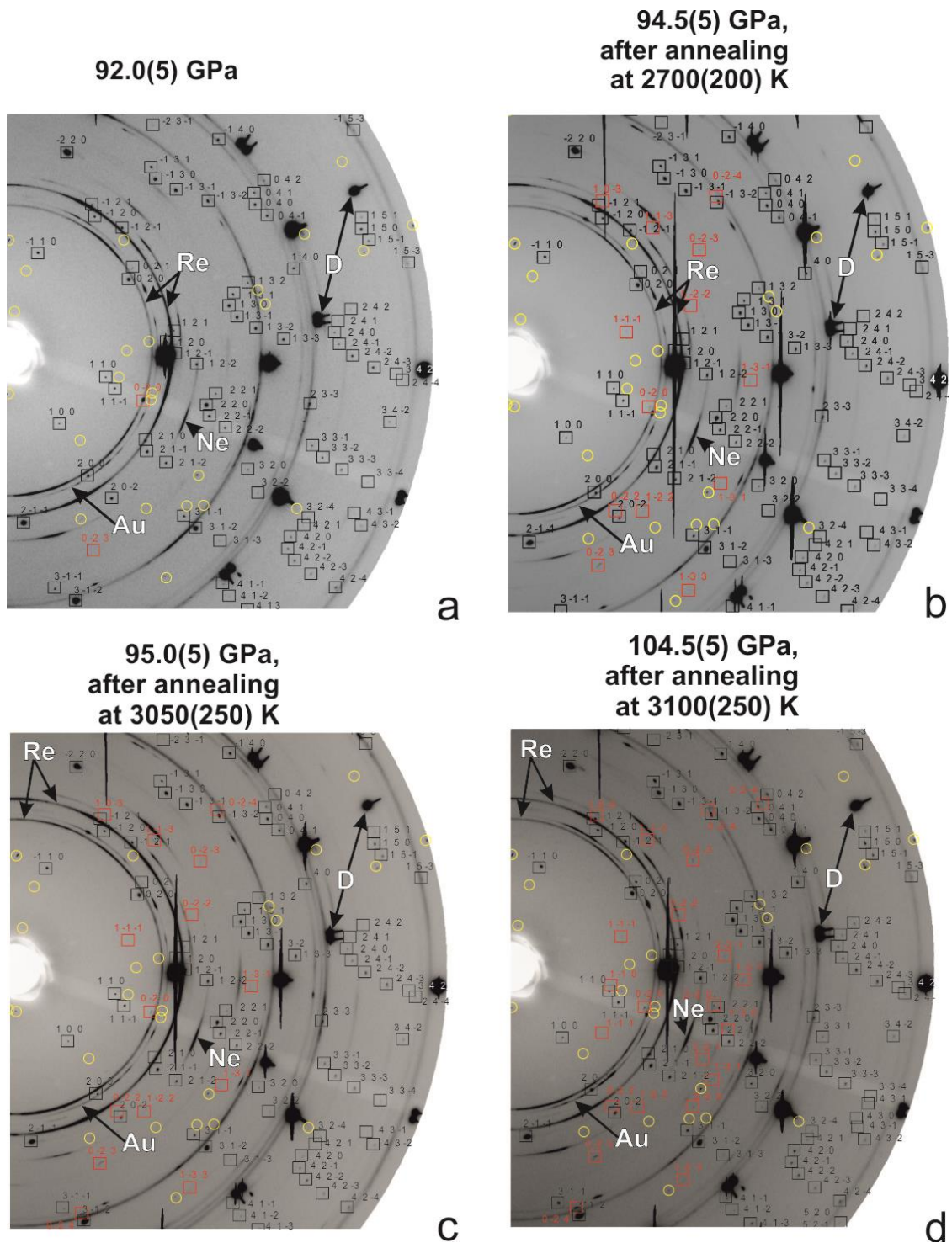


**Figure 5.3.1-2** Examples of parts of the 2D wide-scans of X-ray diffraction images of bridgmanite  $\text{Mg}_{0.86}\text{Fe}_{0.14}\text{Al}_{0.04}\text{Si}_{0.96}\text{O}_3$  collected before (a) and after (b-d) laser heating at different pressures and temperatures. Indexes are given for

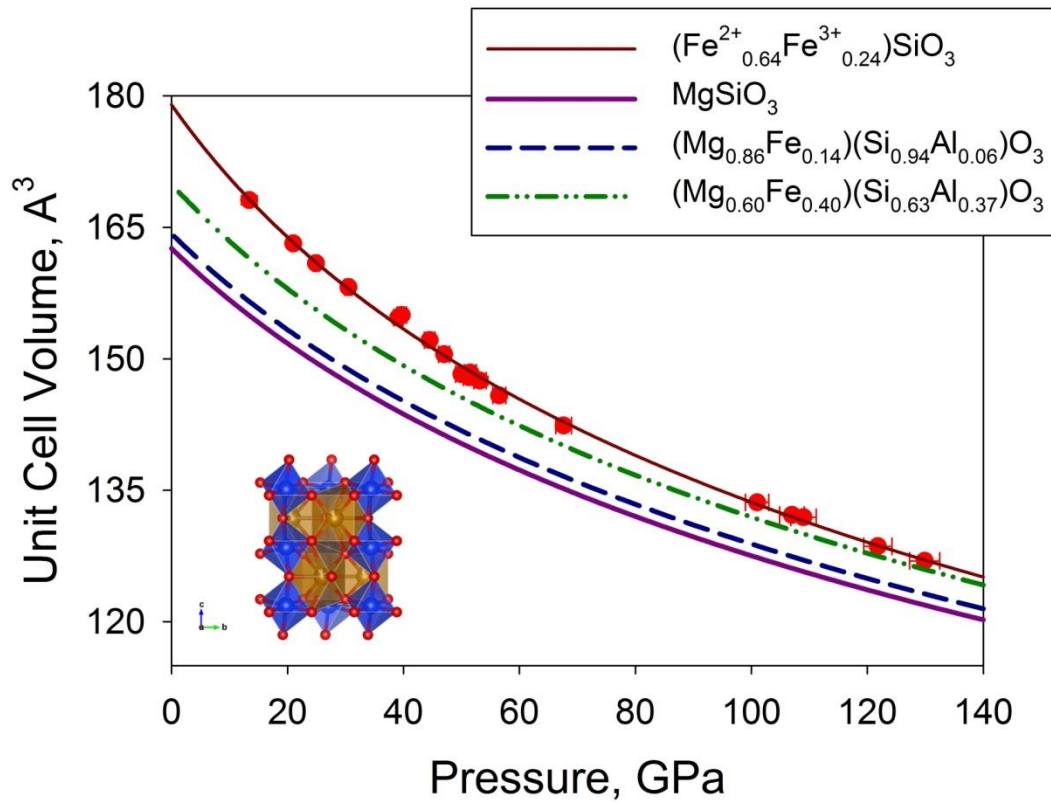
**bridgmanite reflections (underlined by boxes). The only observed changes in diffraction patterns upon heating are due to development of additional domains of the same phase (marked in red). Large black spots are due to diamond reflections. Diffraction rings of Ne (pressure transmitting medium), Re (gasket), and Au are also marked. Data were collected at IDD-13 at APS. Yellow circles indicate bad pixels of the detector. (Full high resolution images are given also in Supplementary Materials).**

The occurrence of an iron-rich H-phase at high pressures and temperatures may be related to the instability of pure iron bridgmanite (Zhang et al. 2014). Indeed, the amount of the  $\text{Fe}^{2+}\text{SiO}_3$  component that can be accommodated by Mg,Fe bridgmanite ranges from about 12 mol% at 26 GPa (Fei et al. 1996) to 50-74 mol% at ~85 GPa (Mao et al. 1997; Tange et al. 2009; Dorfman et al. 2013). At pressures from about 20 GPa to over 115 GPa, pure  $\text{FeSiO}_3$  was reported to disproportionate into FeO and  $\text{SiO}_2$  (Ming, L., Bassett 1975; Fujino et al. 2009). Ferrous iron endmember bridgmanite has never been synthesized so far and the solubility limit of the Fe-bearing component in perovskite-structured silicate remains unknown. However it is now widely accepted (Andraut 2001; Murakami et al. 2012; Glazyrin et al. 2014; Kuppenko et al. 2014, 2015) that bridgmanite relevant to the lower mantle contains both ferrous and ferric iron. Thus, the relevant question is whether pure  $\text{Fe}^{2+}, \text{Fe}^{3+}$ -bridgmanite exists or not.

We used synthetic skiaigite-majorite garnet as starting material for experiments to study the high-pressure high-temperature behavior of Mg,Al-free  $\text{Fe}^{3+}$ -bearing silicate with composition  $\text{Fe}^{2+}_3(\text{Fe}^{2+}_{0.234(2)}\text{Fe}^{3+}_{1.532(1)}\text{Si}^{4+}_{0.234(2)})(\text{SiO}_4)_3$  as determined from single crystal diffraction and Mössbauer spectroscopy data (Ismailova et al. 2015). Our experiments using the multi-anvil apparatus up to 23 GPa and 1900 K demonstrate that above 12.5 GPa and 1700 K, skiaigite-majorite garnet decomposes to  $\text{SiO}_2$  and Fe oxides (Figure S 5.3.2-4). Laser heating of skiaigite-majorite garnet in the DAC up to ~40 GPa and 1500 to 2300 K resulted in decomposition to stishovite ( $\text{SiO}_2$ ) and  $\text{Fe}_4\text{O}_5$  (Lavina et al. 2011) (Figure S 5.3.2-5). Remarkably, in some runs iron oxide crystallized in the form of single crystals (or polycrystalline domains) which gave diffraction data of sufficient quality for an accurate structure refinement of  $\text{Fe}_4\text{O}_5$

(Figure S 5.3.2-6 Table S 5.3.2-4). Upon heating at pressures above ~45 GPa we observed different sequences of transformations. For example, at 51(1) GPa and 1800(100) K skiaigite-majorite garnet decomposes to stishovite, high-pressure orthorhombic  $h$ -Fe<sub>3</sub>O<sub>4</sub> (L. S. Dubrovinsky et al. 2003), and one additional phase (Figure S 5.3.2-5). At higher temperatures (2100(100) K, for example, Figure S 5.3.2-5) diffraction lines of stishovite are absent, the intensity of reflections of  $h$ -Fe<sub>3</sub>O<sub>4</sub> decreases, and the diffraction pattern is dominated by lines of the additional phase that can be easily indexed as orthorhombic. Analysis of single crystal diffraction data allows unambiguous identification of this phase to be GdFeO<sub>3</sub>-type perovskite structure (Figure S 5.3.2-3). The same phase was synthesized by heating skiaigite-majorite garnet at different pressures up to over 100 GPa (Figure 5.3.1-1). Once synthesized, the phase maintains its structure on compression up to ~125 GPa and decompression down to at least 13 GPa. Accurate structure refinements of samples produced at different pressures and temperatures give highly consistent results regarding the composition of the material. Based on the results of six different experiments it can be expressed as (Fe<sup>2+</sup><sub>0.64(2)</sub>Fe<sup>3+</sup><sub>0.24(2)</sub>)Si<sub>1.00(3)</sub>O<sub>3</sub>.). Thus, we synthesized pure Fe-bridgmanite and demonstrated that above ~50 GPa, the presence of Fe<sup>3+</sup> stabilizes silicate perovskite relative to mixed oxides. The crystal chemistry of ferric iron-bearing Fe-bridgmanite is remarkable (Figure 5.3.1-3). First, we observe that all iron is located in the A-site and within the accuracy of determination of the occupancies of structural positions (better than 5%) there is no iron in the octahedra (B-site). This conclusion is robust because X-ray scattering factors of silicon and iron are very different and is in agreement with recent studies on bridgmanites of different compositions (Dorfman et al. 2012; Glazyrin et al. 2014; Kuppenko et al. 2014). Second, it is obvious that the material synthesized between 50 and 100 GPa contains a significant amount of vacancies (about 12%) at the A-site according to the substitution scheme  $3\text{Fe}^{2+} \rightarrow 2\text{Fe}^{3+} + \text{Vacancy}$ . Formation of materials with vacancies at high pressure is not unprecedented, particularly among Fe<sup>3+</sup>-bearing oxides (Bykova et al. 2016), but have not been expected for silicate perovskites (Brodholt 2000; Xu et al. 2015).

The dependence of polyhedral volumes on the unit cell volume (Figure 5.3.1-3) for Fe-bridgmanite is the same as for pure magnesium- and iron-aluminum-bearing bridgmanites. It confirms that the large iron cation does not enter the *B*-site because incorporation of any appreciable amount of iron cations in the octahedral site in Fe-bearing bridgmanite should significantly affect its compressibility.



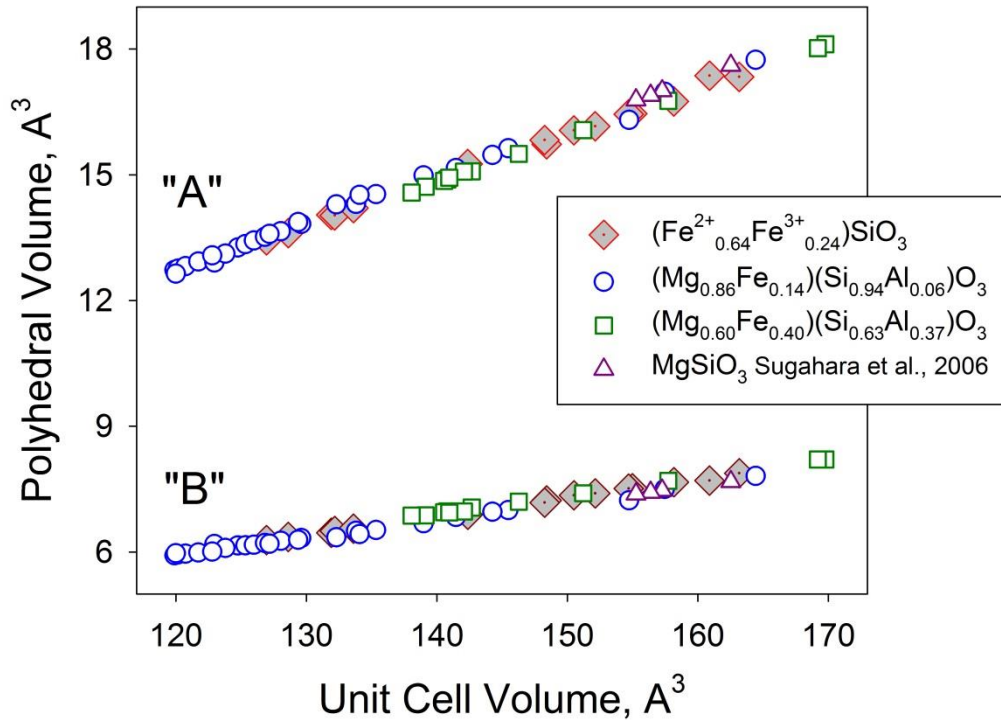


**Figure 5.3.1-3 Compressibility of  $(\text{Fe}^{2+}_{0.64(2)}\text{Fe}^{3+}_{0.24(2)})\text{Si}_{1.00(3)}\text{O}_3$  silicate perovskite.** (a) Unit cell volumes of single crystals of pure iron bridgmanite synthesized at different pressures were measured on compression and/or decompression (red dots with error bars). The data are fitted (solid dark-red line) with a Birch-Murnaghan equation of state giving bulk modulus  $K_{300}=190(4)$  GPa and unit cell volume at ambient conditions  $V_0=178.98(6)$  Å<sup>3</sup> ( $K'=4$ ). For comparison compressional curves of pure  $\text{MgSiO}_3$  (Sugahara et al. 2006; Ballaran et al. 2012), (solid purple line),  $(\text{Mg}_{0.6},\text{Fe}_{0.4})(\text{Si}_{0.63}\text{Al}_{0.37})\text{SiO}_3$  (Dorfman and Duffy 2014; Glazyrin et al. 2014) (dotted-dashed green line), and  $(\text{Mg}_{0.86},\text{Fe}_{0.14})(\text{Si}_{0.94}\text{Al}_{0.06})\text{SiO}_3$  (dashed dark-blue line) are shown (see also Table S3). Insert shows model of perovskite-structured orthorhombic (space group *Pbmn*, #62) bridgmanite with two distinct cation coordinations – distorted bi-capped prisms (“A”-site, brown) and octahedra (“B-site”, blue). (b) Dependence of A- and B- polyhedral volumes as a function of unit cell volume for bridgmanites with different compositions (see text for more details and references).

The effect of pressure on the lattice parameters of Fe<sup>3+</sup>-bearing Fe-bridgmanite is very different from the variation observed for any other silicate perovskites (see (Ballaran et al. 2012; Dorfman et al. 2012; Glazyrin et al. 2014; Kuppenko et al. 2015) and references therein) in that the *a*- and *b*-axes are much more compressible (Figure S 5.3.2-7). Thus, vacancies on the A-site lead to significant softening of the material; it has a bulk modulus  $K_{300}=190(4)$  GPa ( $K'=4$ ,  $V_0=178.98(6)$  Å<sup>3</sup>/unit cell, Figure 5.3.1-3, Table S 5.3.2-3), which is drastically lower than values known for other Fe- or/and Al-rich bridgmanites (Saikia et al. 2009; Ballaran et al. 2012; Dorfman et al. 2012, 2013; Glazyrin et al. 2014) (Figure S 5.3.2-8).

The elastic properties of Fe,Al-bearing silicate perovskites reported in the literature are highly controversial, especially in cases where samples were synthesized *in situ* in laser-heated DACs (for discussion, see particularly (Andrault 2001; Saikia et al. 2009; Ballaran et al. 2012; Dorfman et al. 2012, 2013; Glazyrin et al. 2014)). The large effect of Fe<sup>3+</sup> and vacancies on the bulk modulus of bridgmanite that we observed suggests that accurate determination and comparison of the compressibility of silicate perovskites may be reliable only if the composition (including Fe<sup>3+</sup>/ΣFe) and the structure of the material are known in detail.

A recent precise study of iron-bearing perovskite (Xu et al. 2015) demonstrates that in the case of the charge-substitution mechanism, the density and bulk modulus of bridgmanite vary linearly with the Fe content. Using equations reported in (Dorfman and Duffy 2014), at a representative mid-mantle depth of 1850 km (80 GPa) the density and the bulk modulus of bridgmanite with composition Fe<sub>0.88</sub>SiO<sub>3</sub> is estimated to be  $\rho_{80}=6.171(4)$  g/cm<sup>3</sup> and  $K_{80}=556(24)$  GPa. Using our data we obtain  $\rho_{80}=5.99(1)$  g/cm<sup>3</sup> and  $K_{80}=480(15)$  GPa, and bulk velocity heterogeneity parameter,  $\partial \ln V_B / \partial X_{Fe}$ , 0.16 (vs  $\sim 0.10$  in (Dorfman and Duffy 2014; Glazyrin et al. 2014)). Consequently for oxidized parts of the lower mantle (subducted slabs, for example) and for relevant chemical compositions, the variation of Fe<sup>3+</sup>/ΣFe can lead to significant changes in the bulk sound velocity of brigmanite (exceeding 2%), clearly demonstrating the importance of iron oxidation state for interpreting seismic tomography data (Glazyrin et al. 2014).

## Acknowledgments

We thank I. Kantor for help with laser-heating and we acknowledge the European Synchrotron Radiation Facility for provision of synchrotron radiation facilities. Natalia Dubrovinskaia and Leonid Dubrovinsky thank Deutsche Forschungsgemeinschaft (DFG) and the Federal Ministry of Education and Research (BMBF), Germany, for financial support. Part of this study was performed at GeoSoilEnviroCARS (Sector 13), Advanced Photon Source (APS), Argonne National Laboratory. GeoSoilEnviroCARS is supported by the National Science Foundation - Earth Sciences (EAR-1128799) and Department of Energy- GeoSciences (DE-FG02-94ER14466). This research used resources of the Advanced Photon Source, a U.S. Department of Energy (DOE) Office of Science User Facility operated for the DOE Office of Science by Argonne National Laboratory under Contract No. DE-AC02-06CH11357. We thank S. Tkachev for the technical support with the gas-loading at APS.

### 5.3.2 Supplementary materials

#### Materials

The material used in this study consists of single crystals of bridgmanite with different compositions:  $\text{Mg}_{0.83}\text{Fe}_{0.17}\text{Al}_{0.06}\text{Si}_{0.94}\text{O}_3$  (Fe17),  $\text{Mg}_{0.86}\text{Fe}_{0.14}\text{Al}_{0.04}\text{Si}_{0.96}\text{O}_3$  (Fe14),  $\text{Mg}_{0.60}\text{Fe}_{0.40}\text{Si}_{0.63}\text{Al}_{0.37}\text{O}_3$  (Fe40) and skiaigite-majorite garnet ( $\text{Fe}^{2+}_{0.64(2)}\text{Fe}^{3+}_{0.24(2)}\text{Si}_{1.00(3)}\text{O}_3$ ).

The details of samples FE17, FE14, Fe40 were described elsewhere (Dubrovinsky et al. 2010; Glazyrin et al. 2014; Kuppenko et al. 2014).

Mg,Al-free Fe-bridgmanite was synthesized from skiaigite-majorite garnet from the same batch that was used in a previous study (Ismailova et al. 2015).

#### Multi-anvil experiments

Multi-anvil (MA) experiments to study the stability of skiaigite were performed at Bayerisches Geoinstitut (BGI), Bayreuth at pressures up to 23 GPa and temperatures up to 1800 K. The starting mixture with the skiaigite composition ( $\text{Fe}_3\text{Fe}_2\text{Si}_3\text{O}_{12}$ ) was prepared from pure oxides  $\text{Fe}_{0.94}\text{O}$ ,  $\text{Fe}_2\text{O}_3$  and  $\text{SiO}_2$ . The mixtures were loaded into a

Re capsule with 1mm diameter and 1.8 mm long and heated for 30 min. A  $W_{97}Re_3$ - $W_{75}Re_{25}$  thermocouple was used to monitor the temperature.

According to X-ray powder diffraction the synthesized sample consists of mixtures of oxides: stishovite,  $Fe_{1-x}O$  and  $Fe_4O_5$  (Table S 5.3.2-4).

### **Microprobe**

Chemical compositions of the samples recovered from MA experiments were characterized using wavelength-dispersive X-ray (WDX) microprobe analysis (JEOL JXA-8200; focused beam; accelerating voltage of 15 keV and beam current of 15 nA). Metallic Fe and quartz were used as standards for Fe and Si, respectively, with atomic number effects, absorption, and fluorescence (ZAF) correction.

### **Diamond Anvil Cell experiments**

The crystals of bridgmanite with different compositions in size from  $\sim 10 \times 10 \times 5 \mu m^3$  to  $\sim 20 \times 20 \times 7 \mu m^3$  were selected and tested before loading into a diamond anvil cell (DAC) using an *in house* high-brilliance rotating anode diffractometer (Dubrovinsky et al. 2006).

We used cylindrical-type DACs (Kantor et al. 2012) in all experiments. Boehler-Almax design diamonds with a culet size of 250  $\mu m$  were used for measurements less than 70 GPa. Above this pressure diamonds with 120  $\mu m$  culet size were used. The sample chamber was prepared by drilling a hole in the center of a 200  $\mu m$ -thick Re gasket pre-indented to 20  $\mu m$ . All DACs were loaded with Ne to achieve quasi-hydrostatic conditions and as a pressure standard. For pressure measurements below 15 GPa small ruby chips were loaded.

### **Synchrotron X-ray diffraction**

Single crystal X-ray diffraction experiments were performed at the Advanced Photon Source (APS), Argonne National Laboratory at beamline 13 ID-D (GSECARS), Argonne, USA; at the European Synchrotron Radiation Facility (ESRF), Grenoble, France at the ID09A and ID27 beamlines and at the Deutsches Elektronen-Synchrotron (DESY) at PETRA III, Hamburg, Germany at the extreme conditions beamline P02.2.

High pressure and high temperature experiments at 13 ID-D were performed using X-rays with a wavelength 0.31 Å. The beam was focused with a Kirkpatrick-Baez double mirror system to dimensions of 10 x 10 μm<sup>2</sup>. Diffraction patterns were collected using a MarCCD detector and the position of the detector was calibrated using a LaB<sub>6</sub> standard. The sample was heated *in situ* using a Nd:YAG double-sided laser heating system and temperatures were measured from both sides by spectroradiometry (Prakapenka et al. 2008).

At ESRF on beamline ID09A we used a Mar555 flat panel detector and a X-ray wavelength of 0.415 Å with the beam spot size ~10x10 μm<sup>2</sup>, while on beamline ID27 the parameters were as follows: λ=0.37 Å, beam size 3x3 μm<sup>2</sup>, Perkin Elmer flat panel detector. At the Extreme conditions Beamline P02.2 at PETRA III the X-ray wavelength we used the wavelength λ= 0.2903 Å and Perkin Elmer detector, the beam size was 3x8 μm<sup>2</sup>. The positions of the detectors were calibrated using a Si standard.

Single crystal diffraction data were collected in two modes – by continuous rotation of the cell around the omega axis (“wide scans”) from -20 to +20° for *in situ* high-pressure high-temperature data acquisition and from -38 to +38° (“step scans”) for temperature-quenched sample (i.e. without laser-heating set up) by narrow 0.5° omega scanning. Pressure was determined using the Ne EOS (Fei et al. 2007). In some experiments a small (linear dimensions less than 5 μm) piece of gold was loaded at the edge of the pressure chamber in order to allow an accurate alignment of the cell with respect to the goniometer rotational axis.

The 2D diffraction images were first analysed using Dioptas software (Prescher and Prakapenka 2015). Data processing (peak intensity integration, background evaluation, cell parameters, space group determination, and absorption correction) was performed with the CrysAlis Pro 171.36.28 (Oxford Diffraction 2006) software with implemented SCALE3 ABSPACK scaling algorithm. Structures were solved by the direct method using the SHELXS (Sheldrick 2008) software implemented in the X-seed package (Barbour 2001). Structure refinement of integrated intensities was performed using SHELXL. Full-profile refinement of powder patterns was conducted using GSAS

software with a graphical interface EXPFGUI (Brian H. Toby 2001). Polyhedral volumes were calculated in VESTA software (Momma and Izumi 2011).

### Supplementary Figures

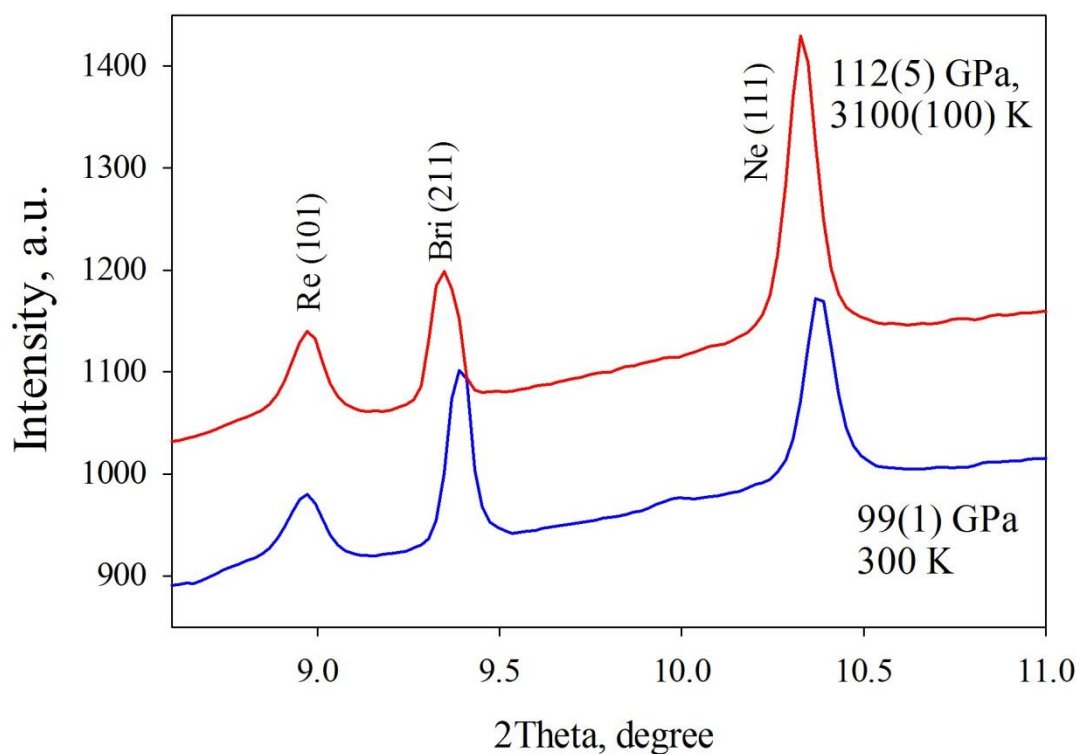
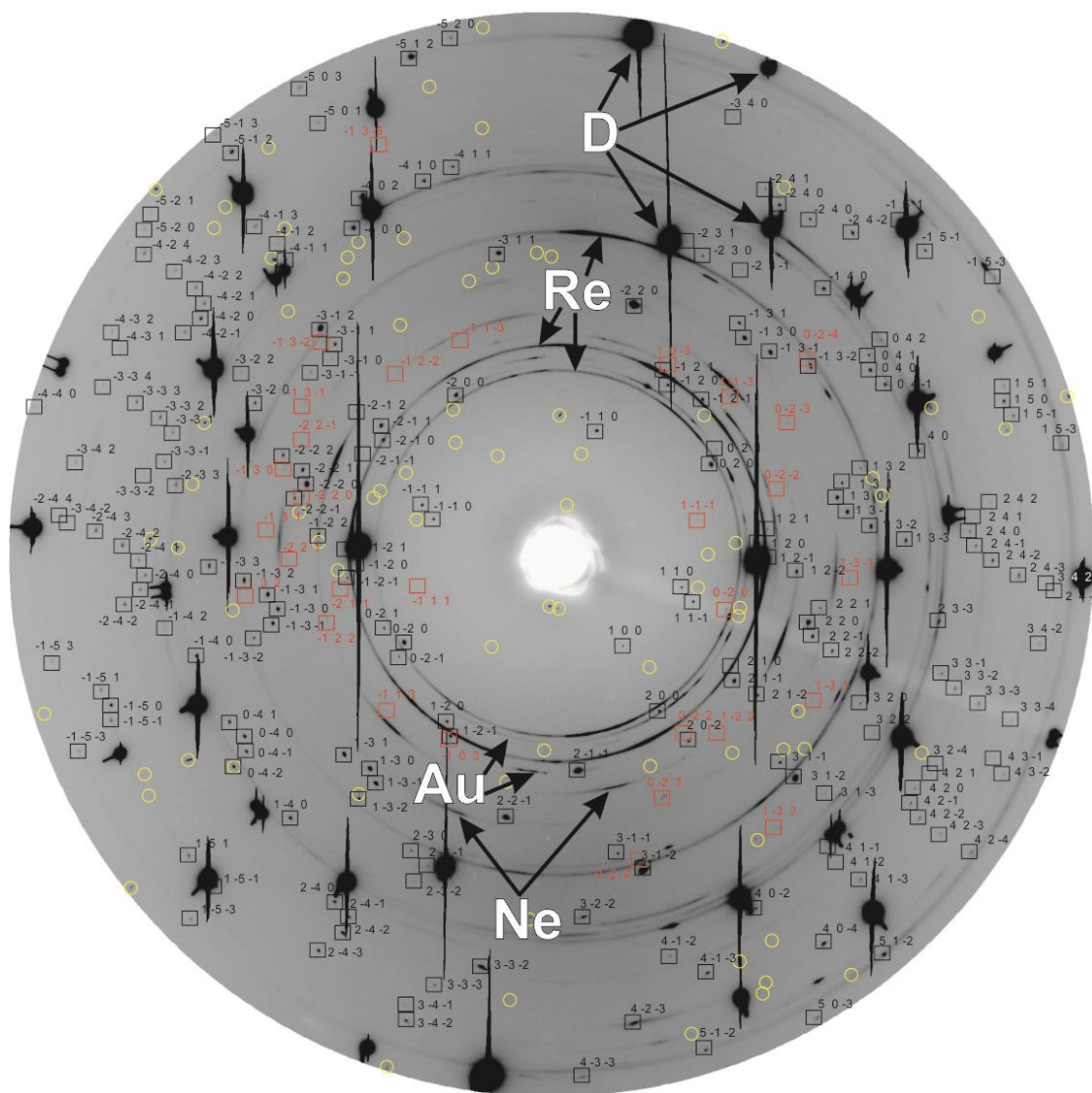


**Figure S 5.3.2-1** Parts of the integrated diffraction images of bridgmanite  $\text{Mg}_{0.86}\text{Fe}_{0.14}\text{Al}_{0.04}\text{Si}_{0.96}\text{O}_3$  (FE14) collected before (lower curve) and during (upper curve) laser heating. While the position of the Re (gasket) diffraction line not affected by heating, diffraction lines of bridgmanite and Ne (pressure transmitting and thermal insulating medium) show pronounced shifts; upon heating pressure increases from 99(1) to 112(5) GPa. Data collected at IDD-13 (APS, USA), X-ray wavelength 0.31 Å.



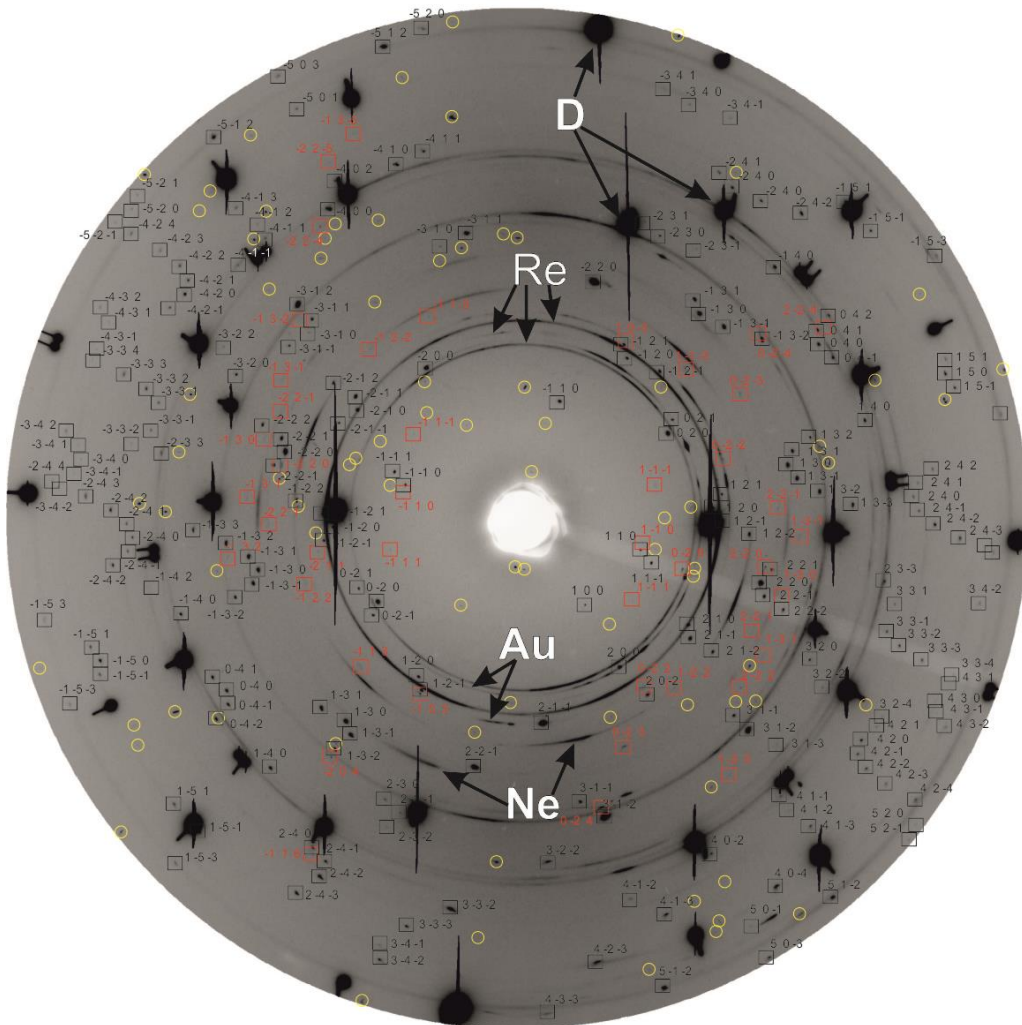
**94.5(5) GPa,  
after annealing  
at 2700(200) K**



b)



104.5(5) GPa,  
after annealing  
at 3100(250) K



d)

Figure S 5.3.2-2 Examples of parts of the 2D wide-scans of X-ray diffraction images of bridgmanite  $\text{Mg}_{0.86}\text{Fe}_{0.14}\text{Al}_{0.04}\text{Si}_{0.96}\text{O}_3$  collected before (a) and after (b-d) laser heating at different pressures and temperatures. Indexes are given for bridgmanite reflections (underlined by boxes). The only observed changes in diffraction patterns upon heating are due to development of additional domains of the same phase (marked in red). Large black spots are due to diamond

reflections. Diffraction rings of Ne (pressure transmitting medium), Re (gasket), and Au are also marked. Data were collected at IDD-13 at APS. Yellow circles indicate bad pixels of the detector.

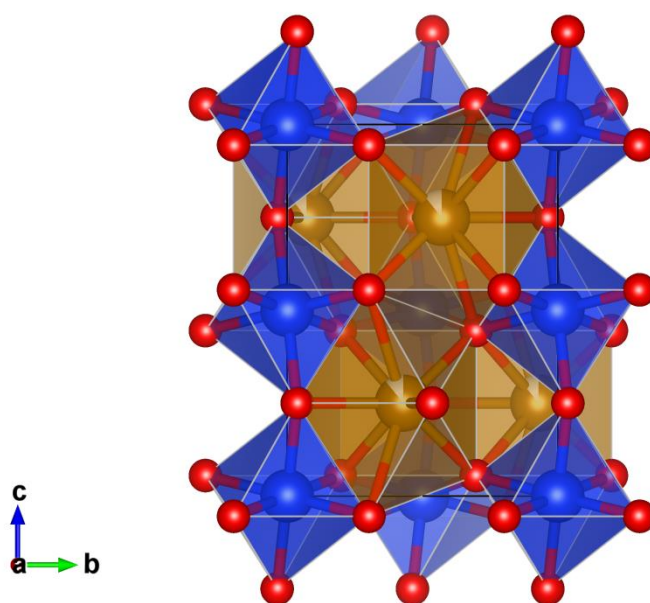
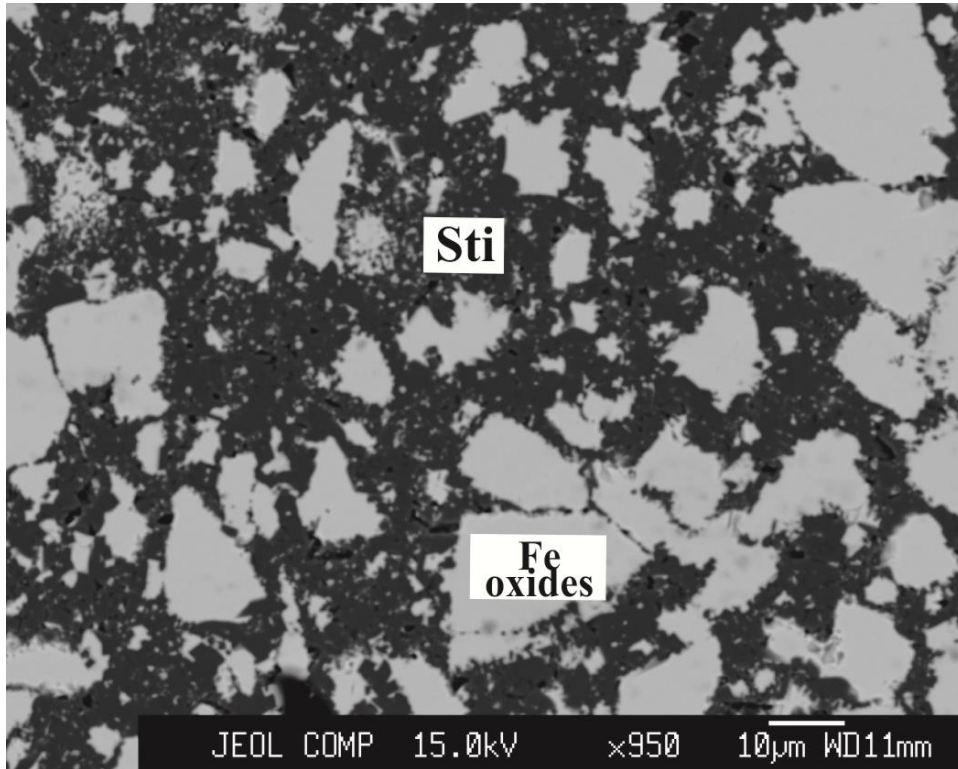


Figure S 5.3.2-3 Representative polyhedral structural model of orthorhombic bridgmanite. The bridgmanite structure (space group  $Pbmn$ , #62) has two cation positions – a distorted bi-capped prism (“A”-site, brown) and octahedra (“B-site”, blue). For the case of  $(\text{Fe}^{2+}_{0.64(2)}\text{Fe}^{3+}_{0.24(2)})\text{Si}_{1.00(3)}\text{O}_3$  silicate perovskite (synthesized, for example, at 67 GPa and 2200(100)K; orthorhombic  $Pbmn$ ,  $a=4.5516(3)$  Å,  $b=4.7753(15)$  Å,  $c=6.5497(4)$  Å,  $V=142.36(5)$  Å<sup>3</sup>) vacancies on the A-site are indicated in white.



**Figure S 5.3.2-4 BSE image of skiaite starting composition at 23 GPa and 1600 °C (run S6151). Skiaite-majorite garnet decomposes to oxides: dark gray – SiO<sub>2</sub> (stishovite), light gray – Fe oxides (Fe<sub>1-x</sub>O and Fe<sub>4</sub>O<sub>5</sub>).**

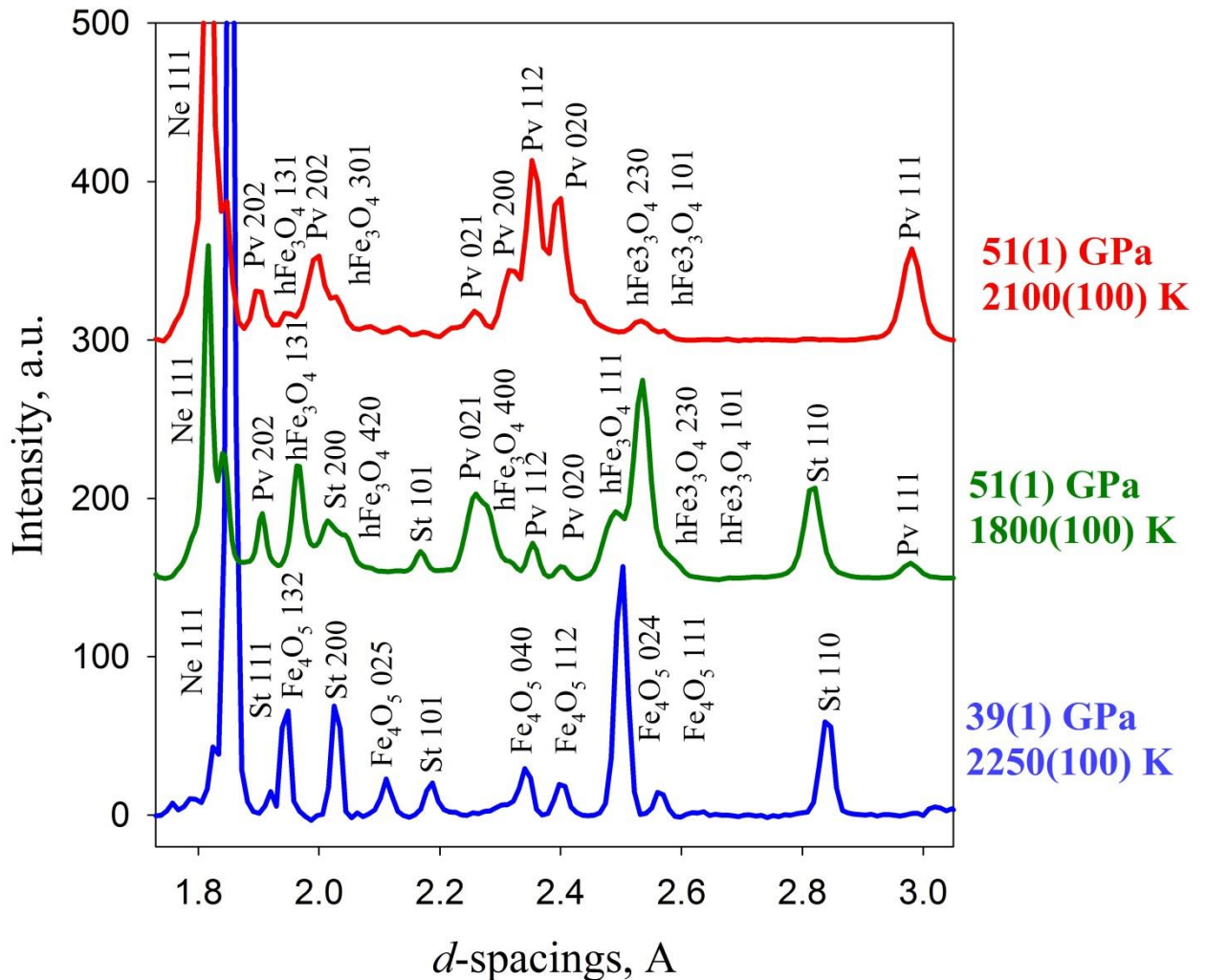
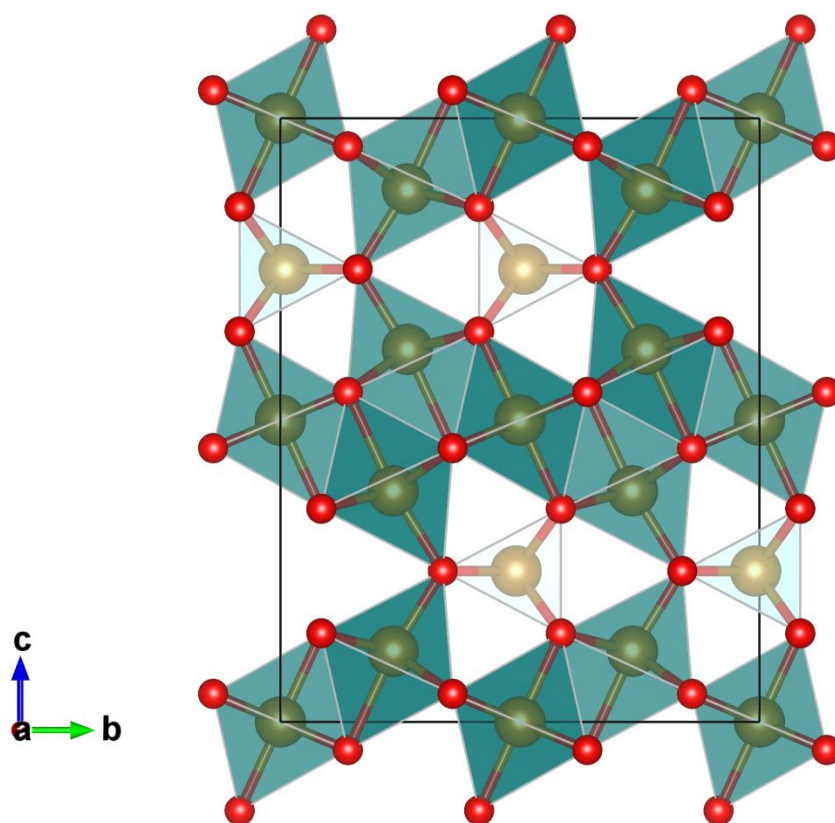


Figure S 5.3.2-5 Typical powder X-ray diffraction patterns of skiagite-majorite garnet that was laser heated at different pressures and temperatures (St – stishovite, hFe<sub>3</sub>O<sub>4</sub> – orthorhombic CaTi<sub>2</sub>O<sub>4</sub>-type Fe<sub>3</sub>O<sub>4</sub>, Pv- perovskite-structured phase). Pressure was determined using Ne lattice parameters (see <http://kantor.50webs.com/diffraction.html>).



**Figure S 5.3.2-6** Crystal structure of Fe<sub>4</sub>O<sub>5</sub> obtained as the product of decomposition of skiaegite-majorite garnet in a laser-heated DAC at 39(1) GPa and 2250(100) K (see Table S4 for crystallographic data).

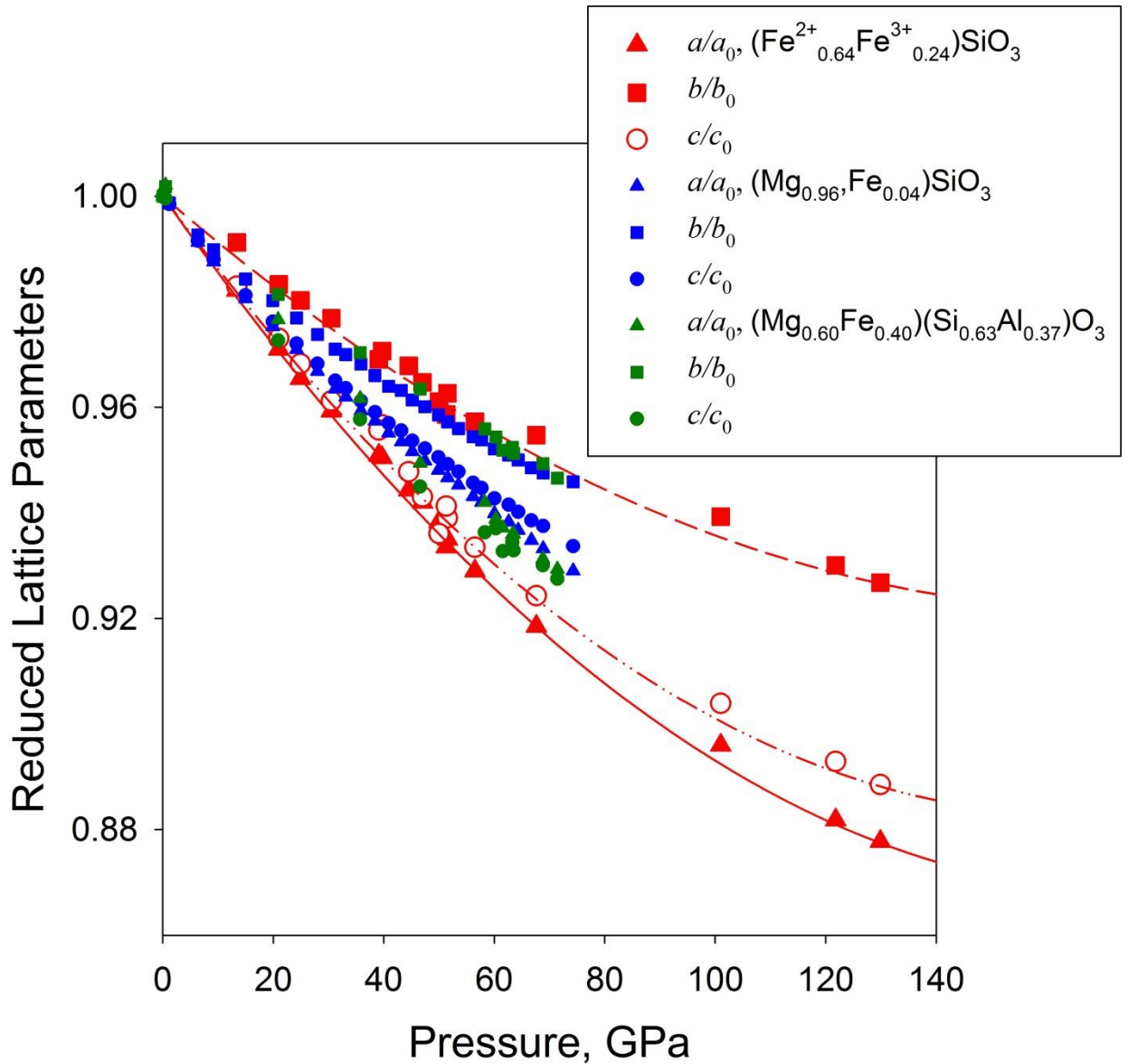


Figure S 5.3.2-7 Variation with pressure of the normalized unit-cell parameters for three silicate perovskites – Fe-bridgmanite (this study),  $(\text{Mg}_{0.96}, \text{Fe}_{0.04})\text{SiO}_3$  (Ballaran et al. 2012), and  $\text{Mg}_{0.60}\text{Fe}_{0.40}\text{Si}_{0.63}\text{Al}_{0.37}\text{O}_3$  (Glazyrin et al. 2014). Note the clearly different behavior of the  $a$ - and  $b$ -axis of Fe-bridgmanite.

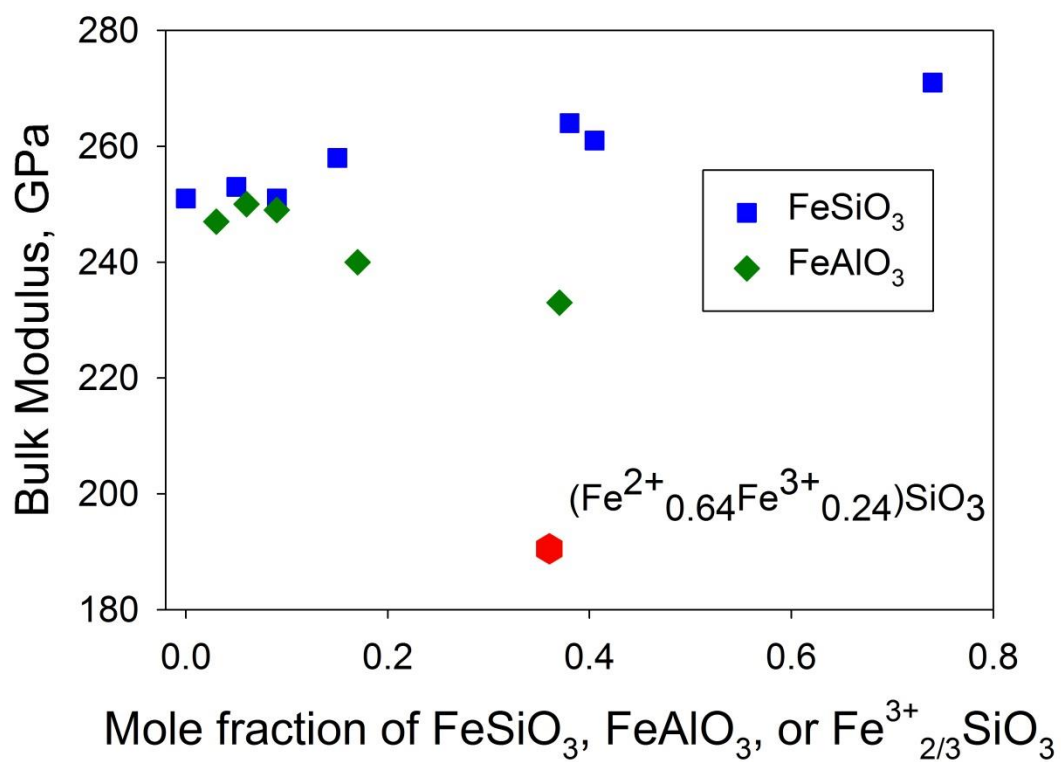


Figure S 5.3.2-8 Effect of Fe<sup>A</sup>SiO<sub>3</sub>, Fe<sup>A</sup>Al<sup>B</sup>O<sub>3</sub>, and Fe<sup>3+</sup><sub>2/3</sub>SiO<sub>3</sub> substitutions in bridgmanite on the bulk modulus (“A” and “B” denote structural positions)

## Supplementary tables

**Table S 5.3.2-1 Crystallographic data for Fe,Al silicate perovskite samples FE14, FE17, and FE40 at selected pressures before and after laser heating at different temperatures.**

Crystallographic data	FE14	FE14	FE14	FE14	FE40	FE17
P, T conditions of data acquisition	92.0(5) GPa	94.5(5) GPa, after 30 min heating at 2700(200) K	95.0(5) GPa after 40 min heating at 3050(250) K	104.5(5) GPa, after 30 min heating at 3100(250) K	101(2) GPa after 30 min heating at 2800(150) K	108(2) GPa after 40 min heating at 2600(100) K
Crystal system	Orthorhombic					
Space group	Pbnm					
$a$ (Å)	4.3955(7)	4.3944(7)	4.3931(6)	4.3615(5)	4.385(7)	4.3476(7)
$b$ (Å)	4.6336(6)	4.6313(6)	4.6313(6)	4.6103(5)	4.6758(12)	4.6014(8)
$c$ (Å)	6.397(4)	6.390(5)	6.395(5)	6.359(4)	6.378(2)	6.3398(7)
$V$ (Å <sup>3</sup> )	130.28(9)	130.04(11)	130.11(9)	127.86(8)	130.8(2)	126.83(3)

Z	4					
Fe occupancy in A position, %	14.4±1.1	14.4±1.1	13.4±1.1	13.7±1.1	38±1.2	17.1±1.2
Atomic coordinates(xyz)	0.5212(3)	0.5207(3)	0.5208(3)	0.5215(3)	-0.011(2)	-0.0218(4)
Mg/Fe	0.5722(3)	0.5721(3)	0.5718(4)	0.5731(4)	0.4237(8)	0.4247(6)
Si/Al	0.25	0.25	0.25	0.25	0.25	0.25
	0.5	0.5	0.5	0.5	0	0
	0	0	0	0	0	0
	0.5	0.5	0.5	0.5	0	0
O1	0.1148(8)	0.1139(8)	0.1145(9)	0.1155(8)	0.125(7)	0.1163(9)
	0.4661(7)	0.4660(6)	0.4667(7)	0.4665(7)	0.052(3)	0.0320(11)
	0.25	0.25	0.25	0.25	0.25	0.25

O2	0.1852(6) 0.1936(5) 0.5571(8)	0.1846(5) 0.1938(4) 0.5567(8)	0.1844(6) 0.1933(5) 0.5572(9)	0.1837(6) 0.1931(5) 0.5574(8)	0.188(4) 0.311(2) -0.0585(12)	0.1832(6) 0.3072(6) -0.0571(4)
<i>F</i> (000)	208	208	207	207	220	211
Theta range for data collection (°)	2.78 to 11.261	2.787 to 11.232	2.784 to 10.949	2.804 11.285	to 3.73 18.57	to 0.454 19.05
Completeness to <i>d</i> = 0.8 Å, %	61.9	61.1	61.8	61.1	31.8	45.4
Index ranges	-5 < <i>h</i> < 5	-2 < <i>h</i> < 3	-5 < <i>h</i> < 5			
	-5 < <i>k</i> < 5	-6 < <i>k</i> < 6	-5 < <i>k</i> < 4			
	-4 < <i>l</i> < 4	-8 < <i>l</i> < 7	-7 < <i>l</i> < 8			
No. of measured, independent, and observed [ <i>I</i> > 2σ( <i>I</i> )] reflections	252/91/82	242/88/81	245/89/82	243/88/83	176/104/94	221/124/124

$R_{\text{int}}$	0.0367	0.0307	0.0334	0.0331	0.0685	0.0621
No. of parameters/restraints	0/13	0/13	0/13	0/13	0/12	0/14
Goodness of fit on $F^2$	1.319	1.194	1.143	1.144	0.959	1.184
Final $R$ indices [ $I > 2\sigma(I)$ ] $R_1 / wR_2$	0.0373/0.0979	0.0415/0.1067	0.0443/0.1076	0.0415/0.1043	0.0638/0.1396	0.0629/0.1731
$R$ indices (all data) $R_1 / wR_2$	0.0563/0.1183	0.0471/0.1100	0.0506/0.1117	0.0428/0.1056	0.0730/0.1632	0.0629/0.1731
Largest diff. peak /hole ( $e / \text{\AA}^3$ )	0.998/-0.778	0.600/-0.504	0.594/-0.672	0.603/-0.590	0.442/-0.648	0.884/-0.961

**Table S 5.3.2-2 Crystallographic data for (Fe<sup>2+</sup><sub>0.64(2)</sub>Fe<sup>3+</sup><sub>0.24(2)</sub>)Si<sub>1.00(3)</sub>O<sub>3</sub> bridgmanite at selected pressures.**

P, T conditions of XRD experiment	44.0(5) GPa	67.0(5) GPa 2200(100) K	107.0(5) GPa 2300(100) K	129.0(5) GPa 1835(100) K
Crystal system	Orthorhombic			
Space group	Pbnm			
<i>a</i> (Å)	4.6332(17)	4.5516(3)	4.4364(6)	4.3494(15)
<i>b</i> (Å)	4.815(5)	4.7753(15)	4.7079(10)	4.6354(14)
<i>c</i> (Å)	6.654(3)	6.5497(4)	6.328(5)	6.296(6)
<i>V</i> (Å <sup>3</sup> )	148.44(18)	142.36(5)	132.17(11)	126.93(13)
<i>Z</i>	4			
Fe occupancy in A position, %	85.3±1.7	88.7±1.4	84.3±1.1	82.1±1.3

Atomic coordinates(xyz)	Fe	Fe	Fe	Fe
Fe	-0.0147(4)	-0.0196(3)	-0.0250(4)	-0.0280(5)
Si	0.4366(8)	0.4295(8)	0.4224(4)	0.4182(5)
O1	0.25	0.25	0.25	0.25
O2	Si	Si	Si	Si
	0	0	0	0
	0	0	0	0
	0	0	0	0
	O1	O1	O1	O1
	0.110(2)	0.1125(15)	0.1198(18)	0.123(2)
	0.041(3)	0.038(3)	0.0356(16)	0.0375(15)
	0.25	0.25	0.25	0.25
	O2	O2	O2	O2
	0.1861(14)	0.1853(8)	0.1813(13)	0.1797(18)

	0.314(2) -0.0537(10)	0.302(2) -0.0546(5)	0.3090(10) -0.0559(15)	0.3089(11) -0.0567(19)
A-bicapped prism $V_0$ , Å <sup>3</sup>	15.7297	15.258	14.0290	13.4375
B-octahedra, $V_0$ , Å <sup>3</sup>	7.2301	6.888	6.5024	6.2801
$F(000)$	268	268	268	268
Theta range for data collection (°)	to 3.127 to 15.005	3.181 to 20.238	3.683 to 20.152	3.749 to 15.185
Completeness to $d = 0.8$ Å, %	68.5	52.5	66.2	65.1
Index ranges	$-5 < h < 5$	$-7 < h < 6$	$-6 < h < 7$	$-4 < h < 5$
	$-4 < k < 4$	$-4 < k < 3$	$-7 < k < 7$	$-5 < k < 5$
	$-6 < l < 7$	$-10 < l < 10$	$-4 < l < 4$	$-4 < l < 5$
No. of measured, independent, and observed [ $I > 2\sigma(I)$ ] reflections	265/110/99	349/138/130	310/137/126	208/93/90

$R_{\text{int}}$	0.0274	0.0437	0.0352	0.0464
No. of parameters/restraints	14/0	15/0	13/0	14/0
Goodness of fit on $F^2$	1.119	1.162	1.205	1.144
Final $R$ indices [ $I > 2\sigma(I)$ ] $R_1 / wR_2$	0.0828/0.1936	0.0735/0.1912	0.0618/0.1705	0.071/0.1792
$R$ indices (all data) $R_1 / wR_2$	0.0882/0.1981	0.0746/0.1923	0.0661/0.1748	0.0726/0.1821
Largest diff. peak /hole ( $e / \text{\AA}^3$ )	1.274/-0.857	1.480/-1.265	0.923/-1.510	1.043/-0.994

**Table S 5.3.2-3 Compressibility of bridgmanites with different compositions.**

Composition	Bulk		A-bicapped prism		B-octahedra		Reference
	K <sub>300</sub> , GPa	V <sub>0</sub> , Å <sup>3</sup> /unit cell	K <sub>300</sub> , GPa	V <sub>0</sub> , Å <sup>3</sup>	K <sub>300</sub> , GPa	V <sub>0</sub> , Å <sup>3</sup>	
(Fe <sup>2+</sup> <sub>0.64(2)</sub> Fe <sup>3+</sup> <sub>0.24(2)</sub> )SiO <sub>3</sub>	190(4)	178.98(6)	178(5)	19.25(5)	230(9)	8.51(5)	This work
(Mg <sub>0.86</sub> Fe <sub>0.14</sub> )(Si <sub>0.96</sub> Al <sub>0.04</sub> )O <sub>3</sub>	250(4)	164.49(5)	219(6)	17.92(9)	335(8)	7.69(2)	This work
(Mg <sub>0.60</sub> Fe <sub>0.40</sub> )(Si <sub>0.63</sub> Al <sub>0.37</sub> )O <sub>3</sub>	233	169.9	217(5)	18.13(5)	285(12)	8.23(4)	(Dubrovinsky et al. 2010; Glazyrin et al. 2014)
MgSiO <sub>3</sub>	251	162.36	262(5)	17.57(11)	327(5)	7.67(3)	(Sugahara et al. 2006; Ballaran et al. 2012)
(Mg <sub>0.96</sub> ,Fe <sub>0.04</sub> )SiO <sub>3</sub>	253	163.09					(Ballaran et al. 2012)
(Mg <sub>0.85</sub> ,Fe <sub>0.15</sub> )SiO <sub>3</sub>	258	163.3					(Dorfman et al. 2012)
(Mg <sub>0.91</sub> ,Fe <sub>0.09</sub> )SiO <sub>3</sub>	251	163.0					(Dorfman et al. 2013)
(Mg <sub>0.62</sub> ,Fe <sub>0.38</sub> )SiO <sub>3</sub>	264	164.7					(Dorfman et al. 2013)

$(\text{Mg}_{0.26}\text{Fe}_{0.74})\text{SiO}_3$	271	166.7					(Dorfman et al. 2013)
$(\text{Mg}_{0.95}\text{Fe}_{0.07})(\text{Si}_{0.93}\text{Al}_{0.05})\text{O}_{2.97}$	247	163.68					(Saikia et al. 2009)
$(\text{Mg}_{0.87}\text{Fe}_{0.13})(\text{Si}_{0.89}\text{Al}_{0.11})\text{O}_3$	249	164.55					(Saikia et al. 2009)
$(\text{Mg}_{0.77}\text{Fe}_{0.24})(\text{Si}_{0.82}\text{Al}_{0.17})\text{O}_3$	240	168.84					(Saikia et al. 2009)
$(\text{Mg}_{0.75}\text{Al}_{0.25})(\text{Si}_{0.75}\text{Al}_{0.25})\text{O}_3$	253	164.85					(Dorfman et al. 2012)
$(\text{Mg}_{0.345}\text{Fe}_{0.405}\text{Al}_{0.25})(\text{Si}_{0.75}\text{Al}_{0.25})\text{O}_3$	261	165.6					(Dorfman et al. 2012)
$(\text{Fe}_{0.75}\text{Al}_{0.25})(\text{Si}_{0.75}\text{Al}_{0.25})\text{O}_3$	252	170.5					(Dorfman et al. 2012)

\* Data fitted with Birch-Murnaghan equation of state with fixed  $K'=4$ .

**Table S 5.3.2-4 Crystallographic data of Fe<sub>4</sub>O<sub>5</sub>**

Empirical formula	Fe <sub>4</sub> O <sub>5</sub>
P, T conditions of XRD experiment	39 GPa 2250(100) K
Crystal system	orthorhombic
Space group	<i>Cmcm</i>
<i>a</i> (Å)	2.7379(6)
<i>b</i> (Å)	9.4010(19)
<i>c</i> (Å)	11.846(4)
<i>V</i> (Å <sup>3</sup> )	304.90(13)
<i>Z</i>	4
Fractional atomic coordinates ( <i>x y z</i> ):	
Fe1	1 0.5 0.5
Fe2	0 0.0080(3) 0.75
Fe3	0.5 0.2649(3) 0.6172(2)
O4	0.5 0.1610(19) 0.75
O5	0.5 0.3594(11) 0.4535(12)
O6	1 0.4147(12) 0.6468(11)
<i>F</i> (000)	576
Theta range for data collection (°)	4.528 to 20.916
Completeness to <i>d</i> = 0.8 Å, %	47.1
Index ranges:	-3 < <i>h</i> < 3,

	$-14 < k < 10,$
	$-13 < l < 17$
No. of measured, independent, and observed [ $I > 2\sigma(I)$ ] reflections	425/231/173
No. of parameters/restraints	32/0
$R_{\text{int}}$	0.0578
Goodness of fit on $F^2$	1.126
Final $R$ indices [ $I > 2\sigma(I)$ ] $R_1 / wR_2$	0.0874/0.2430
$R$ indices (all data) $R_1 / wR_2$	0.1007/0.2571

## 5.4 Synthesis of pure iron silicate post-perovskite

Leyla Ismailova<sup>1,2</sup>, Maxim Bykov<sup>1</sup>, Elena Bykova<sup>1</sup>, Natalia Dubrovinskaia<sup>2</sup>, Michael Hanfland<sup>3</sup>, Leonid Dubrovinsky<sup>1</sup>

<sup>1</sup>Bayerisches Geoinstitut, University of Bayreuth, D-95440 Bayreuth, Germany.

<sup>2</sup>Laboratory of Crystallography, University of Bayreuth, D-95440 Bayreuth, Germany.

<sup>3</sup>European Synchrotron Radiation Facility, BP 220, Grenoble F-38043, France.

*To be submitted to American Mineralogist*

### Abstract

At pressures of 127(1) GPa and 146(1) GPa pure iron post-perovskite was synthesized using laser-heated diamond anvil cell. Synchrotron X-ray diffraction revealed that the incorporation of iron leads to increase of the unit-cell volume relative to magnesium post-perovskite. The change in unit cell parameter  $b$  in the post-perovskite structure is the most significant contribution to volume expansion; it increases in length by 2.39% and increases total volume by 3.5% in comparison to Fe-free post-perovskite. Density of studied post-perovskite (6.670 g/cm<sup>3</sup>) is lower by 3% than the value estimated at the same conditions for pure FeSiO<sub>3</sub> ( $\rho$  6.928 g/cm<sup>3</sup>). Our results suggest that Fe post-perovskite may contribute to ultra-low velocity zones at the base of the lower mantle.

### 5.4.1 Introduction

Since the discovery of the post-perovskite phase (ppv) in MgSiO<sub>3</sub> (Murakami et al. 2004) it received much interest for its potential to explain seismic observations near the base of the lower mantle. Iron free MgSiO<sub>3</sub> has been observed to transform to the post-perovskite phase structure at 107 -126 GPa (Murakami et al. 2004; Hirose et al. 2006). The pressure range at which the post-perovskite transition occurs has been found to be raised, lowered, and/or broadened by changes in composition, depending on Fe and Al content and Fe oxidation state (Shim et al. 2008).

(Mao et al. 2004) demonstrated that iron can stabilize the post-perovskite phase at appreciably lower pressures than that required for the pure  $\text{MgSiO}_3$  end-member.

In compositions up to 75%  $\text{FeSiO}_3$  between 89 and 99 GPa (Dorfman et al. 2013) observed coexisting two phase of perovskite and post-perovskite, supporting the idea of broadening the phase transition. Theoretical studies also support the idea of decreasing the transition pressure with Fe content (Caracas and Cohen, 2013).

Sinmyo et al. (2006) have proposed that the amount of  $\text{Fe}^{3+}$  in ppv is similar to that in perovskite (pv) from electron energy-loss near-edge structure spectroscopy of the sample recovered from the stable pressure-temperature conditions of ppv. Catali et al. (2010) suggest based on powder X-ray diffraction data that the incorporation of  $\text{Fe}^{3+}$  in Mg-silicate ppv has no effect on the volume of ppv, in contrast to  $\text{Fe}^{2+}$ , which increases the volume.

The observation of the large low shear velocity provinces, which extended in the ppv stability region, appeared to be dependent on the composition of D'' layer (Ni et al. 2002). Then, it's important to understand the effect of the composition on the properties of ppv.

So far pure iron post-perovskite hasn't been synthesized, therefore, it's an open question whether it's exists and how incorporation of iron affects physical properties.

Here we report the first synthesis of pure iron post perovskite within its stability field using laser heated diamond anvil cell.

#### 5.4.2 Experimental methods

As a starting material we used skiaigite-majorite garnets with the composition  $\text{Ski}_{77}\text{Maj}_{23}\text{Fe}^{2+}_3(\text{Fe}^{2+}_{0.234(2)}\text{Fe}^{3+}_{1.532(1)}\text{Si}^{4+}_{0.234(2)})(\text{SiO}_4)_3$ . More details about this sample can be found in (Ismailova et al. 2015)

Crystals were loaded in diamonds anvil cells (DACs) in holes drilled to through Re gaskets indented to 20-35  $\mu\text{m}$  thicknesses. We used beveled diamonds with 120  $\mu\text{m}$  culets size. All DACs were loaded with Ne at  $\sim 1.4$  kbar. Neon serves as quasi-hydrostatic pressure transmitting media and a pressure standard

(<http://kantor.50webs.com>). X-ray diffraction measurements were performed at beamline ID09a at ESRF, Grenoble, France. The wavelength was  $\lambda = 0.4151 \text{ \AA}$ , the beam was focused to  $10 \times 10 \text{ \mu m}^2$ , and data collected using a Mar555 flat panel detector. Samples were heated *in situ* using double-side laser set up system designed in BGI (Kupenko et al. 2012). Data were collected by continuous rotation of the cell around the omega axis from  $-20$  to  $+20^\circ$  by  $40^\circ$  step with a 2s time exposure per frame. The 2D diffraction images were first analysed using Dioptas software (Prescher and Prakapenka 2015). Full-profile structure refinement of powder patterns was conducted using GSAS software with a graphical interface EXPFGUI (Brian H. Toby 2001).

### 5.4.3 Results

Upon laser heating of skiaigite-majorite garnet at 125(1) GPa and 2500(100) K for 30 min we observed formation of post-perovskite silicate phase coexisting with pv (Figure 5.4.3-1) (more details about synthesis, structure and the equation of state of pure iron bridgmanite can be found in Ismailova et al., 2016, submitted). In the second run already synthesized at 107.0(5) GPa and 2300(100) K single phase of iron perovskite was compressed to 146(1) GPa and laser-heated at 2500(100) K. At this conditions it transformed to a single post-perovskite phase. All the diffraction peaks were indexed as ppv, neon and rhenium (Figure 5.4.3-2). Calculated and observed ppv diffraction peaks for representative diffraction pattern are given in Table 5.4.3-1. Experimental conditions and unit-cell parameters are listed in Table 5.4.3-2

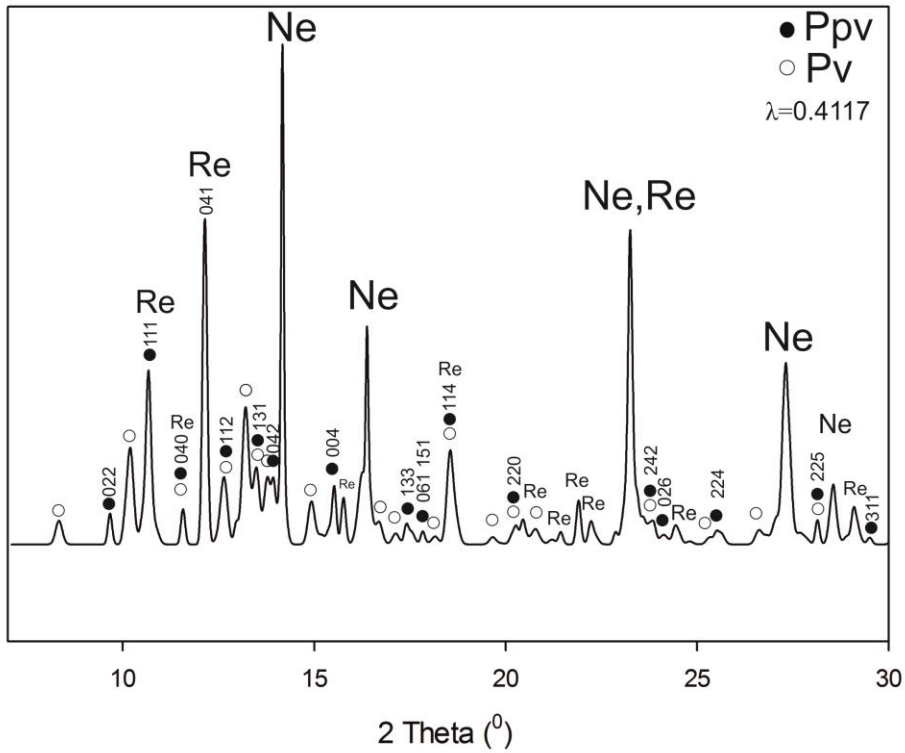


**Figure 5.4.3-1 X-ray diffraction pattern for skiagite-majorite postperovskite at 125(1) GPa. Filled circles – post perovskite, empty circles – iron perovskite (Ismailova et al.,2016), Re- renium gasket, Ne- pressure medium**

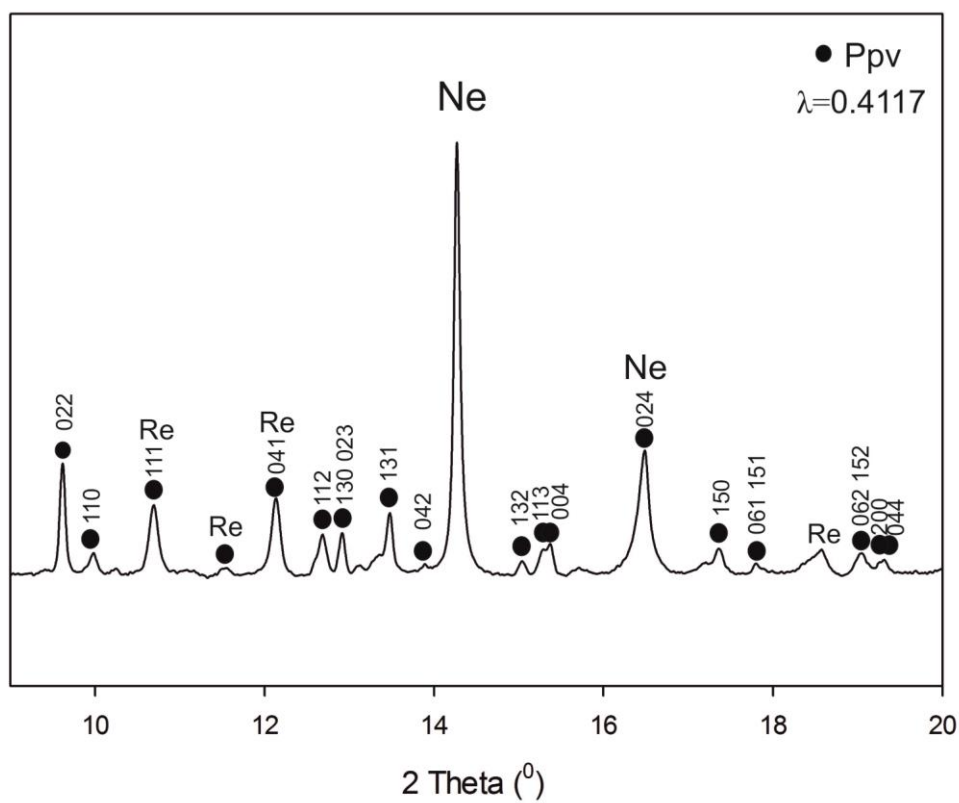


**Figure 5.4.3-2 X-ray diffraction pattern for skiagite-majorite postperovskite at 146(1) GPa. Filled circles – post perovskite, Re- rhenium gasket, Ne- pressure medium.**

**Table 5.4.3-1 Calculated and observed 2theta of post-perovskite synthesized at 146(1) GPa and 2500(100) K.**

<b>HKL</b>	<b>Calculated</b>	<b>Observed</b>
022	9.6195	9.6896
110	9.9996	9.9747
111	10.7171	10.7075
041	12.1694	12.2112
112	12.6298	12.6566
130	12.9160	12.9107
023	12.9204	13.0294
131	13.4810	13.4868
042	13.8863	13.9546
132	15.0515	15.0860
113	15.3025	15.3728
004	15.4256	15.5780
024	16.4794	16.6279
150	17.3543	17.3713
061	17.7767	17.8312
151	17.7816	17.8066
062	19.0034	19.0779
152	19.0080	19.0548
200	19.2149	19.1576
044	19.3077	19.4493

**Table 5.4.3-2 Pressure, temperature conditions of the synthesis and unit-cell parameters of post-perovskite in this study.**

<b>Pressure Temperature of synthesis</b>	<b>a(Å)</b>	<b>b(Å)</b>	<b>c(Å)</b>	<b>V (Å<sup>3</sup>)</b>
125(1) GPa and 2500(100)K	2.474(1)	8.215(1)	6.117(2)	124.35(8)
146(1) GPa and 2500(100) K	2.4667(8)	8.189(2)	6.135(2)	123.92(5)

Crystal structure of post-perovskite consists of SiO<sub>6</sub> tetrahedra sharing the edges and FeO<sub>8</sub> tetrahedra filling the interstition. The a- and c-axis in ppv correspond to the directions of edge sharing and corner-sharing respectively of octahedral within the octahedral sheets (Figure 5.4.3-3). The b-axis is along the direction in which octahedral SiO<sub>6</sub> sheets are stacked with interlayer Fe<sup>2+</sup> ions. The substitution of Fe for Mg in ppv results in the increase of the unit-cell volume. The b-axis expands the most among all three axes, in agreement with the theoretical calculations (Caracas and Cohen, 2008). The b axis increases by 2.39% from Fe-free ppv to pure iron ppv at ~127 GPa, contributing the most to the volume expansion which is 3.5 %.

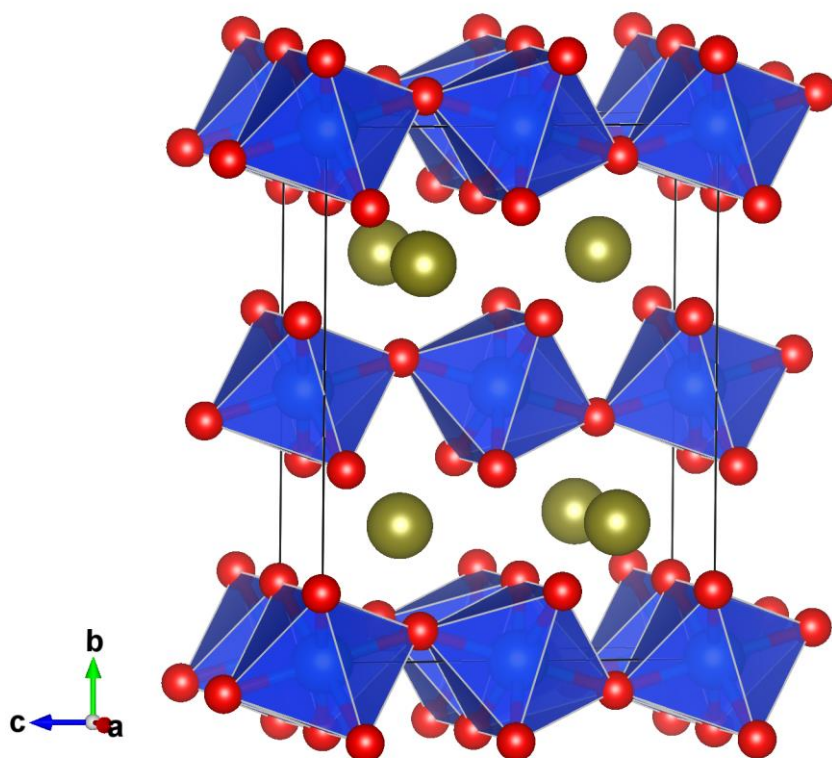


**Figure 5.4.3-3 Crystal structure of pure iron post-perovskite. The post-perovskite crystallizes in Cmc<sub>m</sub> space group, Z=4. It has a structure that consists of SiO<sub>6</sub> octahedra, they share edges along the *a* axis and corners along the *c* axis, FeO<sub>8</sub> bicapped prisms fill the interstition.**

We compare our data with previous data reported on post-perovskites volumes with variable Fe content at ~125 GPa and 300 K (Table 5.4.3-3). At 125 GPa, the volume increases by 3.5 % from pure iron post-perovskite to Fe-free MgSiO<sub>3</sub> by (Guignot et al. 2007). However, the volume reported by Ono et al(2006) is larger than that reported by (Guignot et al. 2007), but lower than the value of pure iron post-perovskite in this study. The observed variation in volume in (Mg,Fe)SiO<sub>3</sub> system with Fe content proposes an increase of the unit-cell volume and data on pure iron post-perovskite supports well this trend.

**Table 5.4.3-3 Volume of post-perovskites with variety of iron content at ~125 GPa and 300 K**

Reference	V (Å <sup>3</sup> )	X Fe
Gignot et al.,2007	120.4(4)	0
Ono et al. 2006	121.5	0
Shim et al 2008	121.3(1)	9
Zhang et al., 2012	121.63(4)	20
Zhang et al., 2012	122.57(13)	40
Dorfman et al.	123	75
this study	124.35(8)	100

Recent studies on the synthesis of Fe-rich post-perovskite report that incorporation of Fe<sup>3+</sup> has no effect on the volume of the post-perovskite (Catalli et al. 2010) while 9% of Fe<sup>2+</sup> expands the volume by 0.7 % relative to pure MgSiO<sub>3</sub> (Shim et al. 2008). Therefore, incorporation of Fe<sup>3+</sup> should increase the density of ppv much more effectively than Fe<sup>2+</sup>.

#### 5.4.4 Implications

At the 125 GPa (2700 km depth) (Dorfman and Duffy 2014) observed that density increases linearly with Fe-content in post-perovskites. The reference pressure, 125 GPa, chosen because it corresponds to 2700km depth, near the D'' discontinuity, and close to the value of the pressure of transition in to post-perovskite phase for MgSiO<sub>3</sub> (Murakami et al, 2004)

If we follow the equation given by Dorfman and Duffy, 2004.

$$\rho_{125,PPV} \text{ (g/cm}^3\text{)} = 5.548(1) + 1.38(4)X_{Fe}$$

density( $\rho_{125}$ ) of pure iron ppv (FeSiO<sub>3</sub>) should be 6.928 g/cm<sup>3</sup>.

If our synthesized post-perovskite retains the same chemical compositions as an initial skiagite-majorite garnet, calculated density ( $\rho_{127}$ ) will be 6.736 g/cm<sup>3</sup>. This is lower by 3% than the value for pure Fe ppv mentioned above. This difference in densities may be attributed to the presence of ferric iron in initial skiagite, while in work by Dorfman and Duffy, 2014 post-perovskite only with ferrous iron was used. In contrast, theoretical calculations predicted no significant difference between densities of Fe<sup>2+</sup> and Fe<sup>3+</sup> bearing post-perovskite (Yu et al. 2012).

The incorporation of iron in silicate post-perovskite increases the density and, consequently, may result in a decrease of bulk sound velocity. Thus affinity of Fe to ppv as demonstrated by synthesis of pure Fe-ppv support the idea that Fe-ppv is responsible (or at least contribute) in to formation of ultra-low velocity of the base of the mantle. Results on study of ppv will have implication for the detection of Fe-rich chemical heterogeneities in the lower mantle. However, more experimental work are required (equation of state of pure iron ppv) are needed in order to constrain the effect of iron on properties of D'' layer.

## 6 REFERENCES

Akaogi, M., and Akimoto, S. (1977) Pyroxene-garnet solid-solution equilibria in the systems  $\text{Mg}_4\text{Si}_4\text{O}_{12}$ - $\text{Mg}_3\text{Al}_2\text{Si}_3\text{O}_{12}$  and  $\text{Fe}_4\text{Si}_4\text{O}_{12}$ - $\text{Fe}_3\text{Al}_2\text{Si}_3\text{O}_{12}$ . *Physics of the Earth and Planetary Interiors*, 15, 90–106.

Amthauer, G., Annersten, H., and Hafner, S.S. (1976) The Mössbauer spectrum of  $^{57}\text{Fe}$  in silicate garnets. *Zeitschrift für Kristallographie*, 143, 14–55.

Andrault, D. (2001) Evaluation of (Mg,Fe) partitioning between silicate perovskite and magnesiowüstite up to 120 GPa and 2300 K. *Journal of Geophysical Research*, 106, 2079–2087.

Andrault, D., and Fiquet, G. (2001) Synchrotron radiation and laser-heating in a diamond anvil cell. *Review of Scientific Instruments*, 72, 1283–1288.

Angel, R.J., Finger, L.W., Hazen, R.M., Kanzaki, M., Weidner, D.J., Liebermann, R.C., and Veblen, D.R. (1989) Structure and twinning of single-crystal  $\text{MgSiO}_3$  garnet synthesized at 17 GPa and 1800°C. *American Mineralogist*, 74, 509–512.

Angel, R.J., Jackson, J.M., Reichmann, H.J., and Speziale, S. (2009) Elasticity measurements on minerals: a review. *European Journal of Mineralogy*, 21, 525–550.

- Angel, R.J., Gonzalez-Platas, J., and Alvaro, M. (2014) EosFit7c and a Fortran module (library) for equation of state calculations. *Zeitschrift fur Kristallographie*, 229, 405–419.
- Badro, J., Fiquet, G., Struzhkin, V. V., Somayazulu, M., Mao, H., Shen, G., and Le Bihan, T. (2002) Nature of the high-pressure transition in Fe<sub>2</sub>O<sub>3</sub> hematite. *Physical review letters*, 89, 205504.
- Ballaran, T.B., Kurnosov, A., Glazyrin, K., Frost, D.J., Merlini, M., Hanfland, M., and Caracas, R. (2012) Effect of chemistry on the compressibility of silicate perovskite in the lower mantle. *Earth and Planetary Science Letters*, 333-334, 181–190.
- Barbour, L.J. (2001) X-Seed — A Software Tool for Supramolecular Crystallography. *Journal of Supramolecular Chemistry*, 1, 189–191.
- Bengtson, A., Li, J., and Morgan, D. (2009) Mossbauer modeling to interpret the spin state of iron in (Mg,Fe)SiO<sub>3</sub> perovskite. *Geophysical Research Letters*, 36, L15301/1–L15301/5.
- Birch, F. (1947) Finite elastic strain of cubic crystals. *Physical Review*, 71, 809–824.
- Bobrov, A. V., Kojitani, H., Akaogi, M., and Litvin, Y.A. (2008) Phase relations on the diopside–jadeite–hedenbergite join up to 24GPa and stability of Na-bearing majoritic garnet. *Geochimica et Cosmochimica Acta*, 72, 2392–2408.
- Brian H. Toby (2001) EXPGUI, a graphical user interface for GSAS. *J. Appl. Cryst.*, 34, 210–213.
- Brodholt, J.P. (2000) Pressure-induced changes in the compression mechanism of aluminous perovskite in the Earth's mantle, 407, 620–622.
- Bykova, E., Bykov, M., Prakapenka, V., Konôpková, Z., Liermann, H.-P., Dubrovinskaia, N., and Dubrovinsky, L.S. (2013) Novel high pressure monoclinic Fe<sub>2</sub>O<sub>3</sub> polymorph revealed by single-crystal synchrotron X-ray diffraction studies. *High Pressure Research*, 33, 534–545.

- Bykova, E., Dubrovinsky, L., Dubrovinskaia, N., Bykov, M., McCammon, C., Ovsyannikov, S.V., Liermann, H.-P., Kuppenko, I., Chumakov, A.I., Rüffer, R., and others (2016) Structural complexity of simple Fe<sub>2</sub>O<sub>3</sub> oxide at high pressures and temperatures. *Nature Communications*.
- Bykova, E. a., Bobrov, A. V., Sirotkina, E. a., Bindi, L., Ovsyannikov, S. V., Dubrovinsky, L.S., and Litvin, Y. a. (2013) X-ray single-crystal and Raman study of knorringite, Mg<sub>3</sub>(Cr<sub>1.58</sub>Mg<sub>0.21</sub>Si<sub>0.21</sub>)Si<sub>3</sub>O<sub>12</sub>, synthesized at 16 GPa and 1,600 °C. *Physics and Chemistry of Minerals*, 41, 267–272.
- Canil, D., and O'Neill, H.S.C. (1996) Distribution of Ferric Iron in some Upper-Mantle Assemblages. *Journal of Petrology*, 37, 609–635.
- Caracas, R., and Cohen, R.E. (2008) Effect of Chemistry on the Physical Properties of Perovskite and Post-Perovskite. *Post-Perovskite: The Last Mantle Phase Transition*, 115–128.
- Catalli, K., Shim, S.-H., Prakapenka, V.B., Zhao, J., and Sturhahn, W. (2010) X-ray diffraction and Mossbauer spectroscopy of Fe<sup>3+</sup>-bearing Mg-silicate post-perovskite at 128-138 GPa. *American Mineralogist*, 95, 418–421.
- Cerantola, V., McCammon, C., Kuppenko, I., Kantor, I., Marini, C., Wilke, M., Ismailova, L., Solopova, N., Chumakov, A., Pascarelli, S., and others (2015) High-pressure spectroscopic study of siderite (FeCO<sub>3</sub>) with a focus on spin crossover. *American Mineralogist*, 100, 2670–2681.
- Chen, B., Jackson, J.M., Sturhahn, W., Zhang, D., Zhao, J., Wicks, J.K., and Murphy, C.A. (2012) Spin crossover equation of state and sound velocities of (Mg<sub>0.65</sub>Fe<sub>0.35</sub>)O ferropericlase to 140 GPa. *Journal of Geophysical Research: Solid Earth*, 117, 1–9.
- Collerson, K.D., Williams, Q., Kamber, B.S., Omori, S., Arai, H., and Ohtani, E. (2010) Majoritic garnet: A new approach to pressure estimation of shock events in meteorites and the encapsulation of sub-lithospheric inclusions in diamond. *Geochimica et Cosmochimica Acta*, 74, 5939–5957.

- Dobson, D.P., and Brodholt, J.P. (2005) Subducted banded iron formations as a source of ultra-low velocity zones at the core-mantle boundary. *Nature*, 434, 371–374.
- Dorfman, S.M., and Duffy, T.S. (2014) Effect of Fe-enrichment on seismic properties of perovskite and post-perovskite in the deep lower mantle. *Geophysical Journal International*, 197, 910–919.
- Dorfman, S.M., Shieh, S.R., Meng, Y., Prakapenka, V.B., and Duffy, T.S. (2012) Synthesis and equation of state of perovskites in the  $(\text{Mg,Fe})_3\text{Al}_2\text{Si}_3\text{O}_{12}$  system to 177GPa. *Earth and Planetary Science Letters*, 357-358, 194–202.
- Dorfman, S.M., Meng, Y., Prakapenka, V.B., and Duffy, T.S. (2013) Effects of Fe-enrichment on the equation of state and stability of  $(\text{Mg,Fe})\text{SiO}_3$  perovskite. *Earth and Planetary Science Letters*, 361, 249–257.
- Dubrovinsky, L., Dubrovinskaia, N., Kantor, I., Nestola, F., and Gatta, D. (2006) High-brilliance X-ray system for high-pressure in-house research: applications for studies of superhard materials. *High Pressure Research*, 26, 137–143.
- Dubrovinsky, L., Glazyrin, K., Kurnosov, A., Frost, D., Hanfland, M., Prakapenka, V.B., Schouwink, P., and Pippinger, T. (2010) Single-crystal X-ray diffraction at megabar pressures and temperatures of thousands of degrees, 7959.
- Dubrovinsky, L.S., N. Dubrovinskaia, Langenhorst, F., Dobson, D.P., Rubie, D.C., Gessmann, C., Abrikosov, I.A., Johansson, B., Baykov, V.I., Vitos, L., and others (2003) Iron – silica interaction at extreme conditions and the electrically conducting layer at the base of Earth’s mantle. *Nature*, 422, 58–61.
- Dubrovinsky, L.S., Dubrovinskaia, N.A., McCammon, C., Rozenberg, G.K., Ahuja, R., Osorio-Guillen, J.M.M., Dmitriev, V., Weber, H.-P.H.-P., Bihan, T.L. Le, and Johansson, B. (2003) The structure of the metallic high-pressure  $\text{Fe}_3\text{O}_4$  polymorph: experimental and theoretical study. *Journal of Physics: Condensed Matter*, 15, 7697.
- Duffy, T.S., and Anderson, D.L. (1989) Seismic velocities in mantle minerals and the mineralogy of the upper mantle. *Journal of Geophysical Research*, 94, 1895.

Dymshits, A.M., Bobrov, A. V., Bindi, L., Litvin, Y.A., Litasov, K.D., Shatskiy, A.F., and Ohtani, E. (2013) Na-bearing majoritic garnet in the  $\text{Na}_2\text{MgSi}_5\text{O}_{12}$ - $\text{Mg}_3\text{Al}_2\text{Si}_3\text{O}_{12}$  join at 11-20GPa: Phase relations, structural peculiarities and solid solutions. *Geochimica et Cosmochimica Acta*, 105, 1–13.

Dymshits, A.M., Litasov, K.D., Shatskiy, A., Sharygin, I.S., Ohtani, E., Suzuki, A., Pokhilenko, N.P., and Funakoshi, K. (2014) P – V – T equation of state of Na-majorite to 21 GPa and 1673 K. *Physics of the Earth and Planetary Interiors*, 227, 68–75.

Dymshits, A.M., Litasov, K.D., Sharygin, I.S., Shatskiy, A., Ohtani, E., Suzuki, A., and Funakoshi, K. (2014) Thermal equation of state of majoritic knorringite and its significance for continental upper mantle. *Journal of Geophysical Research B: Solid Earth*, 1–13.

E.Bykova (2015) Single-crystal X-ray diffraction at extreme conditions in mineral physics and material sciences. University of Bayreuth.

Fei, Y., Wang, Y., and Finger, L.W. (1996) Maximum solubility of FeO in  $(\text{Mg,Fe})\text{SiO}_3$ -perovskite as a function of temperature at 26 GPa: Implication for FeO content in the lower mantle. *Journal of Geophysical Research*, 101, 11525.

Fei, Y., Ricolleau, A., Frank, M., Mibe, K., Shen, G., and Prakapenka, V. (2007) Toward an internally consistent pressure scale. *Proceedings of the National Academy of Sciences of the United States of America*, 104, 9182–9186.

Friedrich, A., Winkler, B., Morgenroth, W., Ruiz-Fuertes, J., Koch-Müller, M., Rhede, D., and Milman, V. (2014) Pressure-induced spin collapse of octahedrally coordinated  $\text{Fe}^{3+}$  in  $\text{Ca}_3\text{Fe}_2[\text{SiO}_4]_3$ . *Physical Review B*, 90, 094105.

Friedrich, A., Winkler, B., Morgenroth, W., Perlov, A., and Milman, V. (2015) Pressure-induced spin collapse of octahedrally coordinated  $\text{Mn}^{3+}$  in the tetragonal hydrogarnet henritermierite  $\text{Ca}_3\text{Mn}_2[\text{SiO}_4]_2[\text{O}_4\text{H}_4]$ . *Physical Review B - Condensed Matter and Materials Physics*, 92.

- Frost, D., Liebske, C., Langenhorst, F., McCammon, C. a, Trønnes, R.G., and Rubie, D.C. (2004) Experimental evidence for the existence of iron-rich metal in the Earth's lower mantle. *Nature*, 428, 409–412.
- Frost, D.J. (2008) and Transition Zone. *Elements*, 171–176.
- Frost, D.J., Poe, B., Trønnes, R., Liebske, C., Duba, A., and Rubie, D.. (2004) A new large-volume multianvil system. *Physics of the Earth and Planetary Interiors*, 143-144, 507–514.
- Fujino, K., Nishio-Hamane, D., Suzuki, K., Izumi, H., Seto, Y., and Nagai, T. (2009) Stability of the perovskite structure and possibility of the transition to the post-perovskite structure in  $\text{CaSiO}_3$ ,  $\text{FeSiO}_3$ ,  $\text{MnSiO}_3$ ,  $\text{CoSiO}_3$ . *Physics of the Earth and Planetary Interiors*, 177, 147–151.
- Fursenko, B.A. (1981) Synthesis of new high-pressure garnets:  $\text{Mn}_3\text{Cr}_2\text{Si}_3\text{O}_{12}$  and  $\text{Fe}_3\text{Cr}_2\text{Si}_3\text{O}_{12}$ . *Bulletin de Mineralogie*, 104, 418–422.
- Gavriliuk, A.G., Struzhkin, V. V, Lyubutin, I.S., Eremets, M.I., Trojan, I.A., and Artemov, V. V (2006) Equation of State and High-Pressure Irreversible Amorphization in  $\text{Y}_3\text{Fe}_5\text{O}_{12}$ , 83, 37–41.
- Glazyrin, K., Boffa Ballaran, T., Frost, D.J., McCammon, C., Kantor, I., Merlini, M., Hanfland, M., and Dubrovinsky, L. (2014) Magnesium silicate perovskite and effect of iron oxidation state on its bulk sound velocity at the conditions of the lower mantle. *Earth and Planetary Science Letters*, 393, 182–186.
- Gudmundsson, G., and Wood, B.J. (1995) Experimental tests of garnet peridotite oxygen barometry. *Contributions to Mineralogy and Petrology*, 56–67.
- Guignot, N., Andrault, D., Morard, G., Bolfan-Casanova, N., and Mezouar, M. (2007) Thermoelastic properties of post-perovskite phase  $\text{MgSiO}_3$  determined experimentally at core-mantle boundary P-T conditions. *Earth and Planetary Science Letters*, 256, 162–168.
- Gwanmesia, G.D., Wang, L., Triplett, R., and Liebermann, R.C. (2009) Pressure and temperature dependence of the elasticity of pyrope–majorite [ $\text{Py}_{60}\text{Mj}_{40}$  and  $\text{Py}_{50}\text{Mj}_{50}$ ]

garnets solid solution measured by ultrasonic interferometry technique. *Physics of the Earth and Planetary Interiors*, 174, 105–112.

Hammond, C. (2009) *The Basics of Crystallography and Diffraction*, 432 p. Oxford University Press, USA.

Hatch, D., and Ghose, S. (1989) Symmetry analysis of the phase transition and twinning in MgSiO<sub>3</sub> garnet: Implications to mantle mineralogy. *Contributions to Mineralogy and Petrology*, 101, 1221–1224.

Hazen, R.M., Downs, R.T., Conrad, P.G., Finger, L.W., and Gasparik, T. (1994) Comparative compressibilities of majorite-type garnets. *Physics and Chemistry of Minerals*, 21, 1994.

Heinemann, S., Sharp, T.G., and Seifert, F. (1997) The cubic-tetragonal phase transition in the system majorite and garnet symmetry in the Earth's transition zone. *Physics and Chemistry of Minerals*, 24, 206–221.

Hirose, K., Sinmyo, R., Sata, N., and Ohishi, Y. (2006) Determination of post-perovskite phase transition boundary in MgSiO<sub>3</sub> using Au and MgO pressure standards. *Geophysical Research Letters*, 33, 1–5.

Hsu, H., Blaha, P., Cococcioni, M., and Wentzcovitch, R.M. (2011) Spin-State Crossover and Hyperfine Interactions of Ferric Iron in MgSiO<sub>3</sub> Perovskite. *Physical Review Letters*, 106, 118501.

Irifune, T. (1987) An experimental investigation of the pyroxene-garnet transformation in a pyrolite composition and its bearing on the constitution of the mantle. *Physics of the Earth and Planetary Interiors*, 45, 324–336.

Irifune, T., and Ringwood, A.E. (1993) Phase transformations in subducted oceanic crust and buoyancy relationships at depths of 600–800 km in the mantle. *Earth and Planetary Science Letters*, 117, 101–110.

Irifune, T., Sekine, T., Ringwood, A.E., and Hibberson, W.O. (1986) The eclogite-garnetite transformation at high pressure and some geophysical implications. *Earth and Planetary Science Letters*, 77, 245–256.

- Irifune, T., Higo, Y., Inoue, T., Kono, Y., Ohfuji, H., and Funakoshi, K. (2008) Sound velocities of majorite garnet and the composition of the mantle transition region. *Nature*, 451, 814–817.
- Ismailova, L., Bobrov, A., Bykov, M., Bykova, E., Cerantola, V., Kuppenko, I., McCammon, C., Dyadkin, V., Chernyshov, D., Pascarelli, S., and others (2015) High-pressure synthesis of skiagite-majorite garnet and investigation of its crystal structure. *American Mineralogist*, 100, 2650–2654.
- Ita, J., and Stixrude, L. (1992) Petrology, elasticity, and composition of the mantle transition. *Journal of Geophysical Research*, 97(B5), 6849–6866.
- Ito, E. (2007) 2 . 08 Theory and Practice – Multianvil Cells and High-Pressure Experimental Methods.
- Kantor, I., Dubrovinsky, L., and McCammon, C. (2006) Spin crossover in (Mg,Fe)O: A Mössbauer effect study with an alternative interpretation of x-ray emission spectroscopy data. *Physical Review B*, 73, 100101.
- Kantor, I., Prakapenka, V., Dera, P., Kurnosov, A., Sinogeikin, S., Dubrovinskaia, N., and Dubrovinsky, L. (2012) BX90: a new diamond anvil cell design for X-ray diffraction and optical measurements. *The Review of scientific instruments*, 83, 125102.
- Kato, T. (1986) Stability relation of (Mg,Fe)SiO<sub>3</sub> garnets, major constituents in the Earth's interior. *Earth and Planetary Science Letters*, 77, 399–408.
- Katsura, T., Yoneda, A., Yamazaki, D., Yoshino, T., and Ito, E. (2010) Adiabatic temperature profile in the mantle. *Physics of the Earth and Planetary Interiors*, 183, 212–218.
- Keppler, H., and Frost, D.. (2005) Introduction to minerals under extreme conditions. Miletich, R. Ed. *EMU Notes in Mineralogy*, 7, 1–30.
- Keppler, H., Kantor, I., and Dubrovinsky, L. (2007) Optical absorption spectra of ferropericlasite to 84 GPa. *American Mineralogist*, 92, 433–436.

- Knittle, E., Jeanloz, R., and Knittle, E. (1991) Earth's core-mantle boundary: Results of Experiments at High Pressures and Temperatures. *Science* (New York, N.Y.), 251, 1438–1442.
- Kupenko, I., Dubrovinsky, L., Dubrovinskaia, N., McCammon, C., Glazyrin, K., Bykova, E., Ballaran, T.B., Sinmyo, R., Chumakov, A.I., Potapkin, V., and others (2012) Portable double-sided laser-heating system for Mossbauer spectroscopy and X-ray diffraction experiments at synchrotron facilities with diamond anvil cells. *Review of Scientific Instruments*, 83.
- Kupenko, I., McCammon, C., Sinmyo, R., Prescher, C., Chumakov, A.I., Kantor, A., Rüffer, R., and Dubrovinsky, L. (2014) Lithos Electronic spin state of Fe, Al-containing MgSiO<sub>3</sub> perovskite at lower mantle conditions. *LITHOS*, 189, 167–172.
- Kupenko, I., McCammon, C., Sinmyo, R., Cerantola, V., Potapkin, V., Chumakov, A.I., Kantor, A., Rüffer, R., and Dubrovinsky, L. (2015) Oxidation state of the lower mantle: In situ observations of the iron electronic configuration in bridgmanite at extreme conditions. *Earth and Planetary Science Letters*, 423, 78–86.
- Kurnosov, A., Kantor, I., Boffa-Ballaran, T., Lindhardt, S., Dubrovinsky, L., Kuznetsov, A., and Zehnder, B.H. (2008) A novel gas-loading system for mechanically closing of various types of diamond anvil cells. *Review of Scientific Instruments*, 79.
- Larson, C., and Von Dreele, R.B. (2004) General Structure Analysis System (GSAS). *Structure*, 748, 86–748.
- Lavina, B., Dera, P., Downs, R.T., Prakapenka, V., Rivers, M., Sutton, S., and Nicol, M. (2009) Siderite at lower mantle conditions and the effects of the pressure-induced spin-pairing transition. *Geophysical Research Letters*, 36, 1–4.
- Lavina, B., Dera, P., Kim, E., Meng, Y., Downs, R.T., and Weck, P.F. (2011) Discovery of the recoverable high-pressure iron oxide Fe<sub>4</sub>O<sub>5</sub>. *Proceedings of the National Academy of Sciences*, 108, 17281–17285.

- Lee, C.-T. a, Luffi, P., Höink, T., Li, J., Dasgupta, R., and Hernlund, J. (2010) Upside-down differentiation and generation of a “primordial” lower mantle. *Nature*, 463, 930–933.
- Li, B., and Liebermann, R.C. (2007) Indoor seismology by probing the Earth ’ s interior by using sound velocity measurements at high pressures and temperatures *Sound Velocity Measurements at High Pressure*.
- Liermann, H.-P., Konôpková, Z., Morgenroth, W., Glazyrin, K., Bednarčík, J., McBride, E.E., Petitgirard, S., Delitz, J.T., Wendt, M., Bican, Y., and others (2015) The Extreme Conditions Beamline P02.2 and the Extreme Conditions Science Infrastructure at PETRA III. *Journal of Synchrotron Radiation*, 22, 1–17.
- Lin, J.-F., Weir, S.T., Jackson, D.D., Evans, W.J., Vohra, Y.K., Qiu, W., and Yoo, C.-S. (2007) Electrical conductivity of the lower-mantle ferropericlase across the electronic spin transition. *Geophysical Research Letters*, 34, L16305.
- Liu, J., Chen, G., Gwanmesia, G.D., and Liebermann, R.C. (2000) Elastic wave velocities of a pyrope-majorite garnets (Py<sub>62</sub>Mj<sub>38</sub> and Py<sub>50</sub>Maj<sub>50</sub> to 9 GPa. *Physics of the Earth and Planetary Interiors*, 120, 153–163.
- Liu, L.G. (1975) Post-oxide phases of olivine and pyroxene and mineralogy of the mantle. *Nature*, 258, 510–512.
- Luth, R.W., Virgo, D., Boyd, F.R., Wood, B.J., Geoinstitut, B., Bayreuth, U., Bayreuth, D., and Republic, F. (1990) Ferric iron in mantle-derived garnets. Implications for thermobarometry and for the oxidation state of the mantle, 104, 56–72.
- Lyubutin, I.S., Gavriliuk, A.G., Trojan, I.A., and Sadykov, R.A. (2005) Magnetic Collapse in Yttrium Iron Garnet Y<sub>3</sub>Fe<sub>5</sub>O<sub>12</sub> at High Pressure, 82, 797–802.
- Mao, H. -k., Shen, G., and Hemley, R.J. (1997) Multivariable dependence of Fe-Mg partitioning in the lower mantle. *Science (New York, N.Y.)*, 278, 2098–2100.
- Mao, H.K., Xu, J., and Bell, P.M. (1986) Calibration of the ruby pressure gauge to 800 kbar under quasi-hydrostatic conditions. *Journal of Geophysical Research*, 91, 4673–4676.

- Mao, W.L., Shen, G., Prakapenka, V.B., Meng, Y., Campbell, A.J., Heinz, D.L., Shu, J., Hemley, R.J., and Mao, H. (2004) Ferromagnesian postperovskite silicates in the D'' layer of the Earth, 101, 15867–15869.
- Mao, W.L., Mao, H.K., Sturhahn, W., Zhao, J., Prakapenka, V.B., Meng, Y., Shu, J., Fei, Y., and Hemley, R.J. (2006) Iron-rich Post-Perovskite and the Origin of Ultralow-Velocity Zones. *Science* (New York, N.Y.), 312, 564–565.
- Matsubara, R., Toraya, H., Tanaka, S., and Sawamoto, H. (1990) Precision lattice-parameter determination of (Mg,Fe)SiO<sub>3</sub> tetragonal garnets. *Science* (New York, N.Y.), 697–699.
- McCammon, C. a., and Ross, N.L. (2003) Crystal chemistry of ferric iron in (Mg,Fe)(Si,Al)O<sub>3</sub> majorite with implications for the transition zone. *Physics and Chemistry of Minerals*, 30, 206–216.
- Merlini, M., Hanfland, M., Gemmi, M., Huotari, S., Simonelli, L., and Strobel, P. (2010) Fe<sup>3+</sup> spin transition in CaFe<sub>2</sub>O<sub>4</sub> at high pressure. *American Mineralogist*, 95, 200–203.
- Milman, V., Akhmatkaya, E. V., Nobes, R.H., Winkler, B., Pickard, C.J., and White, J.A. (2001) Systematic ab initio study of the compressibility of silicate garnets. *Acta Crystallographica Section B: Structural Science*, 57, 163–177.
- Ming, L., Bassett, W. (1975) Decomposition of FeSiO<sub>3</sub> into FeO and SiO<sub>2</sub> under very high pressure and high temperature. *Earth and Planetary Science Letters*, 25, 68–70.
- Momma, K., and Izumi, F. (2011) VESTA 3 for three-dimensional visualization of crystal, volumetric and morphology data. *Journal of Applied Crystallography*, 44, 1272–1276.
- Murakami, M. (2004) Post-Perovskite Phase Transition in MgSiO<sub>3</sub>. *Science*, 304, 855–858.
- Murakami, M., Hirose, K., Kawamura, K., Sata, N., and Ohishi, Y. (2004) Post-Perovskite Phase Transition in MgSiO<sub>3</sub>. *Science* (New York, N.Y.), 304, 855–858.

- Murakami, M., Ohishi, Y., Hirao, N., and Hirose, K. (2012) A perovskitic lower mantle inferred from high-pressure, high-temperature sound velocity data. *Nature*, 485, 90–94.
- Ni, S., Tan, E., Gurnis, M., and Helmberger, D. (2002) Sharp Sides to the African Superplume. *Science*, 296, 1850–1852.
- Novak, G.A., and Gibbs, G.V. (1971) The crystal chemistry of the silicate garnets. *American Mineralogist*, 56, 791–825.
- O'Neill, H.S.C., McCammon, C.A., Canil, D., Rubie, D.C., Ross, C.R., and Seifert, F. (1993) Mossbauer spectroscopy of mantle transition zone phases and determination of minimum Fe<sup>3+</sup> content. *American Mineralogist*, 78, 456–460.
- Ohtani, E., Kagawa, N., and Fujino, K. (1991) Stability of majorite (Mg,Fe)SiO<sub>3</sub> at high pressures and 1800 °C. *Earth and Planetary Science Letters*, 102, 158–166.
- Oxford Diffraction (2006) CrysAlisPro. Oxford Diffraction Ltd, Abingdon, Oxfordshire, England.
- Pascarelli, S., Mathon, O., Muñoz, M., Mairs, T., and Susini, J. (2006) Energy-dispersive absorption spectroscopy for hard-X-ray micro-XAS applications. *Journal of Synchrotron Radiation*, 13, 351–358.
- Petříček, V., Dušek, M., and Palatinus, L. (2014) Crystallographic Computing System JANA2006: General features. *Zeitschrift für Kristallographie- ...*, 229, 345–352.
- Potapkin, V., Chumakov, A.I., Smirnov, G. V, Celse, J.P., Rüffer, R., McCammon, C., and Dubrovinsky, L. (2012) The <sup>57</sup>Fe Synchrotron Mössbauer Source at the ESRF. *Journal of synchrotron radiation*, 19, 559–69.
- Prakapenka, V.B., Kubo, A., Kuznetsov, A., Laskin, A., Shkurikhin, O., Dera, P., Rivers, M.L., and Sutton, S.R. (2008) Advanced flat top laser heating system for high pressure research at GSECARS: application to the melting behavior of germanium. *High Pressure Research*, 28, 225–235.

- Prescher, C., and Prakapenka, V.B. (2015) DIOPTAS : a program for reduction of two-dimensional X-ray diffraction data and data exploration. *High Pressure Research*, 35, 223–230.
- Prescher, C., McCammon, C., and Dubrovinsky, L. (2012) MossA : a program for analyzing energy-domain Mössbauer spectra from conventional and synchrotron sources. *Journal of Applied Crystallography*, 45, 329–331.
- Ringwood, A.E. (1975) Composition and petrology of the Earth's upper mantle.
- Rüffer, R., and Chumakov, A.I. (1996) Nuclear Resonance Beamline at ESRF. *Hyperfine Interactions*, 97-98, 589–604.
- Saikia, A., Ballaran, T.B., and Frost, D.J. (2009) The effect of Fe and Al substitution on the compressibility of MgSiO<sub>3</sub>-perovskite determined through single-crystal X-ray diffraction. *Physics of the Earth and Planetary Interiors*, 173, 153–161.
- Saxena, S.K., Dubrovinsky, L.S., Lazor, P., Cerenius, Y., Häggkvist, P., Hanfland, M., and J., H. (1996) Stability of perovskite (MgSiO<sub>3</sub>) in the Earth's mantle. *Science (New York, N.Y.)*, 274, 1357–1359.
- Sheldrick, G.M. (2008) A short history of SHELX. *Acta Crystallographica Section A: Foundations of Crystallography*, 64, 112–122.
- Shim, S., Duffy, T.S., and Shen, G. (2001) Stability and Structure of MgSiO<sub>3</sub> Perovskite to 2300-Kilometer Depth in Earth's Mantle. *Science (New York, N.Y.)*, 293, 2437–2440.
- Shim, S.-H., Catalli, K., Hustoft, J., Kubo, A., Prakapenka, V.B., Caldwell, W. a, and Kunz, M. (2008) Crystal structure and thermoelastic properties of (Mg<sub>0.91</sub>Fe<sub>0.09</sub>)SiO<sub>3</sub> postperovskite up to 135 GPa and 2,700 K. *Proceedings of the National Academy of Sciences of the United States of America*, 105, 7382–7386.
- Sinogeikin, S. V., and Bass, J.D. (2000) Single-crystal elasticity of pyrope and MgO to 20 GPa by Brillouin scattering in the diamond cell. *Physics of the Earth and Planetary Interiors*, 120, 43–62.

- Sinogeikin, S. V., and Bass, J.D. (2002) Elasticity of pyrope and majorite-pyrope solid solutions to high temperatures. *Earth and Planetary Science Letters*, 203, 549–555.
- Speziale, S., Lee, V.E., Clark, S.M., Lin, J.F., Pasternak, M.P., and JeanLoz, R. (2007) Effects of Fe spin transition on the elasticity of (Mg, Fe)O magnesiowustites and implications for the seismological properties of the Earth's lower mantle. *Journal of Geophysical Research: Solid Earth*, 112, 1–12.
- Stachel, T., Brey, G., and Harris, J.W. (2010) Inclusions in sublithospheric diamonds: Glimpses of deep Earth. *Elements*, 1, 73–78.
- Stan, C. V., Wang, J., Zouboulis, I.S., Prakapenka, V., and Duffy, T.S. (2015) High-pressure phase transition in  $\text{Y}_3\text{Fe}_5\text{O}_{12}$ . *Journal of Physics: Condensed Matter*, 27, 405401.
- Sturhahn, W. (2000) CONUSS and PHOENIX: Evaluation of nuclear resonant scattering data. *Hyperfine Interactions*, 125, 149–172.
- Sugahara, M., Yoshiasa, A., Komatsu, Y., Yamanaka, T., Bolfan-Casanova, N., Nakatsuka, A., Sasaki, S., and Tanaka, M. (2006) Reinvestigation of the  $\text{MgSiO}_3$  perovskite structure at high pressure. *American Mineralogist*, 91, 533–536.
- Tange, Y., Takahashi, E., Nishihara, Y., Funakoshi, K., and Sata, N. (2009) Phase relations in the system  $\text{MgO-FeO-SiO}_2$  to 50 GPa and 2000°C: An application of experimental techniques using multianvil apparatus with sintered diamond anvils. *Journal of Geophysical Research*, 114, B02214.
- Tateno, S., Hirose, K., Sata, N., and Ohishi, Y. (2005) Phase relations in  $\text{Mg}_3\text{Al}_2\text{Si}_3\text{O}_{12}$  to 180 GPa: Effect of Al on post-perovskite phase transition. *Geophysical Research Letters*, 32, 10–13.
- Tomioka, N., Fujino, K., Ito, E., Katsura, T., Sharp, T.G., and Kato, T. (2002) Microstructures and structural phase transition in (Mg,Fe) $\text{SiO}_3$  majorite. *European Journal of Mineralogy*, 14, 7–14.

- Tschauner, O., Ma, C., Beckett, J.R., Prescher, C., Prakapenka, V.B., and Rossman, G.R. (2014) Mineralogy. Discovery of bridgmanite, the most abundant mineral in Earth, in a shocked meteorite. *Science* (New York, N.Y.), 346, 1100–2.
- Wolf, A.S., Jackson, J.M., Dera, P., and Prakapenka, V.B. (2015) The thermal equation of state of (Mg,Fe)SiO<sub>3</sub> bridgmanite (perovskite) and implications for lower mantle structures. *Journal of Geophysical Research B: Solid Earth*, 120(11), 7460–7489.
- Wood, B.J., Pawley, A., and Frost, D. (1996) Water and carbon in the Earth's mantle. *Philosophical Transactions of the Royal Society of London*, 354, 1495–1511.
- Wood, B.J., Kiseeva, E.S., and Matzen, a. K. (2013) Garnet in the Earth's Mantle. *Elements*, 9, 421–426.
- Woodland, a. B., Bauer, M., Ballaran, T.B., and Hanrahan, M. (2009) Crystal chemistry of Fe<sub>3</sub><sup>2+</sup>Cr<sub>2</sub>Si<sub>3</sub>O<sub>12</sub>-Fe<sub>3</sub><sup>2+</sup>Fe<sub>2</sub><sup>3+</sup>Si<sub>3</sub>O<sub>12</sub> garnet solid solutions and related spinels. *American Mineralogist*, 94, 359–366.
- Woodland, A.B., and Koch, M. (2003) Variation in oxygen fugacity with depth in the upper mantle beneath the Kaapvaal craton, Southern Africa. *Earth and Planetary Science Letters*, 214, 295–310.
- Woodland, A.B., and O'Neill, H.S.C. (1993) Synthesis and stability of Fe<sub>3</sub>Fe<sub>2</sub>Si<sub>3</sub>O<sub>12</sub> garnet and phase relation with Fe<sub>3</sub>Al<sub>2</sub>Si<sub>3</sub>O<sub>12</sub> - Fe<sub>3</sub>Fe<sub>2</sub>Si<sub>3</sub>O<sub>12</sub> solutions. *American Mineralogist*, 78, 1000–1013.
- (1995) Phase relation between Ca<sub>3</sub>Fe<sub>2</sub>Si<sub>3</sub>O<sub>12</sub>-Fe<sub>3</sub>Fe<sub>2</sub>Si<sub>3</sub>O<sub>12</sub> garnet and CaFe<sub>2</sub>Si<sub>2</sub>O<sub>6</sub>-Fe<sub>2</sub>Si<sub>2</sub>O<sub>6</sub> solutions. *Contributions to Mineralogy and Petrology*, 121, 87–98.
- Woodland, A.B., and Ross, C.R. (1994) A crystallographic and Mössbauer spectroscopy study of Fe<sub>3</sub>Al<sub>2</sub>Si<sub>3</sub>O<sub>12</sub> - Fe<sub>3</sub><sup>2+</sup>Fe<sub>2</sub><sup>3+</sup>Si<sub>3</sub>O<sub>12</sub> and Ca<sub>3</sub>Fe<sub>2</sub><sup>3+</sup>Si<sub>3</sub>O<sub>12</sub> - Fe<sub>3</sub><sup>2+</sup>Fe<sub>2</sub><sup>3+</sup>Si<sub>3</sub>O<sub>12</sub> (andradite-skiagite) garnet solid solutions. *Physic and Chemistry of Minerals*, 117–132.
- Woodland, A.B., Angel, R.J., Koch, M., and Kunz, M. (1999) Equations of state for Fe<sub>3</sub>Fe<sub>2</sub>SiO<sub>4</sub> -- Fe<sub>3</sub>O<sub>4</sub> spinel solid solutions, 104.

Xu, S., Shim, S., and Morgan, D. (2015) Origin of Fe<sup>3+</sup> in Fe-containing, Al-free mantle silicate perovskite. *Earth and Planetary Science Letters*, 409, 319–328.

Xu, W., Greenberg, E., Rozenberg, G.K., Pasternak, M.P., Bykova, E., Boffa-Ballaran, T., Dubrovinsky, L., Prakapenka, V., Hanfland, M., Vekilova, O.Y., and others (2013) Pressure-induced hydrogen bond symmetrization in iron oxyhydroxide. *Physical Review Letters*, 111, 1–5.

Yu, Y.G., Hsu, H., Cococcioni, M., and Wentzcovitch, R.M. (2012) Spin states and hyperfine interactions of iron incorporated in MgSiO<sub>3</sub> post-perovskite. *Earth and Planetary Science Letters*, 331-332, 1–7.

Zhang, L., Meng, Y., Yang, W., Wang, L., Mao, W.L., Zeng, Q.-S., Jeong, J.S., Wagner, A.J., Mkhoyan, K.A., Liu, W., and others (2014) Disproportionation of (Mg,Fe)SiO<sub>3</sub> perovskite in Earth's deep lower mantle. *Science (New York, N.Y.)*, 344, 877–82.

(Eidesstattliche) Versicherungen und Erklärungen

(§ 8 S. 2 Nr. 6 PromO)

Hiermit erkläre ich mich damit einverstanden, dass die elektronische Fassung meiner Dissertation unter Wahrung meiner Urheberrechte und des Datenschutzes einer gesonderten Überprüfung hinsichtlich der eigenständigen Anfertigung der Dissertation unterzogen werden kann.

(§ 8 S. 2 Nr. 8 PromO)

Hiermit erkläre ich eidesstattlich, dass ich die Dissertation selbständig verfasst und keine anderen als die von mir angegebenen Quellen und Hilfsmittel benutzt habe.

(§ 8 S. 2 Nr. 9 PromO)

Ich habe die Dissertation nicht bereits zur Erlangung eines akademischen Grades anderweitig eingereicht und habe auch nicht bereits diese oder eine gleichartige Doktorprüfung endgültig nicht bestanden.

(§ 8 S. 2 Nr. 10 PromO)

Hiermit erkläre ich, dass ich keine Hilfe von gewerblichen Promotionsberatern bzw. -vermittlern in Anspruch genommen habe und auch künftig nicht nehmen werde.

.....

Ort, Datum, Unterschrift